



저작자표시-비영리-변경금지 2.0 대한민국

이용자는 아래의 조건을 따르는 경우에 한하여 자유롭게

- 이 저작물을 복제, 배포, 전송, 전시, 공연 및 방송할 수 있습니다.

다음과 같은 조건을 따라야 합니다:



저작자표시. 귀하는 원저작자를 표시하여야 합니다.



비영리. 귀하는 이 저작물을 영리 목적으로 이용할 수 없습니다.



변경금지. 귀하는 이 저작물을 개작, 변형 또는 가공할 수 없습니다.

- 귀하는, 이 저작물의 재이용이나 배포의 경우, 이 저작물에 적용된 이용허락조건을 명확하게 나타내어야 합니다.
- 저작권자로부터 별도의 허가를 받으면 이러한 조건들은 적용되지 않습니다.

저작권법에 따른 이용자의 권리는 위의 내용에 의하여 영향을 받지 않습니다.

이것은 [이용허락규약\(Legal Code\)](#)을 이해하기 쉽게 요약한 것입니다.

[Disclaimer](#)

工學博士學位論文

**High-Performance Carbon Electrode-based
Perovskite Solar Cells *via* Interface Engineering**

계면 공정을 통한 고성능의
카본 전극 기반 페로브스카이트 태양전지 제조

2020年 8月

서울대학교 大學院

化學生物工學部

金重元

High-Performance Carbon Electrode-based Perovskite
Solar Cells via Interface Engineering

계면 공정을 통한 고성능의

카본전극 기반 페로브스카이트 태양전지 제조

指導教授 張 正 植

이 論文을 工學博士 學位論文으로 提出함

2020 年 6 月

서울대학교 大學院

化學生物工學部

金 重 元

金重元の 工學博士 學位論文을 認准함

2020 年 6 月

委員長

趙 在 英



副委員長

張 正 植



委 員

林 淳 皓



委 員

李 鍾 贊



委 員

吳 俊 鶴



**High-Performance Carbon Electrode-based Perovskite
Solar Cells *via* Interface Engineering**

by

Jungwon Kim

Submitted to the Graduate School of Seoul National
University in Partial Fulfillment of the Requirements for
the Degree of Doctor of Philosophy

August, 2020

Thesis Adviser: Jyongsik Jang

Abstract

Perovskite solar cells (PSCs) based on organic-inorganic halide perovskite (ABX_3 structure) have rapidly developed as one of the most potent next-generation photovoltaic devices based on their extraordinary optical and physical properties. The photovoltaic performance of PSC, which has been swiftly improving to date, is comparable to commercial-silicon solar cells. In recent years, research trends are turning into real problems related to the actual use of PSCs in daily life, such as large-scale modularization, long-term stability, and toxicity testing for commercialization of PSCs. In particular, in terms of stability, decomposition of the perovskite by external stress factors (e.g. moisture, air, heat and etc.) and deterioration at the interface between a metal electrode and charge transport layer are important issues to be solved. Besides, it is necessary to ameliorate process efficiency due to the introduction of expensive metal electrodes and charge transport layers through a complicated process. One of the best alternatives to solving these problems is the manufacture of PSCs using a carbon electrode, which is an inexpensive and stable material and doesn't require the hole conductor.

Carbon electrode-based perovskite solar cells (C-PSCs) not only have

high stability against moisture and thermal stress but also can be manufactured by introducing electrodes through various methods (e.g. screen printing, doctor blading, spraying, roll to roll, etc.), making PSCs suitable for mass production and enlargement. However, despite process efficiency and device stability, C-PSCs are less efficient than conventional metal electrode-based PSCs because of poor physical and chemical contact between the carbon electrode and the perovskite light-absorbing layer. Therefore, for practical use of C-PSCs, it is necessary to fabricate a high performance and highly stable C-PSC by the improvement of interfacial contact.

This dissertation describes the effective strategies to improve interfacial contact between the carbon electrode and perovskite in fabricating the C-PSCs through interface engineering based on various processes and materials. Specifically, the introduction of organic and inorganic materials through a solution process to induce the growth of the interfacial layer or adjusting the interfacial energy level of carbon electrode through a plasma process. Firstly, a two-dimensional perovskite (2D PSK) interfacial layer was introduced on a fabricated C-PSC using a bulky organic ligand (phenylethyl ammonium iodide, PEAI) solution. Introduced 2D PSK interfacial layer improved hole extraction

ability, and inhibited interfacial charge recombination due to the aligned energy level. These results induced the performance of C-PSC. Also, it was confirmed that the stability of the device was further improved because the 2D PSK has high moisture and thermal stability. Secondly, a colloidal lead iodide (PbI_2) capped with organic acids, that can be dispersed in a non-polar solvent was additionally introduced at the interface of the carbon/perovskite for the enhanced the interfacial contact. The prepared colloidal PbI_2 was introduced at the interface without damaging the fabricated C-PSCs, and secondary growth of methylammonium lead iodide (MAPbI_3) interfacial layer was induced by additional MAI (methylammonium iodide) treatment on the colloidal PbI_2 -treated C-PSC. Secondary growth of the MAPbI_3 interfacial layer significantly improved device performance by maximizing the interfacial contact between the carbon electrode and perovskite layer compared to previous studies that induced performance enhancement by the additional introduction of organic ligands. Moreover, the device stability was improved due to the hydrophobic organic acid present during the formation of the interfacial MAPbI_3 layer. Thirdly, the carbon electrode, in which fluorine atoms were introduced in a concentration gradient, was prepared based on the plasma process. As fluorine atoms

having strong electron-withdrawing properties, were introduced into the carbon electrode, the work function of the carbon electrode and the HOMO energy level of the perovskite are well aligned with each other, thereby improving hole transporting ability, followed by the enhanced device performance. In addition, hydrophobic fluorine atoms were introduced into the hydrophobic carbon electrode, and C-PSCs having maximum moisture stability was produced by synergy effect. Accordingly, this study provides several strategies to further improve the long-term stability of PSCs, as well as how to improve the performance of C-PSC through various processes and materials-based interface engineering.

Keywords: Perovskite solar cell, Screen-printable carbon electrode, Interface engineering, 2D/3D hybrid perovskite, Colloidal PbI_2 , Hierarchical perovskite, Fluorine plasma treatment, Energy level alignment.

Student Number: 2017-32525

List of Abbreviations

A: active area

A_i : photoluminescence decay weight fraction

AFM: atomic force microscopy

Al_2O_3 : aluminium oxide

AVA: ammonium valeric acid

BA: n-butylammonium

BEA: benzyl ammonium

BET: Brunauer–Emmett–Teller

BJH: Barrett–Joyner–Halenda

BSE: backscattered electron image

C: carbon

CA: cyclopropylammonium

C-AFM: conductive atomic force microscopy

CB: chlorobenzene

CBM: conduction band minimum

CdTe: cadmium telluride

CF: chloroform

CIGS: $\text{CuIn}_{1-x}\text{Ga}_x\text{Se}_2$

C_n : number of carbon on alkyl chain

C-PSC: carbon electrode-based perovskite solar cell

CsAc: cesium acetate

CsI: cesium iodide

c-TiO₂: compact TiO₂

d : thickness

DCB: dichlorobenzene

DEE: diethyl ether

DI: deionized

DJ: Dion-Jacobson

DMA: *N,N*-dimethyl acetamide

DMF: *N,N*-dimethyl formamide

DMSO: dimethyl sulfoxide

D_N : donor number

DSSC: dye-sensitized solar cell

E_g : band gap

EIS: electrochemical impedance spectroscopy

EQE: external quantum efficiency

ETL: electron transport layer

EtOH: ethanol

F: fluorine

FABr: formamidinium bromide

FAI: formamidinium iodide

FC-PSC: F-doped carbon electrode-based PSC

FE-EPMA: field-emission electron probe microanalyzer

FE-SEM: field-emission scanning electron microscopy

FF: fill factor

FT-IR: Fourier-transform infrared

FTO: fluorine-doped tin oxide

FWHM: full width at half maximum

GaAs: gallium arsenide

GB: grain boundary

GBL: γ -butyrolactone

h: hour

HCl: hydrochloric acid

HOMO: highest occupied molecular orbital

HR-TEM: high-resolution transmission electron microscopy

HSP: Hansen's solubility parameters

HTL: hole transport layer

HTM: hole transport material

I: iodine

IPA: isopropanol

IPCE: incident photon-to-current efficiency

ITO: indium tin oxide

$I-V$: current–voltage

J_{sc} : short-circuit current density

$J-V$: current density–voltage

Li-TFSI: lithium bis(trifluoromethylsulphonyl)imide

LUMO: lowest unoccupied molecular orbital

MABr: methylammonium bromide

MAI: methylammonium iodide

MAPbI₃: methylammonium lead iodide (CH₃NH₃PbI₃)

meso-TiO₂: mesoporous TiO₂

min: minute

mL: milliliter

nm: nanometer

ns: nanosecond

n_{traps} : trap density

OPV: organic photovoltaic

pa: picoampere

Pb: lead

PbBr₂: lead (II) bromide

PbI₂: lead (II) iodide

PCE: power conversion efficiency

PEA: phenylethylammonium

PEAI: phenylethylammonium iodide

PMMA: poly (methyl methacrylate)

ps: picosecond

PS: polystyrene

PSC: perovskite solar cell

PSK: perovskite

PTFE: polytetrafluoroethylene

PV: photovoltaic

QD: quantum dot

R_{ct} : charge transfer resistance

R_{rec} : charge recombination resistance

R_s : series resistance

RH: relative humidity

RP: Ruddlesden-Popper

R-PSK: reference triple cation perovskite

s: second

SAED: selected area diffraction

SCLC: space-charge-limited current

SG-PSK: perovskite layer with secondary grown MAPbI₃ interface

Spiro-OMeTAD: 2,2',7,7'-tetrakis(*N,N*-di-*p*-methoxyphenylamine)-9,9'-spirobifluorene

SPO: stabilized power output

SSPL: steady-state photoluminescence

TCO: transparent conductive oxide

TCSPC: time-correlated single-photon-counting

TEM: transmission electron microscopy

TiO₂: titanium dioxide

TOL: toluene

TOPO: trioctylphosphine oxide

Triple cation (-mixed halide) perovskite: Cs_{0.05}MA_{0.16}FA_{0.79}Pb(I_{0.84}Br_{0.16})₃

TRPL: time-resolved photoluminescence

TTIP: titanium isopropoxide

UPS: ultraviolet photoelectron spectroscopy

UV-Vis: ultraviolet–visible

VBM: valence band maximum

V_{oc} : open-circuit voltage

V_{TFL} : trap-filled limit voltage

WF: work function

W/O: without

XRD: x-ray diffraction

XPS: x-ray photoelectron spectroscopy

Zn: zinc

ZrO₂: zirconium dioxide

2D PSK: two-dimensional perovskite

3D PSK: three-dimensional perovskite

μm: micrometer

μL: microliter

ε: relative dielectric constant

ε₀: free space permittivity

η: efficiency

θ: theta

k : Boltzmann's constant

μ: charge carrier mobility

σ₀: direct current conductivity

τ: photoluminescence decay time constant

List of Figures

- Figure 1.** Comparison of the increasing rate in perovskite solar cell efficiencies.
- Figure 2.** The crystalline structure of cubic perovskite ABX_3 ; A: large cations, such as organic ligands (MA^+ , FA^+) or alkali metals (Rb^+ , Cs^+); B: small cations, such as Pb^{2+} , Sn^{2+} ; X: halogen ions, such as I^- , Br^- , Cl^- or SCN^- .
- Figure 3.** (a) Alterations of perovskite thin-film surface and light absorption ability and crystalline according to composition control of X position with a various molar ratio. (b) Evolution of photon-to-electron conversion properties of Pb-Sn alloyed perovskite, which was prepared by control a mixing ratio at position B.
- Figure 4.** Research direction that contributes to commercialization of PSCs. (a) Development of scalable methods for perovskite deposition, (b) fabrication of PSC module and panel with large operational areas, and (c) long-term stable perovskite film under ambient moisture by incorporating small organic molecule.

- Figure 5.** Various structural configurations of PSCs; (a) regular type of mesoporous n-i-p, (b) inverted type of p-i-n, (c) regular type of planar n-i-p, and (d) perovskite tandem cell.
- Figure 6.** Decomposition at the metal cathode / spiro-OMeTAD HTM / perovskite interface of PSC in a typical humid and thermal stress; (a) Hypothesis of perovskite film degradation in a humid condition, and (b) diffusion of Au electrode of PSCs after thermal stimulation.
- Figure 7.** Numerous external factors affecting PSC stability and considerations for improving device stability.
- Figure 8.** Device architectures of (a) a fully printable C-PSC, and (b) a paintable C-PSC.
- Figure 9.** Numerous attempts to improve performance of HTM-free C-PSCs, such as (a) introduction of various type of carbon sources (carbon black, carbon nanotube, graphite), (b) and (c) increasing the contact surface area of carbon electrodes, (d) boron-doping on carbon electrode, and (e) carbon electrode introduction by hot-pressing.
- Figure 10.** (a) Schematic illustrations of PSC and interfacial charge transport pathway. (b) Schematic diagram of interfacial

charge dynamics: 1) photo-generated excitons separated by free carriers; 2) charge diffusion from the center to the interface (1 ps to 1 ns); 3) extraction of electric charges into ETL and HTL by the interfacial electric field (< 100 ps); 4) charge recombination induced by interfacial trap states (1 ns to 1 μ s); 5) interfacial back charge transfer (1 μ s to 1 ms); and 6) charge accumulation induced by ion migration (>1 s).

Figure 11. Various strategies of interface engineering for high efficient and stable PSC.

Figure 12. Schematic illustration of perovskite precursor and solvent interaction in various polar solvents.

Figure 13. Variation of manufactured perovskite films according to various anti-solvent treatments.

Figure 14. Several approaches of solution process-based interfacial engineering, such as (a) passivation layer through the introduction of quaternary ammonium halide, (b) introduction of the polymer as a moisture permeation inhibiting layer, (c) insulating buffer layer introduced to suppress the charge recombination, and (d) perovskite QD for interfacial energy level control.

Figure 15. Numerous interface engineering studies to improve performance of HTM-free C-PSCs, such as (a) defect passivation via a simple post-treatment of trioctylphosphine oxide (TOPO) ligands, (b) in situ cation exchange by cesium acetate (CsAc) treatment, and (c) dropping of the anti-solvent containing carbon nanotube during perovskite crystal formation.

Figure 16. (a) Crystal structures of 2D PSK from 3D PSK through insertion of organic spacer in $\langle 100 \rangle$ lattice direction. (b) Comparison between Dion-Jacobson (DJ) type and Ruddlesden-Popper (RP) perovskite. (c) Illustration of quasi-2D PSK formed by number of n .

Figure 17. (a) Moisture stability and (b) bandgap control according to n -value control of 2D PSK.

Figure 18. Schematic of energy band alignment according to types of 2D PSK (large- n 2D PSK, randomly mixed 2D/3D PSK, and ordered 2D/3D hybrid PSK, sequentially).

Figure 19. Various interface engineering for highly efficient and stable PSC *via* the introduction of 2D/3D hybrid perovskite; (a) 2D ligand treatment during the anti-solvent process and change

the crystallinity according to compositional ratio. (b) Improved efficiency and long-term stability by introducing the PEAI-based interface layer. (c) Change of 2D PSK crystallinity according to the alkyl chain length of 2D PSK. (d) Characterization of 2D PSK as a capping layer between HTM and 3D PSK.

Figure 20. (a) Types of defect sites that might exist on the perovskite film, and (b) schematic illustration of passivation mechanisms that can occur at the interface on perovskite.

Figure 21. (a) A mechanism for self-induced passivation of PbI_2 in perovskite film. (b) Model of the $\text{CH}_3\text{NH}_3\text{PbI}_3/\text{PbI}_2$ interface; (1) restricted current flow against PbI_2 , (2) hole injection from PbI_2 to $\text{CH}_3\text{NH}_3\text{PbI}_3$, and (3) electron injection due to band bending with generated charges and heat excitation.

Figure 22. Variation of PSC efficiency according to stoichiometric control and surface SEM image of deficient and excess PbI_2 sample.

Figure 23. Additional ligand treatment-based interfacial perovskite layer reacted with excess PbI_2 ; (a) MAI treatment, and (b)

MABr treatment.

Figure 24. Different compositions of perovskite interfacial layer formation *via* organic ligand reacted with excess PbI_2 ; (a) FABr treatment, and (b) assorted 2D ligands treatment.

Figure 25. (a) Schematic images of plasma generation (by adding energy to the material, the gas of electrons and ions is eventually produced) and properties of plasma, and (b) illustration of typical plasma equipment for surficial texturing-process.

Figure 26. Schematic diagram indicating the general purpose of the four types of plasma-based surface treatment.

Figure 27. Diverse plasma-treatment for high efficient PSC; (a) Adjusted energy level of spiro-OMeTAD through the oxygen plasma. (b) Printable C-PSC with WF controlled carbon electrode *via* oxygen plasma.

Figure 28. Schematic illustration showing the procedures to deposit a carbon electrode and induce interfacial growth of the 2D PSK layer.

Figure 29. Cross-sectional FE-SEM images of the C-PSC with the 2D PSK interfacial layer.

Figure 30. Energy band diagram of each component in the fabricated C-PSC.

Figure 31. Backscattered electron image (BSE) and elemental mapping using FE-EPMA of carbon (C) and iodine (I) in a cross-section of the fabricated C-PSC.

Figure 32. Top view of FE-SEM image w/o and with PEAI treatment.

Figure 33. (a) Full and (b) expanded range of XRD patterns of the perovskite films w/o and with PEAI treatment. Note that the carbon layer was peeled off to reveal the perovskite layer underneath for measurement.

Figure 34. SSPL of the perovskite films w/o and with PEAI treatment. (a) Samples were excited from the top surface of PSK, and (b) glass side by light irradiation at 430 nm, respectively. The carbon layer was peeled back to eliminate its quenching effect.

Figure 35. $J-V$ characteristics of C-PSCs w/o and with PEAI treatment as a function of scan direction.

Figure 36. $J-V$ characteristic comparison for C-PSCs with (a) MAI post-treatment and (b) PEAI pre-treatment.

Figure 37. $J-V$ characteristics of the best-performing device with

2D/3D hybrid PSK.

Figure 38. Distribution of photovoltaic parameters (V_{oc} , FF, J_{sc} , and PCE) of C-PSCs w/o and with PEAI treatment. The mean values are marked as solid lines in the boxes.

Figure 39. (a) The steady-state V_{oc} curves measured under 1 sun illumination of each type. (b) IPCE spectra of C-PSCs w/o and with PEAI treatment. The integrated J_{sc} is 20.54 and 21.56 mA cm⁻², respectively. (c) steady-state performance measured at V_{max} of 0.785 V, and (d) device performance with an active area of 1 cm². The inset displays a digital photograph of C-PSC with PEAI post-treatment; the dashed green square represents an active area.

Figure 40. $I-V$ characteristics for carbon electrodes w/o and with PEAI treatment.

Figure 41. TRPL decay curves for perovskite films w/o and with PEAI treatment. The samples were prepared on glass and examined (a) w/o carbon (likewise for SSPL measurements) and (b) with carbon. The samples were excited from the glass side by light irradiation at 405 nm.

Figure 42. The V_{oc} as a function of light intensity for PSCs w/o and with

PEAI treatment plotted on a semi-log scale.

Figure 43. Nyquist plots for PSCs (a) w/o and (b) with PEA treatment measured under illumination at different applied bias ranged from 0 V to 1.0 V. The scanning frequency ranged from 1 MHz to 1 Hz. The inset shows the equivalent circuit.

Figure 44. $J-V$ characteristic for a conventional PSC with FTO / TiO₂ / 3D PSK / spiro-OMeTAD / Au structure.

Figure 45. (a) The PCE evolution of a conventional PSC with an FTO / TiO₂ / 3D PSK / spiro-OMeTAD / Au structure, and C-PSCs w/o and with PEA treatment under ambient conditions (temperature: 25 °C, relative humidity: 40 ± 5%). (b) Normalized PCE evolution of the PSCs as a function of heating time at 100 °C (0 – 180 min) and 150 °C (180 – 390 min).

Figure 46. (a) Digital photograph of colloidal PbI₂ solution dispersed in chlorobenzene. (b) Proposed chemical reaction mechanisms of carboxylic acids and PbI₂.

Figure 47. (a) FE-SEM image of spin-coated colloidal PbI₂ on Si wafer. (b) TEM image of the colloidal PbI₂. (c) HR-TEM image of colloidal PbI₂. (d) SAED pattern of colloidal PbI₂.

- Figure 48.** XRD patterns of pristine PbI_2 powder and prepared colloidal PbI_2 with typical PbI_2 peaks.
- Figure 49.** Schematic illustration showing the procedures to deposit a carbon electrode and induce interfacial growth of MAPbI_3 layer based on the introduction of colloidal PbI_2 .
- Figure 50.** Digital photograph of pristine C-PSC, PbI_2 -treated C-PSC, and C-PSC with secondary growth of MAPbI_3 interfacial layer.
- Figure 51.** Cross-sectional and surficial FE-SEM images of the deposited carbon electrode using for specific surface area analysis.
- Figure 52.** BET surface analysis of the carbon electrode. The inset indicates the distribution of average pore diameter.
- Figure 53.** Elemental mapping using FE-EPMA of carbon (C), lead (Pb), and iodine (I) in a cross-section of the fabricated C-PSC w/o treatment, and with secondary growth of MAPbI_3 interfacial layer.
- Figure 54.** Surficial FE-SEM images showing perovskite films (a) w/o and with (b) colloidal PbI_2 and (c) secondary grown MAPbI_3 interfacial layer.

Figure 55. Surficial AFM images indicating perovskite films (a) w/o and with (b) colloidal PbI_2 and (c) secondary grown MAPbI_3 interfacial layer.

Figure 56. (a) Full and (c, d) expanded range of XRD patterns, including (b) FWHM of specific peaks, of the perovskite films w/o and with colloidal PbI_2 and secondary growth MAPbI_3 interfacial layer treatment.

Figure 57. (a) Full range and (b) enlarged range of FT-IR spectra of the perovskite films w/o and with colloidal PbI_2 and secondary growth of MAPbI_3 interfacial layer treatment.

Figure 58. SSPL spectra for (a) fluorescence of PbI_2 and (b) perovskite films w/o and with colloidal PbI_2 and secondary grown MAPbI_3 interfacial layer.

Figure 59. (a) $J-V$ characteristics and (b) IPCE spectra of pristine C-PSC and post-treated C-PSC with colloidal PbI_2 and sequential MAI treatment. (c) Performance data of the champion device. (d) Comparison of $J-V$ characteristics according to the chain length of organic acid.

Figure 60. Variation and comparison of the PV parameters such as V_{oc} , J_{sc} , FF, and PCE of the C-PSC w/o and with colloidal PbI_2

and MAI treatment. These parameters were evaluated from 26 devices fabricated for each concentration.

Figure 61. J - V characteristic of the device with an active area of 1 cm^2 .

The inset shows a digital photograph of C-PSC with MAPbI_3 interfacial layer and the dashed orange square represents an active area.

Figure 62. Stabilized photocurrent and PCE of secondary-grown MAPbI_3 -based C-PSCs fabricated by optimized condition, measured at the maximum power point (0.847 V) for 100 s.

Figure 63. SSPL decay curve according to the introduction of MAPbI_3 interfacial layer (excitation wavelength: 420 nm).

Figure 64. TRPL decay curves extracted from untreated and treated-samples (a) w/o and (b) with carbon electrode. TRPL spectra were recorded under exposure to 520 nm pulse laser.

Figure 65. (a) Overall UPS spectra of control and SG-PSK based on C-PSCs; (b) and (c) the expanded spectra at secondary electron cutoff and fermi-edge regions, respectively. (d) UV-vis absorption spectra of pristine triple cation perovskite and secondary-grown perovskite film. (e) Optical band gap energy determination *via* Tauc plot analysis.

Figure 66. Energy level diagram of the component layers in the C-PSC with the introduction of colloidal PbI_2 and MAPbI_3 interfacial layer.

Figure 67. Nyquist plots of the C-PSCs (a) without treatment and with secondary grown- MAPbI_3 interfacial layer, and (b) with the treatment of adjusted alkyl chain length of organic acid in colloidal PbI_2 solution, which are measured under illumination at 1.0 V bias.

Figure 68. (a) J - V characteristics for hole only devices based on FTO / PEDOT:PSS / triple cation PSK / (MAPbI_3) / carbon electrode structure (inset) and the calculated electrical conductivity (σ_0). (b) The SCLC region of dark current-voltage (J_d - V) characteristics for controlled hole only devices with V_{TFL} kink point and the n_{trap} .

Figure 69. C-AFM current mapping images of perovskite films (a) w/o and with (b) secondary grown- MAPbI_3 interfacial layer treatment under room light condition with a bias of 1.0 V, respectively.

Figure 70. (a) Histogram of the PCE values obtained from 30 C-PSC w/o ($\text{PCE}_{\text{avg}} = 12.93\%$) and with secondary growth of

MAPbI₃ interfacial layer (PCE_{avg} = 16.30%). (b) *J-V* curves of each type of PSC measured by forward and reverse scans where the hysteresis was alleviated by the introduction of MAPbI₃ interfacial layer.

Figure 71. Normalized PCE evolution of C-PSC w/o and with treatment PbI₂ and sequential MAI for secondary growth of MAPbI₃ interfacial layer, stored in the controlled ambient conditions (temperature = 25 °C, relative humidity = 40 ± 5%).

Figure 72. Schematic illustration of the FC-PSC fabrication process.

Figure 73. XPS spectra of a carbon electrode and F-doped carbon electrode. (a) XPS survey spectra. (b), (c), and (d) F1s, O1s, and C1s XPS spectra, respectively.

Figure 74. XPS spectra exhibiting deconvolution curves of C1s (a) without F plasma treatment and (b) with F plasma treatment, respectively.

Figure 75. (a) FT-IR spectra of C-PSC w/o and with F plasma treatment. (b) Raman spectra and calculated intensity ratio of C-PSC and FC-PSC.

Figure 76. BSE image and FE-EPMA elemental mapping of carbon (C) and fluorine (F) atom in a cross-section of fluorine-doped

carbon electrode.

Figure 77. J - V characteristics of PSCs w/o and with F plasma treatment.

Figure 78. (a) J - V characteristics of carbon-based PSCs w/o and with F plasma treatment as a function of scan direction. (b) PCE distribution for 40 C-PSC and FC-PSC devices, respectively. (c) Stabilized V_{oc} and PCE of each device. (d) IPCE spectra for C-PSC and FC-PSC.

Figure 79. J - V characteristics of the best-performing device (active layer size: 0.132 cm^2).

Figure 80. J - V characteristics of the device with an active area of 1 cm^2 .

Figure 81. (a) Whole UPS spectra, and (b) magnified view of the secondary electron cut-off region of w/o and with F plasma-treated cell.

Figure 82. Energy band diagram of each component in the fabricated C-PSC w/o and with F-plasma treatment, showing the separation and transport of photo-generated carriers.

Figure 83. (a) TRPL decay curve for C-PSC and FC-PSC sample. (b) Nyquist plots of C-PSC and FC-PSC devices (inset: the equivalent circuit diagram).

Figure 84. I - V curves of the carbon electrode without and with F plasma

treatment (CE: Carbon electrode, FPCE: Fluorine plasma-treated carbon electrode).

Figure 85. Long-term stability of the C-PSC and FC-PSC devices under controlled ambient conditions (temperature: 25 °C; relative humidity: $40 \pm 5\%$).

Figure 86. (a) Stability test of the C-PSC and FC-PSC devices under high humidity conditions (temperature: 25 °C; relative humidity: 60 and $80 \pm 5\%$).

Figure 87. Water contact angles (a) w/o and (b) with F plasma treatment on the carbon electrode (C-PSC = 97.8° , FC-PSC = 135.5°).

Figure 88. (a) Efficiency change of w/o and with F plasma-treated device after 10 min immersion test. (b) Digital photographic and optical microscopic images of the device.

List of Tables

- Table 1.** Photovoltaic parameters C-PSCs w/o and with PEAI treatment, depending on scan direction.
- Table 2.** TRPL decay parameters for the perovskite films w/o and with PEAI treatment. The bi-exponential decay equation was used for fitting the curves.
- Table 3.** EIS parameters for the PSCs w/o and with PEAI treatment, obtained from the Nyquist plots.
- Table 4.** BET and BJH analysis parameters for the carbon electrode.
- Table 5.** Average PV parameters evaluated from 25 each type devices measured under 100 mW cm^{-2} of simulated AM 1.5G illumination.
- Table 6.** TRPL decay parameters for the perovskite films w/o and with PbI_2 and additional MAI treatment. The bi-exponential decay equation was used for fitting the curves.
- Table 7.** Comparison of parameters related to energy level of C-PSC w/o and with MAPbI_3 interfacial layer.
- Table 8.** EIS parameters of the C-PSCs w/o and with secondary grown- MAPbI_3 interfacial layer, obtained by fitting the

Nyquist plots. Note that the alkyl chain length of colloidal PbI_2 was controlled butyric acid to octanoic acid.

Table 9. PV parameters of C-PSC w/o and with secondary growth of MAPbI_3 interfacial layer as a function of scan direction.

Table 10. Elemental composition of the carbon electrode w/o and with F plasma treatment.

Table 11. Raman spectra peak positions and intensity ratio.

Table 12. PV parameters of C-PSC w/o and with F plasma treatment according to scan direction.

Table 13. PV parameters of best performing C-PSC with F plasma treatment, compared with average of 40 FC-PSCs.

Table 14. TRPL decay parameters for the perovskite films w/o and with F plasma treatment on the carbon electrode. The curves were fitted with the bi-exponential decay equation.

Table 15. EIS results of w/o and with F plasma treatment on the carbon-based PSC.

Table of Contents

Abstract	i
List of Abbreviations	v
List of Figures	xii
List of Tables	xxviii
Table of Contents	xxx
1. Introduction	1
1.1. Background	1
1.1.1. Organic-inorganic halid perovskite solar cells (PSCs)	1
1.1.2. Device architecture and fabrication of PSCs.....	8
1.1.3. Carbon electrode-based PSCs (C-PSCs).....	13
1.1.4. Interface engineering of PSCs	19
1.1.4.1. Interface engineering based on solution process	23
1.1.4.1.1. 2D/3D hybrid PSCs based on bulk organic ligands....	29
1.1.4.1.2. Interfacial passivated-PSCs based on excess PbI ₂	36
1.1.4.2. Interface engineering based on plasma process.....	44
1.2. Objectives and Outlines	49

1.2.1. Objectives.....	49
1.2.2. Outlines	50
2. Experimental Details	52
2.1. Interface engineering of C-PSCs based on 2D perovskite interfacial layer	52
2.1.1. Fabrication of C-PSCs with 2D perovskite interfacial layer	52
2.1.2. Characterization of C-PSCs with 2D perovskite interfacial layer.....	55
2.2. Interface engineering of C-PSCs based on secondary growth of MAPbI₃ interfacial layer.....	57
2.2.1. Preparation of Colloidal PbI ₂ Solution.....	57
2.2.2. Fabrication of C-PSCs with secondary growth of MAPbI ₃ interfacial layer	57
2.2.3. Characterization of C-PSCs with secondary growth of MAPbI ₃ interfacial layer	59
2.3. Interface engineering of C-PSCs based on energy level adjustment <i>via</i> F-plasma treatment.....	63
2.3.1. Fabrication of C-PSCs with F-doped carbon	63
2.3.2. Characterization of C-PSCs with F-doped carbon.....	65

3. Results and Discussion	67
3.1. Interface engineering of C-PSCs based on 2D perovskite interfacial layer	67
3.1.1. Fabrication of interface-engineered C-PSCs with 2D perovskite	67
3.1.2. Photovoltaic performance of interface-engineered C-PSCs with 2D perovskite.....	79
3.1.3. Interfacial charge carrier dynamics in interface-engineered C-PSCs with 2D perovskite.....	88
3.1.4. Device stability of interface-engineered C-PSCs with 2D perovskite	97
3.2. Interface engineering of C-PSCs based on secondary growth of MAPbI₃ interfacial layer.....	102
3.2.1. Synthesis of colloidal PbI ₂ and fabrication of C-PSCs with MAPbI ₃ interfacial layer	102
3.2.2. Characterization of colloidal PbI ₂ -based MAPbI ₃ interfacial layer.....	115
3.2.3. Photovoltaic performance of C-PSCs with MAPbI ₃ interfacial layer.....	124
3.2.4. Interfacial charge carrier dynamics in C-PSCs with MAPbI ₃ interfacial layer	132
3.2.5. Device hysteresis and long-term stability of C-PSCs with MAPbI ₃ interfacial layer	147

3.3. Interface engineering of C-PSCs based on energy level adjustment <i>via</i> F-plasma treatment.....	153
3.3.1. Fabrication of F-doped C-PSCs.....	153
3.3.2. Photovoltaic performance of the F-doped C-PSCs.....	162
3.3.3. Interfacial charge carrier dynamics in F-doped C-PSCs....	170
3.3.4. Ambient and moisture stabilities of F-doped C-PSCs	178
4. Conclusion	184
References	189
국문초록	204

1. Introduction

1.1 Background

1.1.1. Organic-inorganic halide perovskite solar cells (PSCs)

Recently, the global interest in environmental issues such as global warming, fine dust and environmental depletion due to an increase in the usage of fossil fuels has been higher than ever. For this reason, it is necessary to develop sustainable energy that considers the environment as an alternative resource for the next generation [1]. Solar energy, the cleanest and most available energy resource, can meet the growing global energy demands in an eco-friendly way [2]. Because of the suitability of solar energy as a renewable alternative energy source, scientists have developed various types of photovoltaic (PV) devices for decades, such as Si-based solar cell [3], GaAs [4], $\text{CuIn}_{1-x}\text{Ga}_x\text{Se}_2$ (CIGS) [5] and CdTe solar cells [6], organic photovoltaics(OPVs) [7], and dye-sensitized solar cells (DSSCs) [8]. However, high production costs and limitations in large-scale production have restricted to a wide range of applications in everyday life due to the characteristics of the above PV device components (lack of elements, rare metals, toxicity, poor efficiency, etc.) [9].

Since its inception in 2009 by Kojima *et al.* [10], PSCs have attracted remarkable attention in PV research due to their great potential as next-generation photovoltaics. Over the past decade, technological innovation of PSC has progressed at an unprecedented rate (**Figure 1**) [11], and the state of the art PSC has the highest power conversion efficiency (PCE) of 25.2 % in 2020 in single-junction architecture [12, 13]. The perovskite has a specific crystal structure with ABX_3 formula in which organic and inorganic materials are mixed as a various constitutional combinations [A = $CH_3NH_3^+$ (methylammonium, MA^+), $CH(NH_2)_2^+$ (formamidinium, FA^+) or alkali metals (Rb^+ , Cs^+); B = Pb^{2+} , Sn^{2+} ; X = I^- , Br^- , Cl^- or SCN^-] (**Figure 2**) [14].

This light-absorbing material has the intrinsic photoelectric characteristics, e.g. broad optical absorption spectrum (UV to NIR region) [15], high optical absorption coefficient ($\sim 10^5 \text{ cm}^{-1}$) [16], low Urbach energy (15 meV) [17], high charge carrier mobility ($> 20 \text{ cm}^2 \text{ V}^{-1} \text{ s}^{-1}$) [18], low trap-state density ($n_{\text{traps}} = 10^9 \text{ to } 10^{10} \text{ cm}^{-3}$) [19], long carrier diffusion length ($\sim 175 \text{ }\mu\text{m}$) [20] and a clear ambipolar carrier transport characteristics [21], which can be further reinforced or modified through compositionally modulating the ratio of cations and halides (**Figure 3**) [22, 23].

PSCs can be simply fabricated by the solution process under the low temperature and ambient atmospheric condition, which means significant cost-competitiveness, and lower restriction on the manufacturing process. Owing to such economic benefits and superior performance of over 25%, the interest of researches is increasingly focusing on commercializing PSCs beyond improving the performance of PSCs. To approach the commercialization of PSCs soon, a great deal of efforts has focused on (i) scalable coating processes [24], (ii) large area PSC modules and panels [25], and (iii) high stability against ambient air [26], heat [27], light [28], and moisture (**Figure 4**) [29].

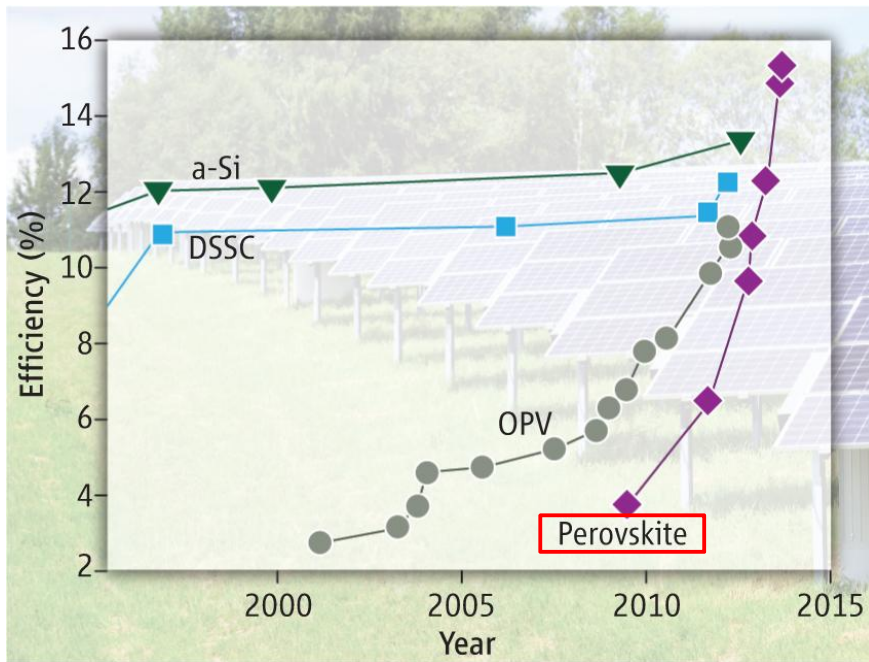


Figure 1. Comparison of the increasing rate in perovskite solar cell efficiencies (purple lines and markers) [11].

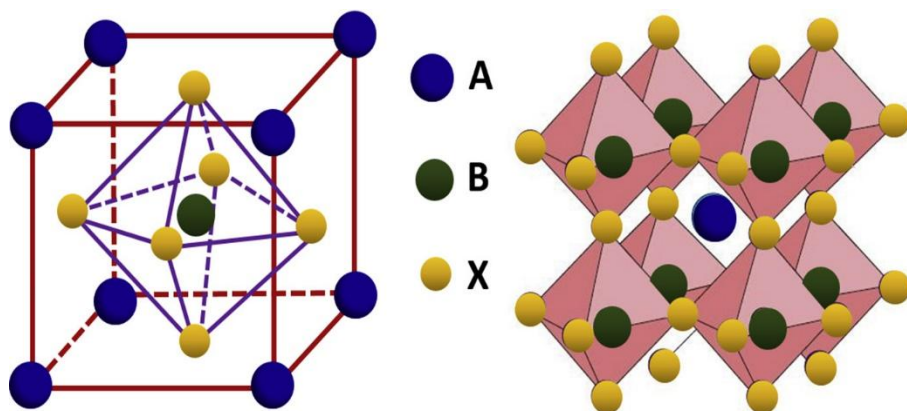


Figure 2. The crystalline structure of cubic perovskite ABX_3 ; A: large cations, such as organic ligands (MA^+ , FA^+) or alkali metals (Rb^+ , Cs^+); B: small cations, such as Pb^{2+} , Sn^{2+} ; X: halogen ions, such as I^- , Br^- , Cl^- or SCN^- [14].

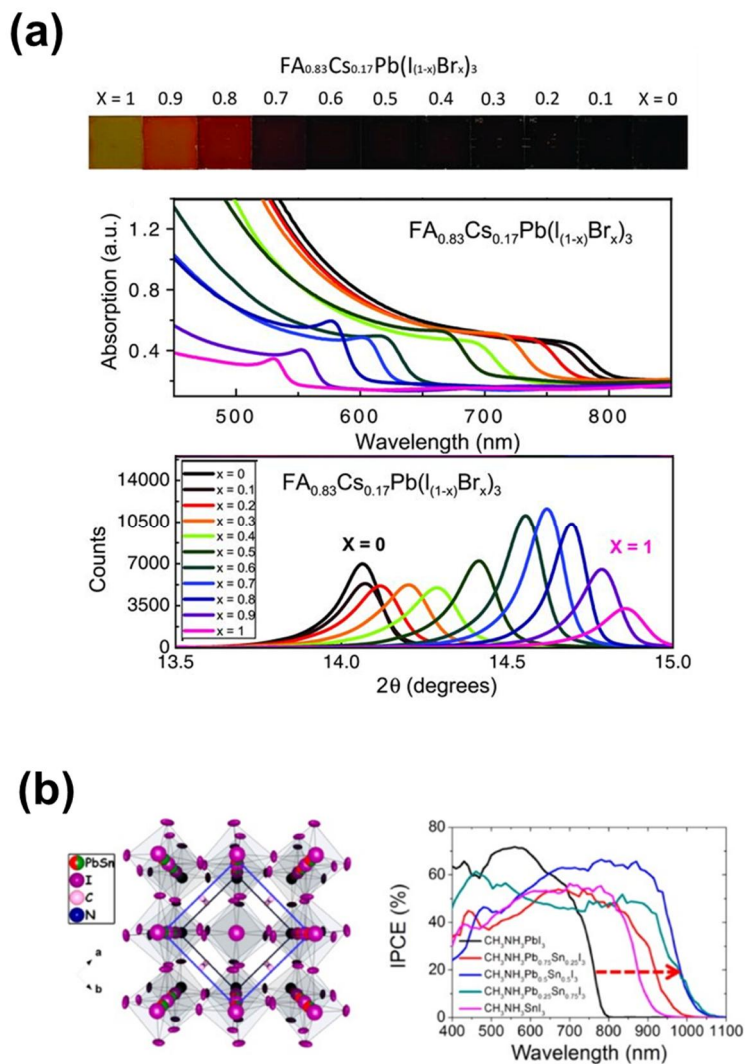


Figure 3. (a) Alterations of perovskite thin-film surface and light absorption ability and crystalline according to composition control of X position with a various molar ratio [22]. (b) Evolution of photon-to-electron conversion properties of Pb-Sn alloyed perovskite, which was prepared by control a mixing ratio at position B [23].

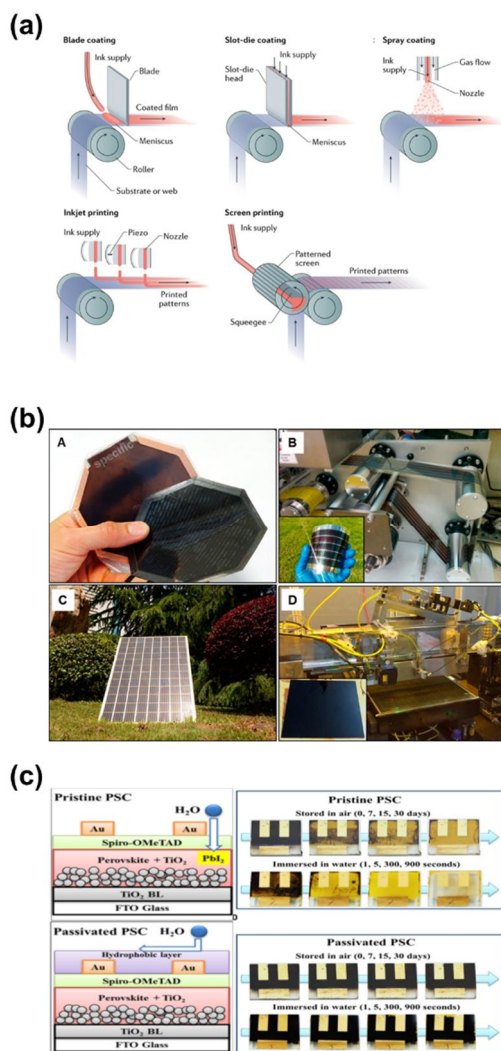


Figure 4. Research direction that contributes to the commercialization of PSCs. (a) Development of scalable methods for perovskite deposition [24], (b) fabrication of PSC module and panel with large operational areas [25], and (c) long-term stable perovskite film under ambient moisture by incorporating small organic molecule [26].

1.1.2. Device architecture and fabrication of PSCs

Generally, PSC is a stacked device consisting of a transparent conductive oxide (TCO) coated glass substrate, an n-type semiconductor as an electron transport layer (ETL), a perovskite as a light-absorbing layer, a semiconductor as a p-type hole transport layer (HTL), and a back contact metal electrode (Au or Ag). The device configuration can be commonly classified into three types according to the stacking order of composition layers and the direction of charge carrier transport. The device structure can be conventionally classified into three types according to the stacking order of the composition layers and the direction of charge carrier transport: (i) mesoscopic PSCs composed of TCO / compact ETL / mesoporous ETL / perovskite / HTL / metal, (ii) regular type of planar “n–i–p” PSCs comprised of TCO / compact ETL / perovskite / HTL / metal, and (iii) inverted type of planar “p–i–n” PSCs made up of TCO / HTL / perovskite / ETL / metal [30]. More recently, multi-junction PV devices (perovskite tandem structures), in which two band gap matched absorbers, have been monolithically stacked have demonstrated a possibility for low cost and potential to exceed single junction efficiency limits [31]. Each of device types described above is shown in **Figure 5**, respectively [32].

Among various structures, for example, a specific method of manufacturing the conventional n-i-p mesoscopic PSC, a firstly attempted configuration of PSC, is as follows [10]. The device assembly begins with the introduction of ETL on the TCO substrate such as a fluorine-doped tin oxide (FTO) or indium tin oxide (ITO). The structure is then layered with a mesoporous metal oxide as ETL or structural scaffold containing the perovskite, followed by the deposition of HTL, and capped with the metal anode. Although mesoscopic PSC with TiO₂ layer achieved more than 22% PCE through high-efficient charge extraction, the device stability problem due to the intrinsic properties of components still remains [33, 34].

Most of all, device degradation that occurs in HTM and metal electrodes is related to the problem of PSC. 2,2',7,7'-tetrakis(*N,N*-di-*p*-methoxyphenylamine)-9,9'-spirobifluorene (spiro-OMeTAD) with hygroscopic lithium bis (trifluoromethylsulfonyl) imide (Li-TFSI) dopant for remarkable hole extraction properties, which is commonly used an organic small molecule-based hole transport material (HTM), seriously debases the ambient and thermal stability of PSC [35]. Corrosion of metallic electrode by diffused halogen ions also causes device deterioration (**Figure 6**) [36]. Furthermore, HTMs and precious

metal electrodes are expensive materials, and especially metal electrodes require the thermal vapor deposition process, thus reducing the efficiency of the PSC manufacturing process.

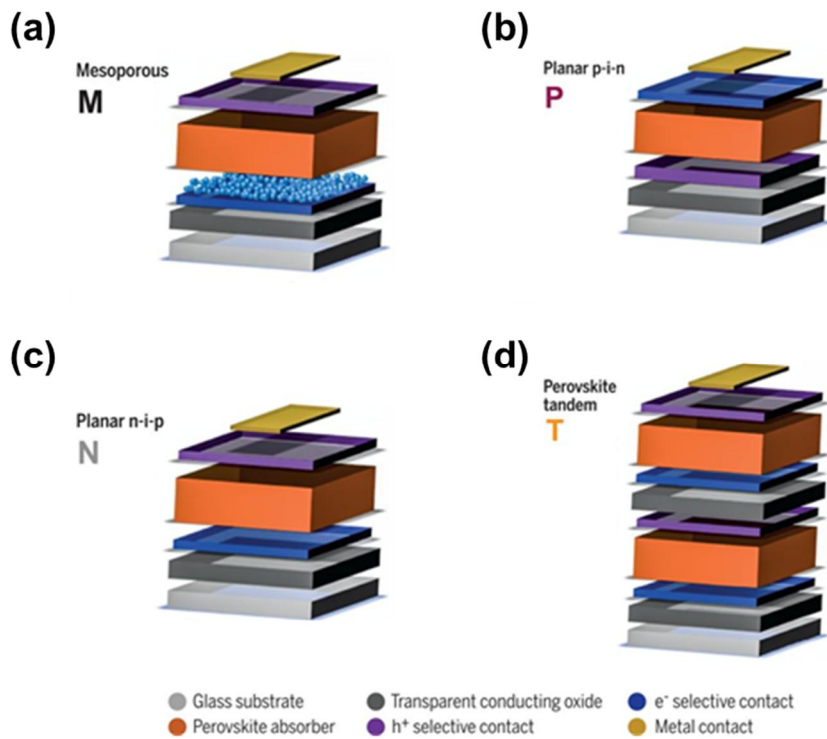


Figure 5. Various structural configurations of PSCs; (a) regular type of mesoporous n-i-p, (b) inverted type of p-i-n, (c) regular type of planar n-i-p, and (d) perovskite tandem cell [32].

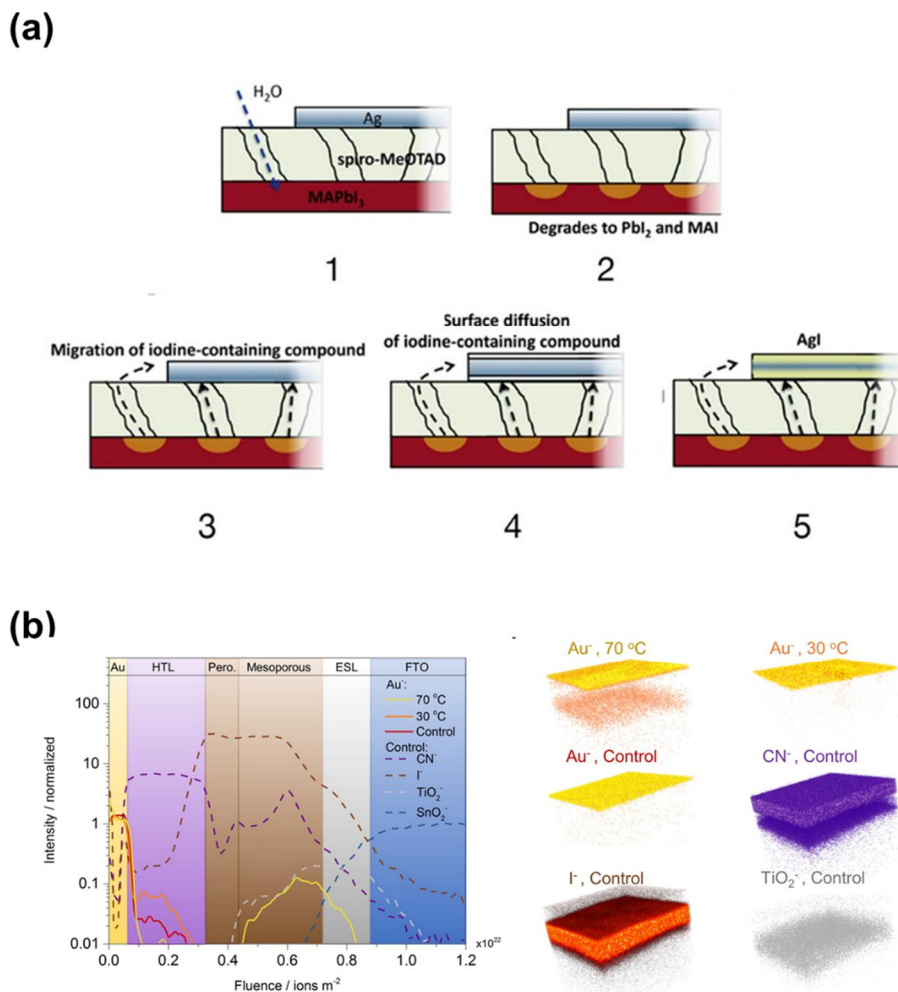


Figure 6. Decomposition at the metal cathode / spiro-OMeTAD (HTM) / perovskite interface of PSC in a typical humid and thermal stress; (a) Hypothesis of perovskite film degradation in a humid condition, and (b) diffusion of Au electrode of PSCs after thermal stimulation [37, 38].

1.1.3. Carbon electrode-based PSCs (C-PSCs)

Among the various topics investigated to accelerate the commercialization of PSC, improving the long-term stability of the device is one of the main research directions to improve the competitiveness of PSC as a next-generation energy source. To resolve the stability issues of PSC, it is the most important point to suppress degradation of a photo-active layer, charge transfer layer and electrode in the PSC due to external stimuli such as moisture, heat, and light **(Figure 7)** [34]. In particular, the decomposition of HTM and metal electrode, which are most exposed to ambient moisture in conventional PSC devices, is directly related to deteriorating PSC device performance [37]. Therefore, hole conductor-free carbon electrode-based PSCs (C-PSCs) are emerging as a replaceable PSC architecture for implementing stable devices.

The carbon electrode can simultaneously replace HTL and back contact electrode, and C-PSC also prevents performance degradation issues associated with HTM and perovskite / HTM interfaces. Especially, C-PSC is interesting and important for many researchers in terms of commercializing PSC, because it is a simple, scalable manufacturing method that is more cost-effective and easy to manage [39].

There are two types of C-PSC: (i) fully printable C-PSC with TCO / compact ETL / mesoporous ETL / insulating scaffold layer (Al_2O_3 or ZrO_2) / C architecture with post-treated perovskite layer, which was the firstly suggested by Han *et al.* with the PCE of 6.6% [40], (ii) paintable C-PSC with the architecture of TCO / compact ETL / mesoporous ETL / perovskite / C, which was the initially reported by Yang *et al.* with the PCE of 10.2% (**Figure 8**) [41]. The paintable C-PSC has a comparatively high PCE and an efficient manufacturing process since the carbon electrode is a relatively simple configuration without the HTL and insulating scaffold layer and is screen-printed directly onto a crystalline perovskite film and also without.

According to development possibilities of C-PSC, several approaches (e.g., adjustment of carbon sources [42], doping of heterogeneous elements in carbon [43], increasing the contact area of carbon electrodes [41, 44], introduction methods of carbon electrode [45, 46], etc. (**Figure 9**)) to successfully improve the efficiency of C-PSC have been tried, lately developed C-PSC with an efficiency over 15% [47]. Furthermore, the hydrophobic nature of carbon effectively prevents the penetration of moisture and greatly improves the long-term stability of PSCs [48]. Recently, Wu *et al.* showed that C-PSCs maintain 75% of their initial

efficiency under highly humid conditions ($85 \pm 10\%$ RH) for 100 h [49].

However, due to the absence of HTM and poor physical and chemical contact of the carbon electrode on the perovskite film, interfacial charge recombination and inefficient hole transport between perovskite and carbon, resulting in significantly lower efficiency of C-PSC than conventional PSC including HTM and metal electrode. Therefore, there is a necessity to suppress interfacial charge recombination and improve the interfacial contact for efficient and highly stable C-PSCs.

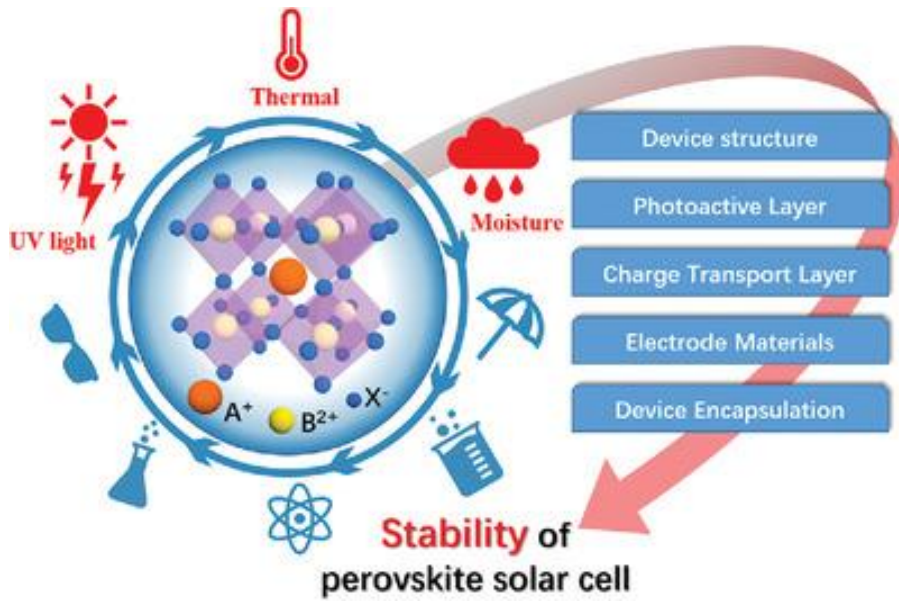


Figure 7. Numerous external factors affecting PSC stability and considerations for improving device stability [34].

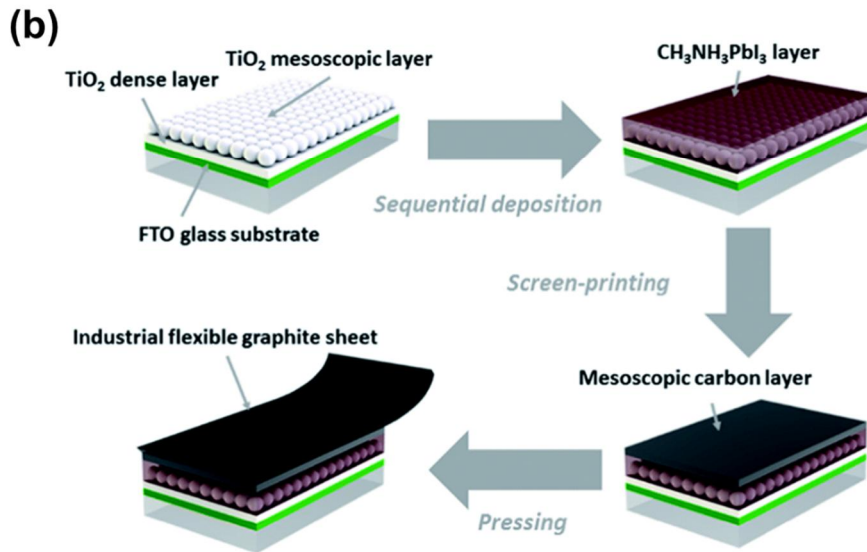
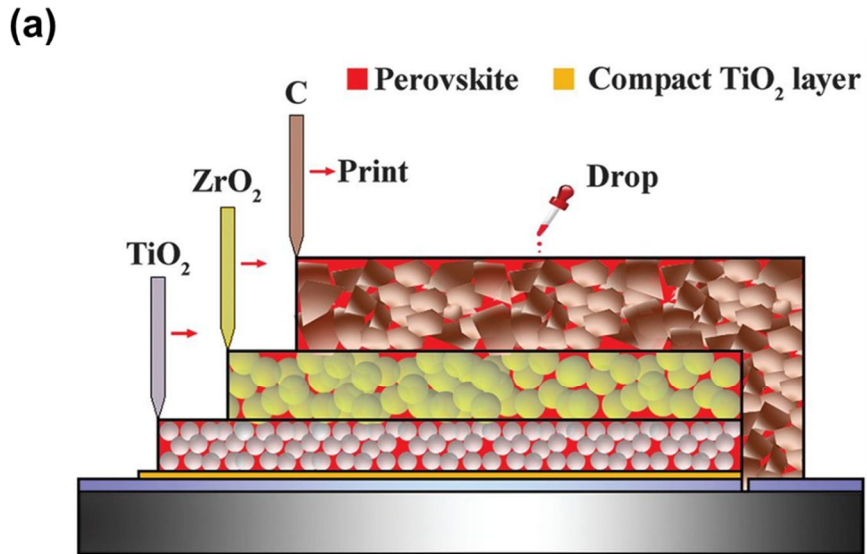


Figure 8. Device architectures of (a) a fully printable C-PSC [50], and (b) a paintable C-PSC [41].

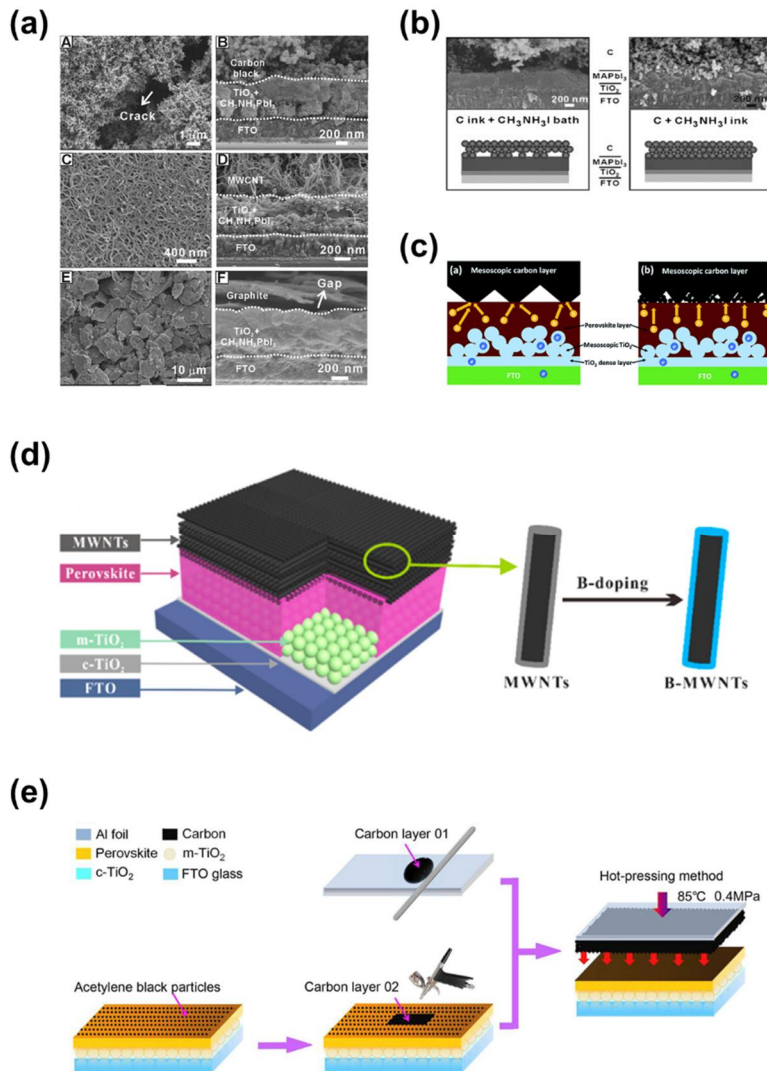


Figure 9. Numerous attempts to improve performance of HTM-free C-PSCs, such as (a) introduction of various type of carbon sources (carbon black, carbon nanotube, graphite) [42], (b) and (c) increasing the contact surface area of carbon electrodes [41, 44], (d) boron-doping on carbon electrode [43], and (e) carbon electrode introduction by hot-pressing [46].

1.1.4. Interface engineering of PSCs

The decrease in charge transfer efficiency due to charge accumulation in the charge transfer layer represents the most obvious signs such as current-voltage (I - V) hysteresis in the device and charge recombination at the interface, and these abnormal electrical behaviors are directly related to the deterioration of device performance and stability [51, 52]. Thus, apart from having appropriate materials, device structures, and good film qualities, controlling the properties of the interface is the key factor for a highly efficient and stable PSC.

Interfacial engineering is the best way to suppress undesirable charge-carrier dynamics by controlling the interface characteristics of compositional layers (TCO, ETL, perovskite, HTL and electrode) constituting the PSC (**Figure 10**) [53, 54]. The interface engineering plays an important role in improving the device performance through adjusting energy level alignment [55, 56], deactivating trap states [57, 58], blocking ion migrations [59], tuning the morphology of perovskite [60], and improving the device stability (**Figure 11**) [61]. In particular, it proved more than 21% efficiency in HTM-free PSC through efficient charge transport depending on the proper contact point of the interface [62]. This significant result demonstrated that the C-PSC, which has low

efficiency due to poor contact between the carbon electrode and the perovskite, can achieve an efficiency of 20% or more based on the improvement of interfacial contact. Therefore, HTM-free C-PSC with high efficiency and stability through interfacial engineering is a reliable candidate to replace conventional PSC.

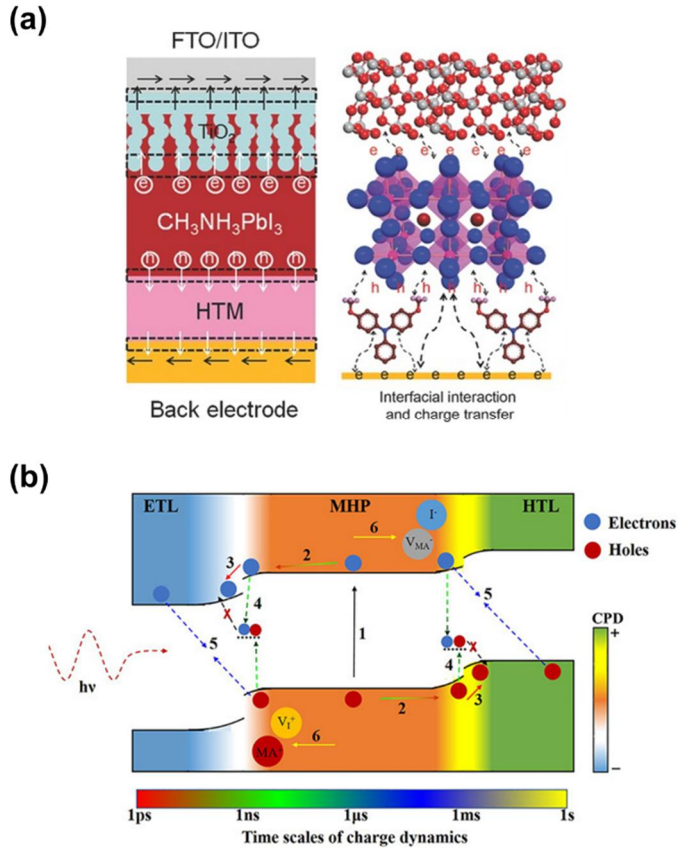


Figure 10. (a) Schematic illustrations of PSC and interfacial charge transport pathway [53]. (b) Schematic diagram of interfacial charge dynamics: 1) photo-generated excitons separated by free carriers; 2) charge diffusion from the center to the interface (1 ps to 1 ns); 3) extraction of electric charges into ETL and HTL by the interfacial electric field (< 100 ps); 4) charge recombination induced by interfacial trap states (1 ns to 1 μ s); 5) interfacial back charge transfer (1 μ s to 1 ms); and 6) charge accumulation induced by ion migration (>1 s) [54].

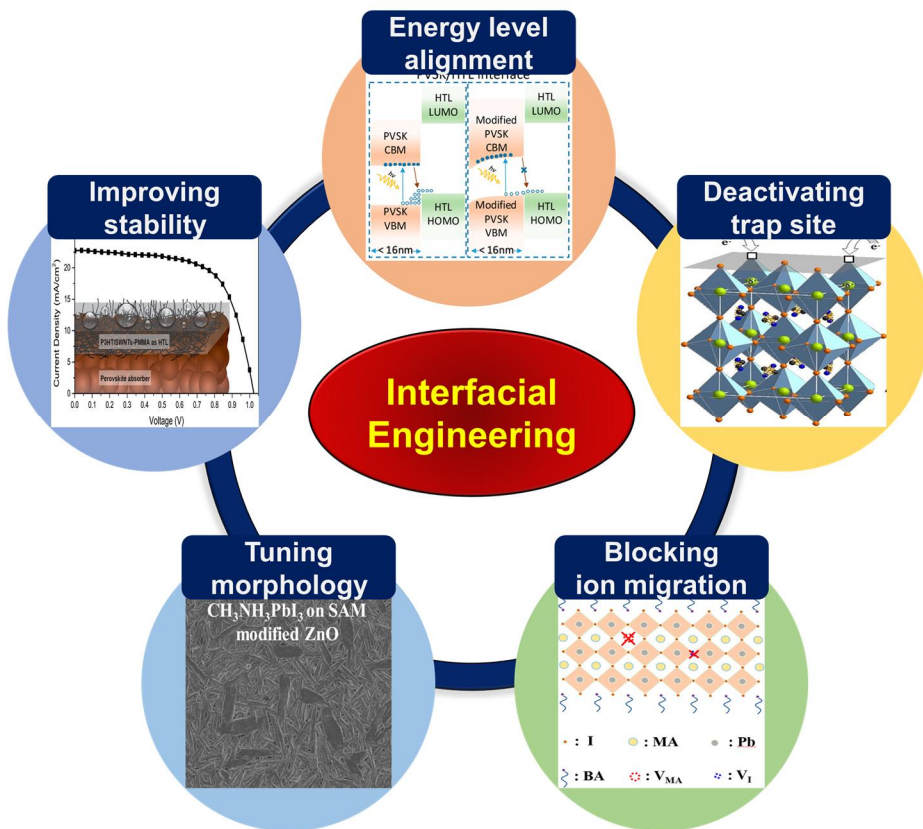


Figure 11. Various strategies of interface engineering for high efficient and stable PSC [55, 57, 59-61].

1.1.4.1. Interface engineering based on solution process

Typically, the perovskite precursor solution used for fabrication of PSCs by the solution process is prepared using a polar solvent such as *N,N*-dimethyl formamide (DMF), γ -butyrolactone (GBL), dimethyl sulfoxide (DMSO) and *N,N*-dimethyl acetamide (DMA), and treated on the substrate to introduce the perovskite layer (**Figure 12**) [63]. The fabricated perovskite crystalline layer can be easily decomposed in polar solvents with a high dipole moment and polarity, especially water molecules with high polarity are the main factor that degrades device performance by acting as a major decomposition trigger for the perovskite material itself and PSC [64]. Thus, through anti-solvent treatment, it is possible to increase the crystallinity of the perovskite film during the coating-process or introducing charge transport layers and encapsulation layers using organic, inorganic and polymer solutions based on anti-solvents.

However, anti-solvents have different effects on perovskite films depending on dielectric constant, polarity and boiling point (**Figure 13**) [65]. Although non-polar solvents (e.g. chloroform (CF), chlorobenzene (CB), toluene (TOL), dichlorobenzene (DCB) diethyl ether (DEE), and etc.) are common anti-solvents, isopropanol (IPA), a polar solvent with

a relatively low dielectric constant and boiling point, is also used to introduce various hydrophilic charge transfer layers while minimizing damage to perovskite films under controlled processes [66].

By using a non-destructive solvent for the perovskite layer in the interfacial process, significant substances (e.g. organic molecules capable of forming a passivation layer on the perovskite surface [67, 68], polymers that inhibit moisture penetration [61, 69], insulating buffer materials (PMMA or PS) that inhibit charge recombination [70, 71], and a perovskite quantum dot (QD) to control the energy level [72]), were introduced to improve the device performance and stability of the PSC (**Figure 14**).

Furthermore, many attempts have been made that are suitable for interfacial engineering to C-PSC; e.g. deactivating of trap site through defect healing with hydrophobic ligand coordination (**Figure 15a**) [73], energy level control based on surficial cation exchange of preformed perovskite film (**Figure 15b**) [74], and improving physical contact through carbon nanotubes loading based on anti-solvent treatment during crystallization (**Figure 15c**) [75], which has been well derived to improve the device performance and stability.

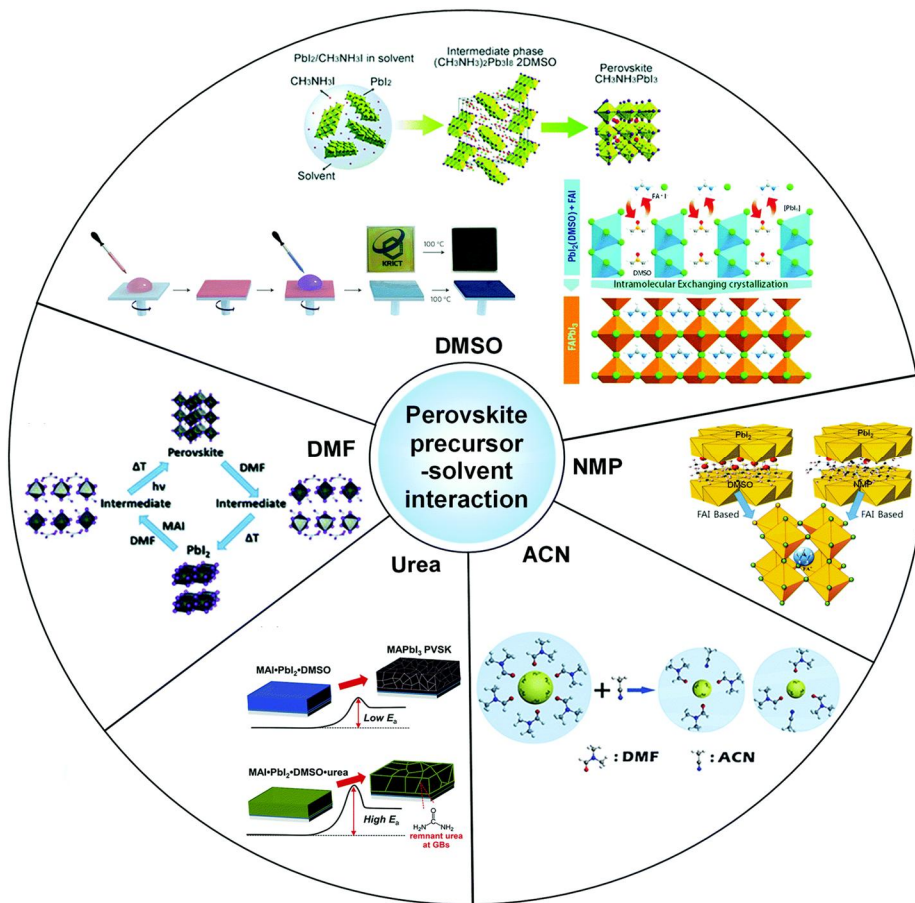


Figure 12. Schematic illustration of perovskite precursor and solvent interaction in various polar solvents [63].

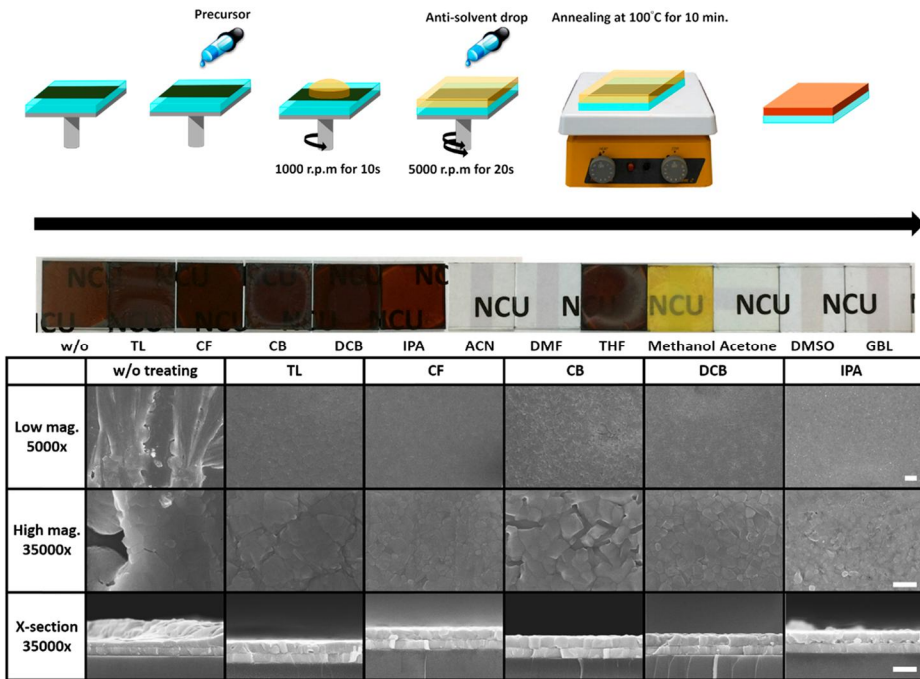


Figure 13. Variation of manufactured perovskite films according to various anti-solvent treatments [65].

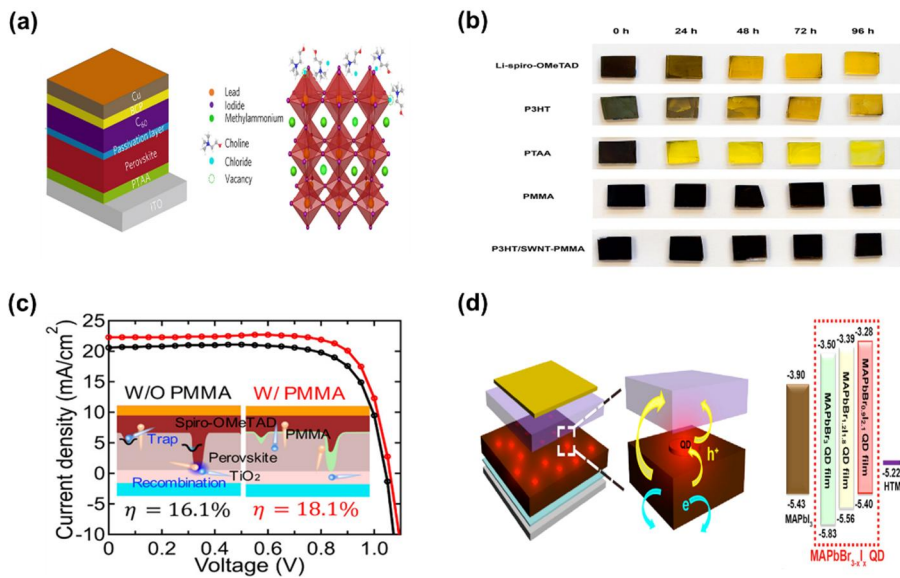


Figure 14. Several approaches of solution process-based interfacial engineering, such as (a) passivation layer through the introduction of quaternary ammonium halide [68], (b) introduction of the polymer as a moisture permeation inhibiting layer [61], (c) insulating buffer layer introduced to suppress the charge recombination [70], and (d) perovskite QD for interfacial energy level control [72].

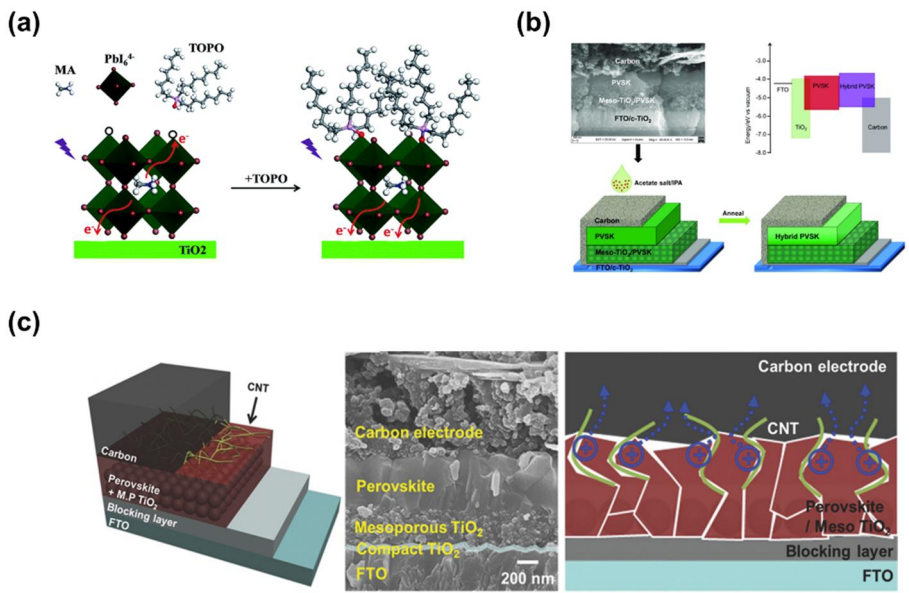


Figure 15. Numerous interface engineering studies to improve performance of HTM-free C-PSCs, such as (a) defect passivation via a simple post-treatment of trioctylphosphine oxide (TOPO) ligands [73], (b) in situ cation exchange by cesium acetate (CsAc) treatment [74], and (c) dropping of the anti-solvent containing carbon nanotube during perovskite crystal formation [75].

1.1.4.1.1. 2D/3D hybrid PSCs based on bulk organic ligands

Three-dimensional perovskite (3D PSK) has emerged as one of the most promising next-generation solar cell materials with a PCE of over 25% due to its excellent optical and physical properties [12]. Despite the noteworthy efficiency, poor long-term stability becomes a bottleneck toward the practical commercialization of PSCs. As two-dimensional perovskite (2D PSK) has a strong resistance to moisture and heat compared with conventional 3D PSK [76, 77], research interest in 2D PSK-based PSC has been increasing ever since Smith *et al.* firstly reported 2D PSK as the light absorber for PSC in 2014 [78].

The Ruddlesden-Popper (RP) perovskite is one type of the typical structure which can emerge in 2D perovskite material. It is commonly formed by splitting along lattice direction $\langle 100 \rangle$ from 3D perovskite (**Figure 16a**) [79]. Another representative type of 2D PSK is the Dion-Jacobson (DJ) perovskite. The main difference between the two is the relative stacking of the layers, so the DJ perovskite is suitable for a wide infrared range (**Figure 16b**) [80]. DJ perovskite has high crystallinity, while the ability to control the smaller bandgap and thickness of the RP type makes it more commonly used in solar cells.

The 2D PSK is generally described with formula $(A'_m A_{n-1} B_n X_{3n+1})$, in

which A' cation can be bound to the inorganic sheet ($A_{n-1}B_nX_{3n+1}$) by forming a double or single layer with divalent or monovalent ($m = 1$ or 2) binding. Also, A' cations, which are relatively bulky organic spacers such as n-butylammonium (BA), phenylethyl ammonium (PEA), cyclopropylammonium (CA), benzylammonium (BEA), and ammonium valeric acid (AVA), are intrinsically hydrophobic and confer the stability on 2D PSK [81]. 2D PSK has a layered structure of 2D and 3D structures mixed in a periodic pattern and 'n' represents the distance between 2D materials. in the case of $n = 1$, it represents a pure 2D PSK in which an inorganic sheet is present between each 2D layer and when $1 < n \leq 5$, it is known as a 2D quasi-PSK, and pure 3D PSK has infinity n; It has only 3D perovskite layers without 2D perovskite layer (**Figure 16c**) [82]. Moreover, the hydrophobic nature of 2D PSKs, exciton characteristics are naturally obtained based on the multiple-quantum-well structure, created by the layered-structure, which leads to more insulating behaviors [83]. Therefore, 2D PSKs have tunable bandgaps and stability through manipulation of its 'n' value. The lower 'n' value, the higher bandgap and stability of perovskite (**Figure 17**) [84, 85]. Thanks to these features, the introduction of 2D PSK to 3D PSK lattice has been proposed as one of the powerful engineering methods for improving PSC

stability.

However, the direct mixing of organic cation spacers limits device efficiency, as the 2D PSK segments, which are arbitrarily incorporated, interfere with charge transport from domain to domain due to their insulating properties (**Figure 18**) [81, 86]. To address this dilemma, several recent studies have demonstrated a strategy to fabricate a 2D/3D hybrid perovskite for a highly efficient and stable device (**Figure 19**) [87-93]. The bulky organic cations are deposited on the preformed 3D PSK surface to induce in situ growth of the 2D PSK layer. This methodology reduces the number of surface trap states and suppresses charge recombination by the optimized band alignment of the 2D/3D hybrid perovskite structure, improving stability as well as PV performance of PSC.

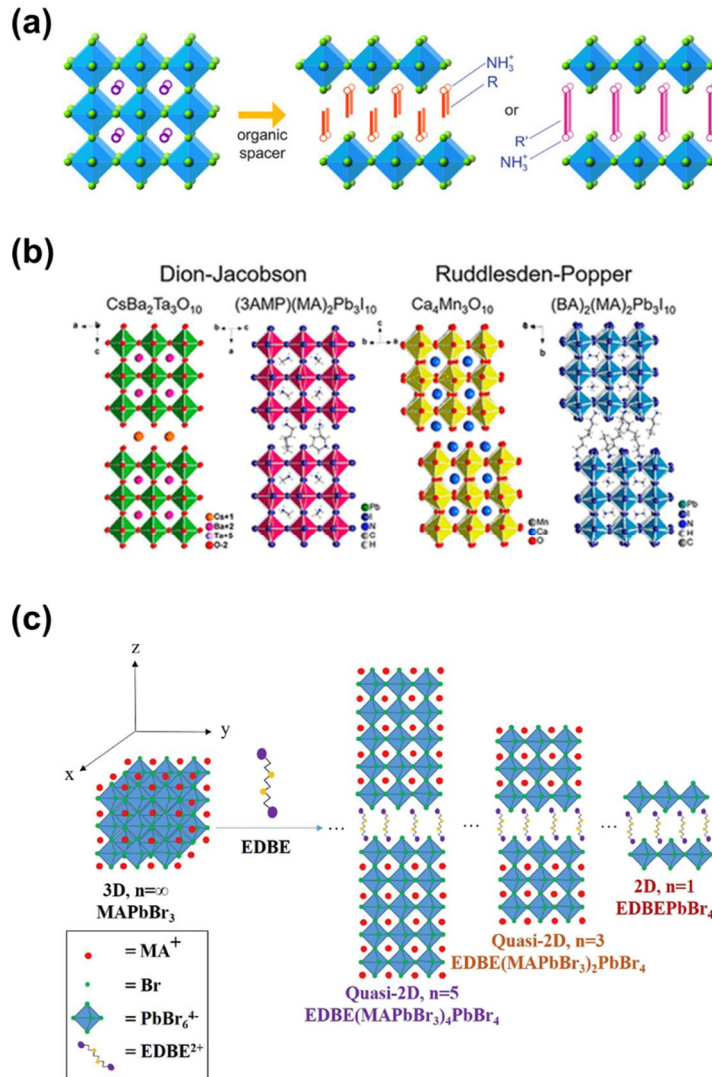


Figure 16. (a) Crystal structures of 2D PSK from 3D PSK through the insertion of organic spacer in $\langle 100 \rangle$ lattice direction [79]. (b) Comparison between Dion-Jacobson (DJ) type and Ruddlesden-Popper (RP) perovskite [80]. (c) Illustration of quasi-2D PSK formed by a number of n [82].

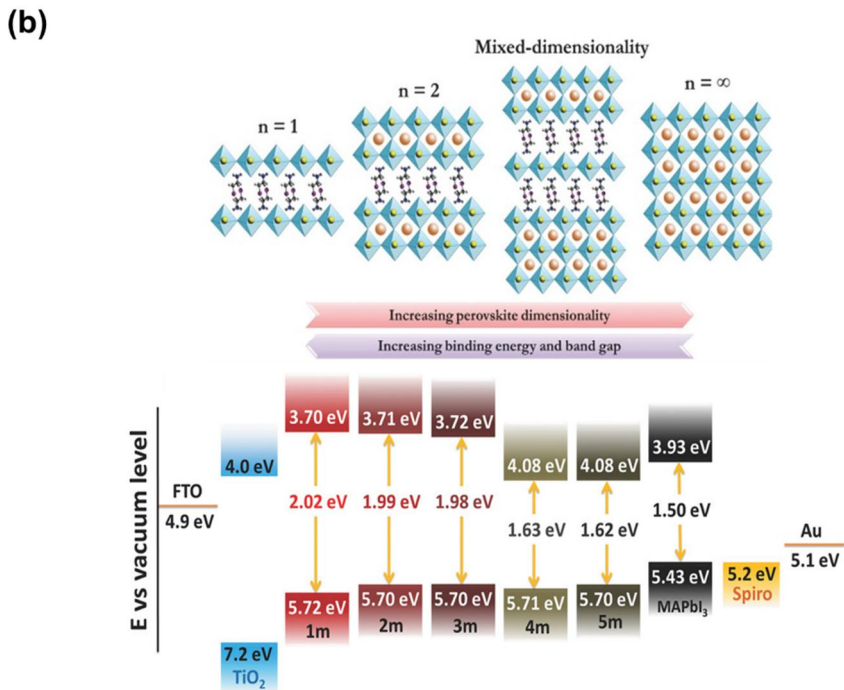
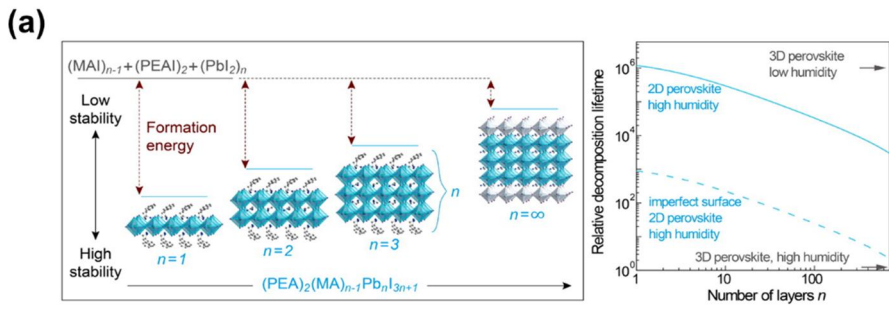


Figure 17. (a) Moisture stability and (b) bandgap control according to n -value control of 2D PSK [84, 85].

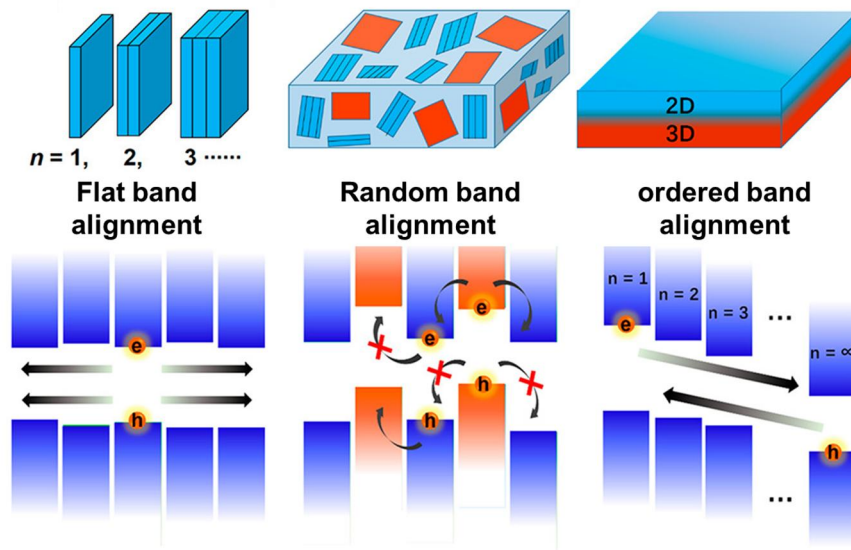


Figure 18. Schematic of energy band alignment according to types of 2D PSK (large- n 2D PSK, randomly mixed 2D/3D PSK, and ordered 2D/3D hybrid PSK, sequentially) [81].

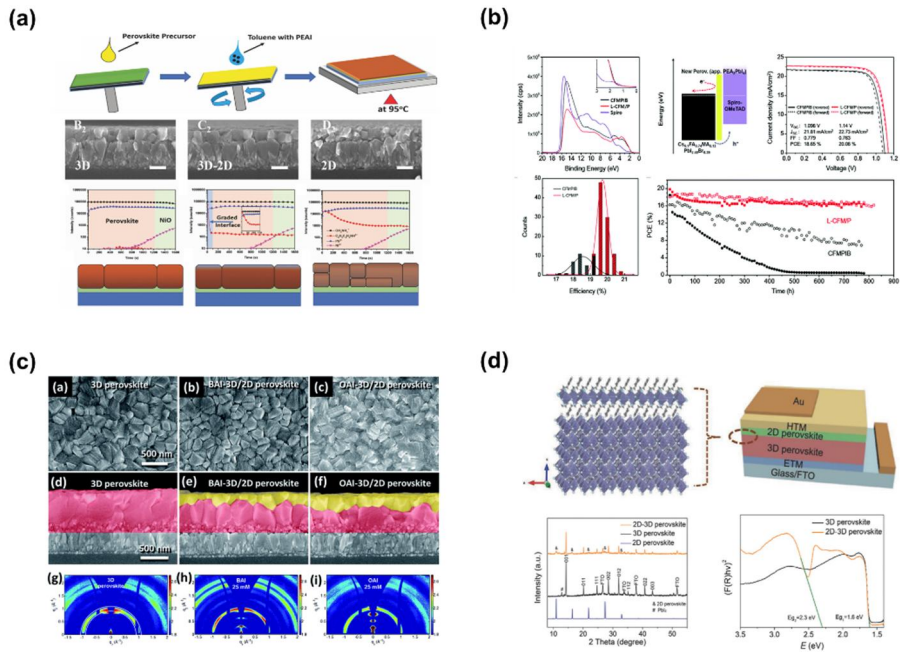


Figure 19. Various interface engineering for highly efficient and stable PSC *via* the introduction of 2D/3D hybrid perovskite; (a) 2D ligand treatment during the anti-solvent process and change the crystallinity according to compositional ratio [88]. (b) Improved efficiency and long-term stability by introducing the PEAI-based interface layer [89]. (c) Change of 2D PSK crystallinity according to the alkyl chain length of 2D PSK [90]. (d) Characterization of 2D PSK as a capping layer between HTM and 3D PSK [91].

1.1.4.1.2. Interfacial passivated-PSCs based on excess PbI_2

Indeed, regardless of the external environmental stress on the perovskite, the perovskite surface and grain boundaries (GBs) have several potential defects, such as cationic, anionic vacancies and Pb^+ anti-site of substitution defects, as described in **Figure 20a** [94]. These kinds of defects could act as undesired recombination sites at the interface between HTL or ETL and perovskite, which adversely affects the voltage and charge transfer process at the device level.

To overcome the surface recombination, a custom passivation scheme must be implemented at the interface [95]. **Figure 20b** illustrates the various passivation mechanisms on perovskite. The first is chemical surface passivation, which reduces the density of defects and reduces the rate of recombination. Secondly, the use of field-effect passivation repels free charges (electrons or holes) at the interface, reducing the likelihood of trapping charges at defect sites. Finally, in the most ideal case, combining bulk and surface passivation without causing resistance loss can provide the best performance for the PSC [94].

Recently, lead (II) iodide (PbI_2) has been known to passivate the interface layer across the entire interface of the perovskite. In this regard, it has been argued that an excess PbI_2 controlled in the perovskite layer

improves device performance by forming a shell around individual perovskite crystals in the film (**Figure 21a**) [96]. According to the excess PbI_2 , it acts as a self-inducing passivated layer at the interface between the GB and charge transport layer, and improves the efficiency of the device through the effect of suppressing charge recombination. On the other hand, a deficient PbI_2 may cause ion migration or hysteresis due to insufficient passivation of GB, so an appropriate excess of PbI_2 helped improve device efficiency (**Figure 21b**) [97, 98]. However, due to the large bandgap of PbI_2 , excess PbI_2 can easily create a potential barrier in the charge extraction layer, and PbI_2 remaining in GB may act as a factor promoting deterioration of perovskite (**Figure 22**) [99]. Therefore, controlling the optimized excess PbI_2 is important to improve device performance and stability.

To this end, additional organic ligand treatment studies (e.g. self-healing interfacial layer growth through reaction with residual PbI_2 of MAI [100], methylammonium bromide (MABr) [101], and formamidinium iodide (FAI) post-treatment [102], perovskite interfacial layer formation with different composition through formamidinium bromide (FABr) treatment [103], and hierarchical 2D/3D PSK based on PEAI treatment [104]) were proposed to form an additional interface

passivation layer based on excess PbI_2 as an ideal control method. The growth of the excess PbI_2 -based perovskite interfacial layer induced performance and efficiency improvement by suppressing surface charge recombination of surface defects and trap sites at the perovskite (**Figure 23, 24**).

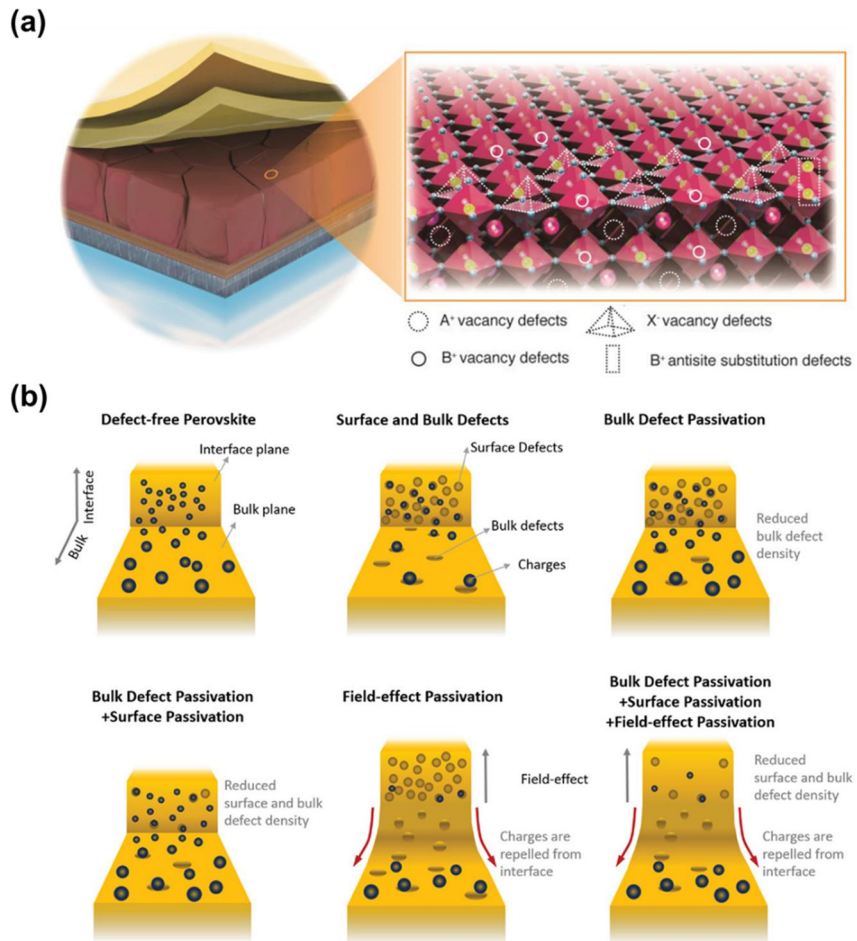


Figure 20. (a) Types of defect sites that might exist on the perovskite film, and (b) schematic illustration of passivation mechanisms that can occur at the interface on perovskite [94].

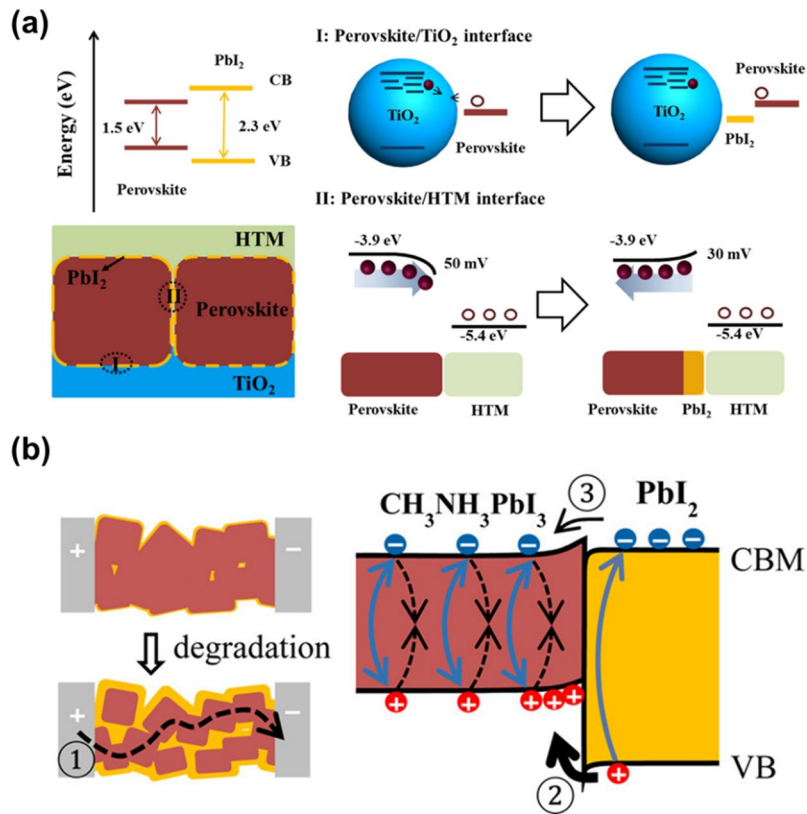


Figure 21. (a) A mechanism for self-induced passivation of PbI_2 in perovskite Film [96]. (b) Model of the $\text{CH}_3\text{NH}_3\text{PbI}_3/\text{PbI}_2$ interface; (1) restricted current flow against PbI_2 , (2) hole injection from PbI_2 to $\text{CH}_3\text{NH}_3\text{PbI}_3$, and (3) electron injection due to band bending with generated charges and heat excitation [99].

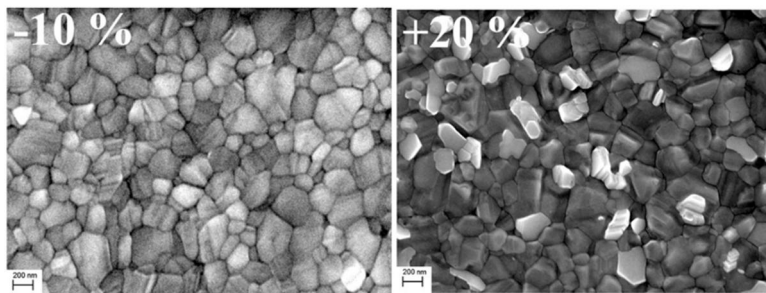
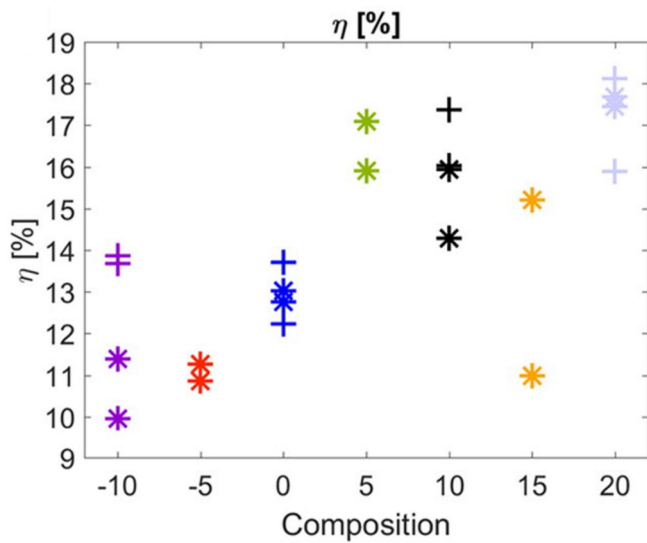


Figure 22. Variation of PSC efficiency according to stoichiometric control and surface SEM image of deficient and excess PbI_2 samples [97].

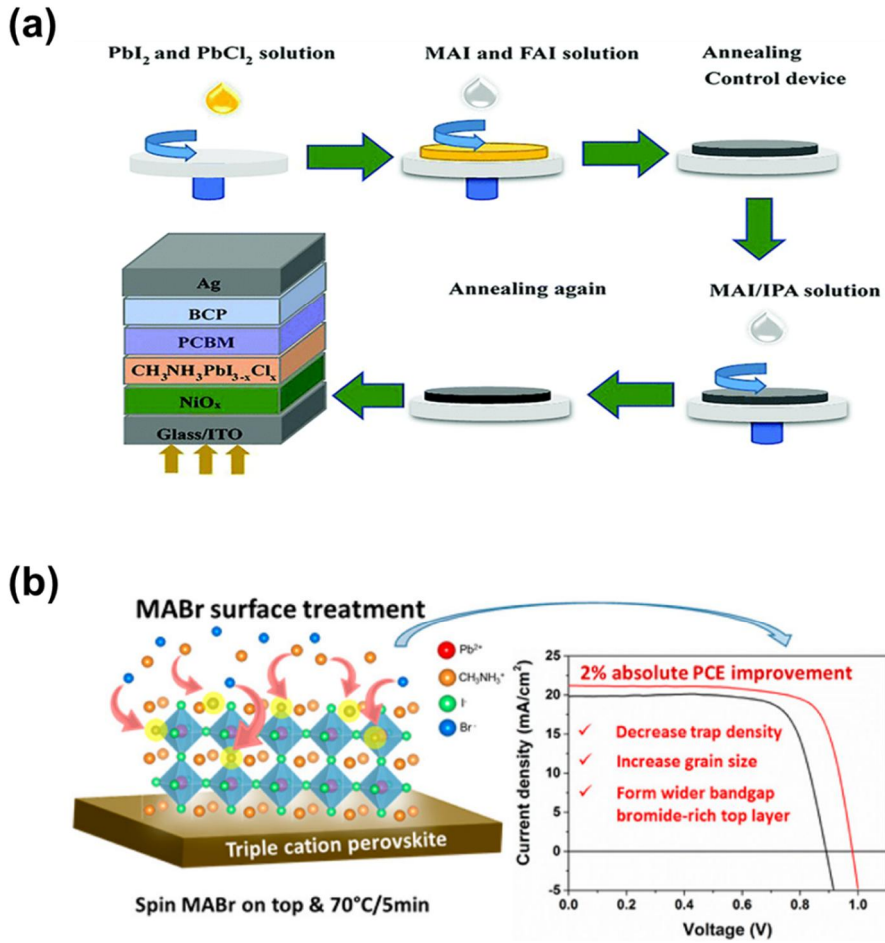


Figure 23. Additional ligand treatment-based interfacial perovskite layer reacted with excess PbI₂; (a) MAI treatment [100], and (b) MABr treatment [101].

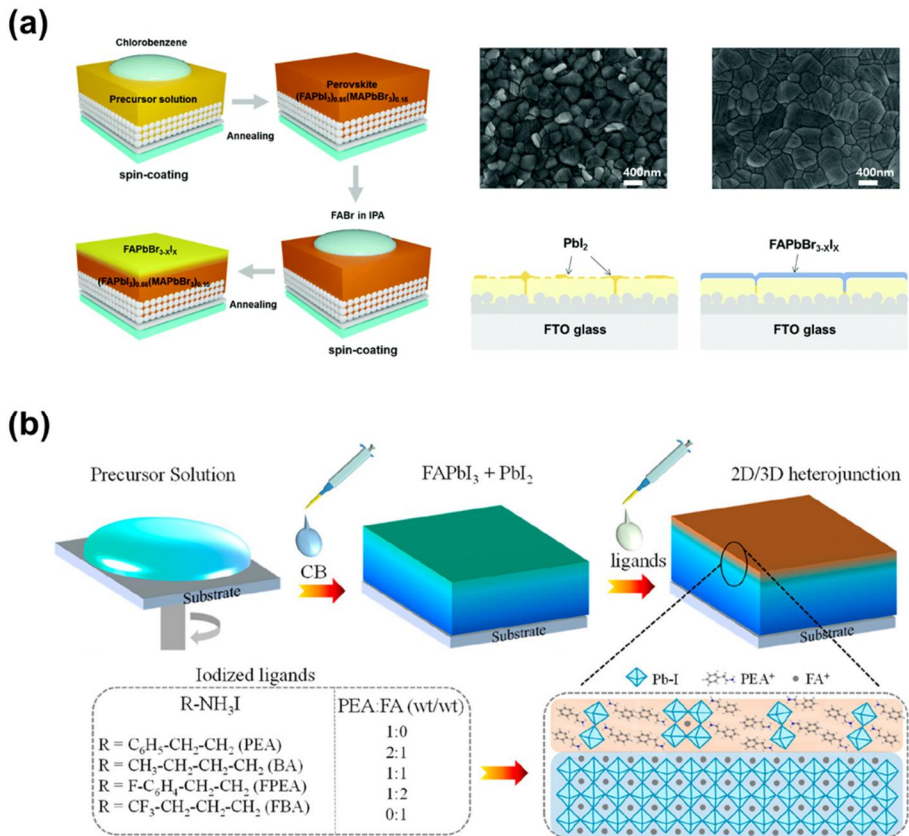


Figure 24. Different compositions of perovskite interfacial layer formation *via* organic ligand reacted with excess PbI₂; (a) FAPbBr₃ treatment [103], and (b) assorted 2D ligands treatment [104].

1.1.4.2. Interface engineering based on plasma process

Plasma is an ionized gas energy state with electrical conductivity, and surface treatment can improve adhesion or heterogeneity between materials. Generally, it refers to a state in which various chemical reactions occur due to the coexistence of ionized ions, electrons, neutral particles, and active particles (radicals) **(Figure 25a)** [105]. Plasma treatment can be performed in an exhausted enclosure or a chamber. Before the energy in the form of power is supplied, the air is pumped and gas flows at low pressure. In addition, plasma can be treated even at atmospheric pressure, but it is not easy to control process uniformity and plasma source, there are limitations of process gases used [106]. Even so, plasma treatment is actually a low-temperature process, which is a good way to modify the surface of heat-sensitive materials **(Figure 25b)** [107-109].

Plasma changes the general physicochemical pathway and offers new materials and new surface treatment methods. Plasma surface treatment shows the following effects; (1) Surface cleaning minimizes contamination of the surface by removing natural and technical oils from the nanoscale, (2) functionalization controls the wettability of the surface, (3) surface etching forms specific nanoscale patterns to increase the

surface area of material, and (4) surface coating within a short time introduces a specific material element layer (**Figure 26**). At this time, the energy level can be adjusted when a specific element or material is introduced through gas control, which affects performance improvement by controlling the charge transfer of the device [110, 111].

In particular, carbon-based materials used as charge transfer materials such as electrodes, interface layers, and photocatalytic materials, work function (WF) and surficial contact property control by introducing specific elements have been performed as one of the important research topics [112]. In this element introduction process, the introduction of heterogeneous elements on carbon-based material using the plasma process has attracted attention based on the simplicity of the process [113-117].

Through this simple plasma treatment method, studies have been conducted to improve the performance and stability of PSC by inducing energy level and surface contact control through oxygen plasma treatment, but studies on the introduction of various heterogeneous elements are still insufficient (**Figure 27**) [118, 119].

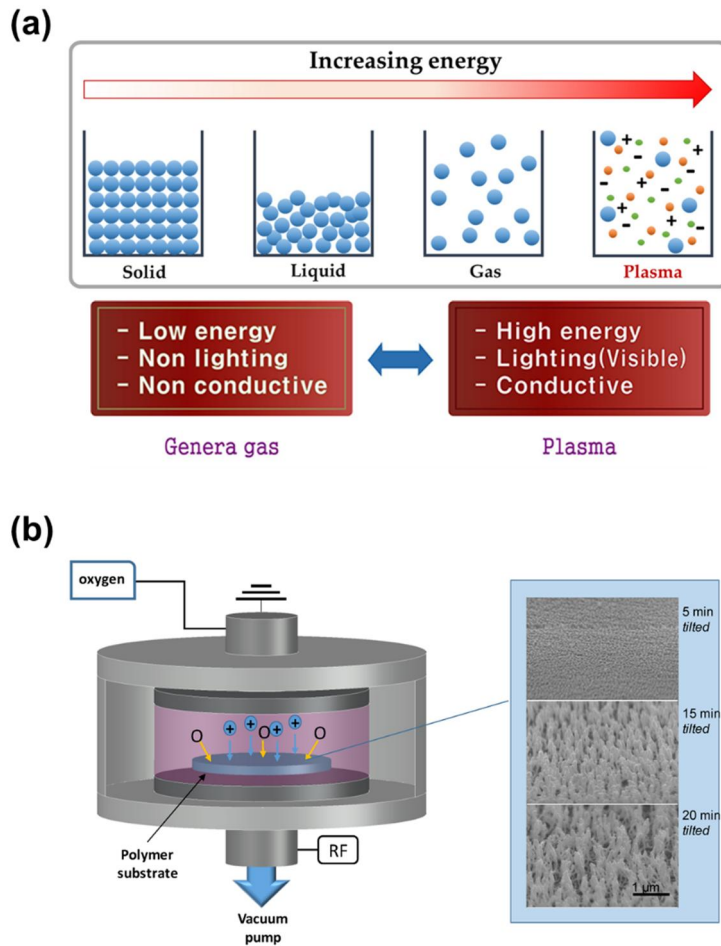


Figure 25. (a) Schematic images of plasma generation by adding energy to the material, the gas of electrons and ions and properties of plasma, and (b) illustration of typical plasma equipment for surficial texturing-process [105, 108].

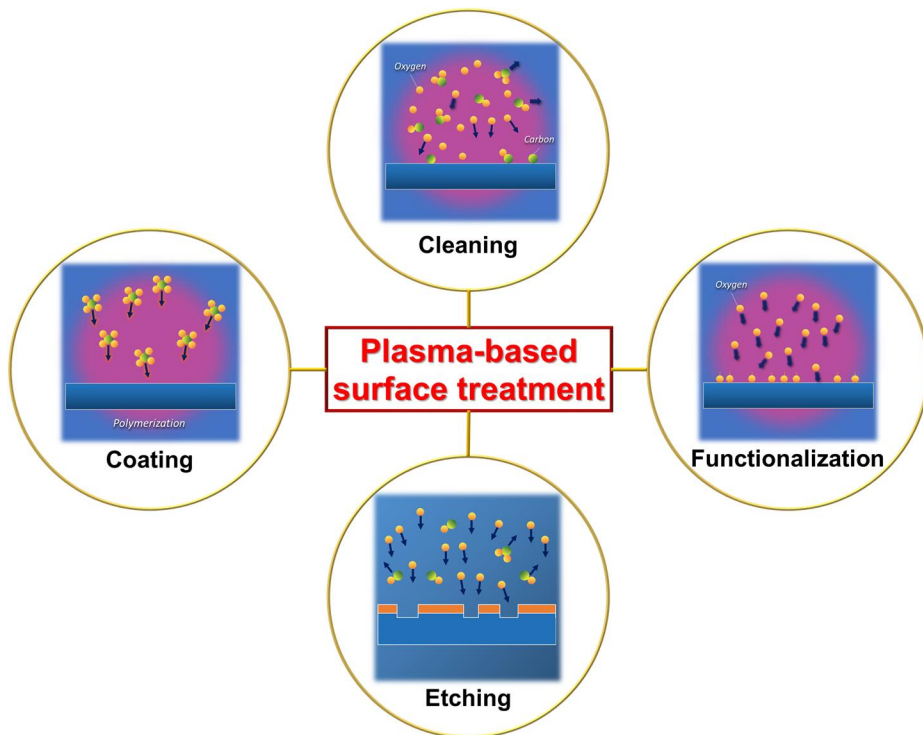


Figure 26. Schematic diagram indicating the general purpose of the four types of plasma-based surface treatment.

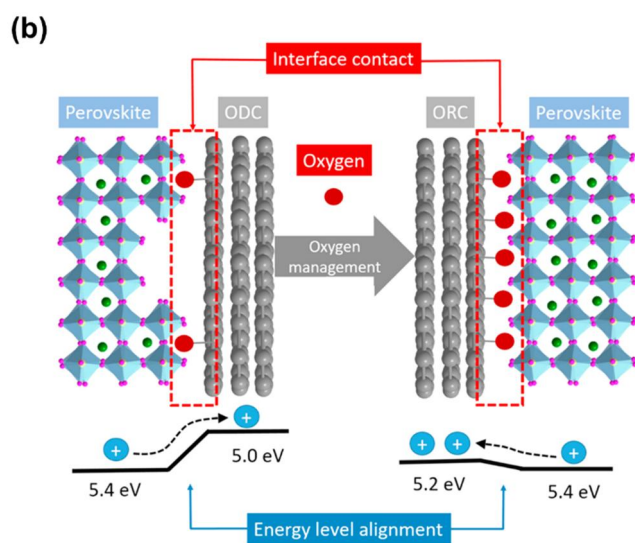
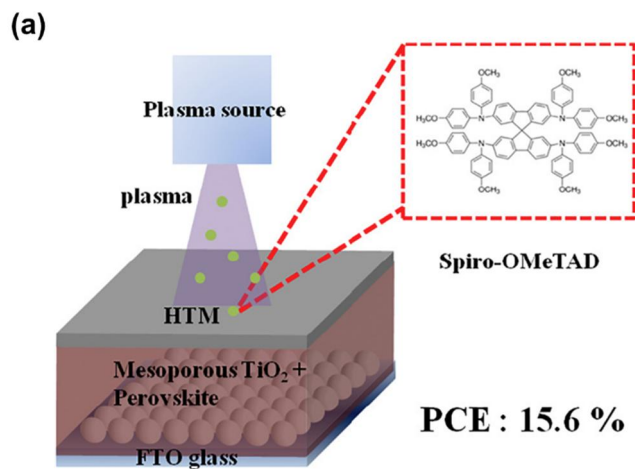


Figure 27. Diverse plasma-treatment for high efficient PSC; (a) Adjusted energy level of spiro-OMeTAD through the oxygen plasma [118]. (b) Printable C-PSC with WF controlled carbon electrode *via* oxygen plasma [119].

1.2. Objectives and Outlines

1.2.1. Objectives

The aim of this dissertation is to explain strategies for achieving high-performance, long-term stabilization of hole conductor-free carbon electrode-based perovskite solar cells as well as to propose interfacial engineering methods based on various process and material. In detail, a highly stable and efficient carbon electrode-based perovskite solar cell based on a 2D/3D hybrid perovskite was prepared by introducing the interfacial 2D perovskite layer *via* post-treatment of a bulk organic ligand solution. Subsequently, in the interfacial process, the introduction of nano-sized inorganic PbI_2 that can be dispersed in a non-polar solvent and the sequential organic ligand solution treatment form a hierarchical perovskite with improved interface contact between the carbon electrode and perovskite. Furthermore, in terms of process, fluorine-based plasma treatment not only improves photovoltaic performance through interfacial energy level control but also maximizes moisture resistance. This study provides an interface engineering perspective and distinctive approaches to carbon electrode-based perovskite solar cells to improve production efficiency and long-term stability that are critical to the commercialization of perovskite solar cells.

1.2.2. Outlines

This dissertation focused on devising a method to improve the efficiency and stability of carbon electrode-based perovskite solar cells (C-PSCs) by introducing the interfacial layer based on various processes and materials and adjusting the interfacial energy level.

This dissertation involves the following subtopics:

I. Interface engineering of C-PSC based on 2D perovskite (2D PSK) layer through bulk ligand solution treatment

I-1. Fabrication of C-PSCs with 2D PSK interfacial layer *via* phenylethylammonium iodide (PEAI) treatment

I-2. Evaluation of photovoltaic performance

I-3. Analysis of interfacial properties between carbon and perovskite

I-4. Device stability test

II. Interface engineering of C-PSCs based on secondary growth of MAPbI₃ interfacial layer *via* colloidal PbI₂ treatment

II-1. Preparation of colloidal PbI₂ capped with organic acids

II-2. Fabrication of C-PSCs with secondary grown MAPbI₃ interfacial layer *via* the sequential treatment of colloidal PbI₂ and MAI

II-3. Evaluation of photovoltaic performance

II-4. Analysis of interface properties between carbon and perovskite

II-5. Device stability test

III. Interface engineering of C-PSCs based on energy level adjustment of carbon layer through fluorine plasma treatment

III-1. Fabrication of C-PSCs with gradient fluorine-doped carbon electrode *via* fluorine gas-based vacuum plasma treatment

III-2. Evaluation of photovoltaic performance

III-3. Analysis of interface properties between carbon and perovskite

III-4. Device stability test

2. Experimental Details

2.1. Interface engineering of C-PSCs based on 2D PSK interfacial layer

2.1.1. Fabrication of C-PSCs with 2D PSK interfacial layer

FTO coated substrates with a sheet resistance of $7 \Omega \text{ sq}^{-1}$, Carbon paste (FTU-16, $\leq 20 \Omega \text{ sq}^{-1}$) and methylamine (40% in methanol) were purchased from Wooyang GMS, Asahi Chemical Research Laboratory and Junsei Chemical Co., Ltd., respectively. Cesium iodide (CsI, 99.999% trace metals basis), Lithium bis(trifluoromethanesulfonyl)imide (Li-TFSI $\geq 99\%$), titanium (IV) isopropoxide ($\geq 97\%$), hydroiodic acid (HCl, 57 wt% in H₂O, $\geq 99.99\%$), lead bromide (PbBr₂, $\geq 98\%$), acetonitrile (anhydrous, 99.8%), *N,N*-dimethylformamide (DMF, anhydrous, 99.8%), dimethyl sulfoxide (DMSO, anhydrous, 99.9%) were purchased from Sigma-Aldrich. Lead iodide (PbI₂, 99.9985%, metals basis), carbon black (Super-P conductive) and chlorobenzene (99%) were obtained from Alfa aesar. Formamidinium iodide (FAI, $\geq 98\%$), TiO₂ paste (30 NR-D), methylammonium bromide (MABr, $\geq 98\%$) and phenylethylammonium iodide (PEAI) were purchased from GreatCell Solar. Methylammonium iodide (MAI) was synthesized through a

generally well-known method, reaction of methylamine with hydroiodic acid [120]. All chemical reagents and solvents mentioned above were used without further purification. FTO glass substrates were etched with 2M HCl and Zn powder to form the electrode patterns. The patterned FTO substrates were ultrasonically cleaned in deionized (DI) water, acetone and isopropanol (IPA) for 30 min, sequentially. To deposit a dense TiO₂ compact layer as a hole-blocking layer, a mildly acidic solution of titanium (IV) isopropoxide in ethanol (EtOH) was spin-coated onto the substrate at 3000 rpm for 30 s and heated at 150 °C for 10 min in ambient air. The compact TiO₂ layer coated substrate was then sintered at 500 °C for 60 min in the muffle furnace. After cooling to the room temperature, a mesoporous TiO₂; which was prepared by diluting TiO₂ paste in ethanol (1: 3.5 at a mass ratio) was spin coated on the compact TiO₂ layer at 3000 rpm for 30 s. The substrate was annealed at 150 °C for 10 min and sintered at 500 °C for 60 min. To obtain Li-doped TiO₂, Li-TFSI solution (15 mg mL⁻¹ in acetonitrile) was treated on the mesoporous TiO₂ layer by spin coating at 3000 rpm for 30 s. The treated substrate was heated at 150 °C for 10 min, followed by sintering at 500 °C for 30 min. As a role of the light-absorbing layer, the cesium-containing triple cation-mixed halide perovskite

($\text{Cs}_{0.05}\text{MA}_{0.16}\text{FA}_{0.79}\text{Pb}(\text{I}_{0.84}\text{Br}_{0.16})_3$) was deposited as a previously reported method [121]. FAI (1 M), PbI_2 (1.1 M), MABr (0.2 M) and PbBr_2 (0.2 M) were dissolved in a mixed solvent of DMF and DMSO (4:1 v/v), and the mixed perovskite precursor solution was stirred at 50 °C for 1 h. Then 40 μl of CsI, pre-dissolved in DMSO as a stock solution (1.5 M) was added to the mixed solution and stirred for an additional 1h. The mixed solution was filtered with a 0.45 μm polytetrafluoroethylene (PTFE) syringe filter before spin-coating. The perovskite precursor solution was cast onto the substrate and spin-coated in two steps at 1000 and 5000 rpm for 10 and 23 s, respectively. During the second step, 180 μl of chlorobenzene was dropped on the spinning substrate at 10 s prior to the completion of the process. After the entire spin-coating process, the substrate was immediately placed on a 100 C hot plate and annealed for 45 min to crystallize the 3D perovskite. To deposit a carbon electrode, the carbon paste mixed with carbon black (2 wt%) and chlorobenzene was screen-printed on the 3D perovskite layer and cured at 100 °C for 10 min. This depositing procedure was conducted three times successively. To introduce a 2D perovskite layer between the 3D perovskite and carbon electrode, 200 μl of PEAI solution (10 mg mL^{-1} in IPA) was poured onto the carbon electrode-printed substrate. After

30 s, the substrate was spin-coated at 3000 rpm for 30 s and then annealed at 100 °C for 10 min. All fabrication processes were conducted under the controlled ambient condition with 25 °C and 30% relative humidity.

2.1.2. Characterization of C-PSCs with 2D PSK interfacial layer

Field-emission scanning electron microscopy (FE-SEM) images of surface morphology and cross-section of the device and field-emission electron probe micro-analyzer (FE-EPMA) spectra were obtained from JSM-6701F (JEOL Ltd) and JXA-8530F (JEOL Ltd), respectively, which are installed at the National Center for Inter-University Research Facilities (NCIRF) at Seoul National University. X-ray diffraction (XRD) patterns of the perovskite films were measured using SmartLab (Rigaku). Steady-state photoluminescence (SSPL) spectra were measured using an LS-55 fluorescence spectrometer (Perkin-Elmer). Time-resolved photoluminescence (TRPL) decay profiles were measured under exposure to a 405 nm pulsed laser (Pico-Quant). Current density–voltage (J – V) characteristics of the PSCs were measured using an I–V tracer (MP-160; Eko Instruments) under standard AM 1.5 G (100 mW cm⁻²) illumination from a 500 W xenon lamp, calibrated with a KG5-filtered Si reference cell (K801; McScience Inc.). The active area of the fabricated device was 0.132 cm². The incident photon-to-current

efficiency (IPCE) spectra were characterized using a K3100 Solar Cell IPCE System (McScience Inc.) without bias light. Stabilized power output, open-circuit voltage (V_{oc}) and electrochemical impedance spectroscopy (EIS) spectra of the PSCs and $I-V$ characteristics of the carbon electrode were measured using the Zive Lab equipment (WonA Tech). The active area for EIS measurements was 0.132 cm^2 and the EIS spectra were fitted by an equivalent electrical circuit using the Z-view analyst software (ZMAN).

2.2. Interface engineering of C-PSCs based on secondary growth

MAPbI₃ interfacial layer

2.2.1. Preparation of Colloidal PbI₂ Solution

Colloidal PbI₂ solution was prepared as follows. PbI₂ and organic acids (butyric acid, hexanoic acid and octanoic acid ($\geq 99\%$) were purchased from Sigma-Aldrich, respectively) were mixed in chlorobenzene with a molar ratio (1:2), and then sonicated at room temperature for 1 h in a water bath to form a colloid structure of PbI₂ capped with organic acids. A pale yellow solution was formed by colloidal PbI₂ particles, which were well dispersed in chlorobenzene.

2.2.2. Fabrication of C-PSCs with secondary growth MAPbI₃ interfacial layer

The patterning of FTO glass substrates was conducted by chemical etching of FTO with 2 M aqueous hydrochloric acid and Zn powder. The patterned FTO glass substrate was ultrasonically rinsed in deionized water, acetone and 2-propanol for 60 min, respectively. To develop a compact TiO₂ (c-TiO₂) layer as a hole blocking layer, prepared titanium (IV) isopropoxide solution (0.2 M) diluted in a mixed solution of EtOH:HCl (4:1 v/v) was spin-coated on the cleaned FTO substrate at

3000 rpm for 30 s, followed by thermal annealing at 100 °C for 10 min in ambient air and 500 °C for 45 min in a muffle furnace, sequentially. After cooling to room temperature, a diluted solution of TiO₂ paste in the anhydrous ethanol (0.2 wt%) was deposited onto the FTO/c-TiO₂ substrate to form a mesoporous TiO₂ (meso-TiO₂) layer by the spin-coating process at 3000 rpm for 60 s. After pre-heating at 150 °C for 10 min, the meso-TiO₂ film was gradually heated to 500 °C in the muffle furnace, and then the film was sintered at the same temperature to remove organic components. To accomplish Li-doped meso-TiO₂ layer, Li-TFSI solution (15 mg mL⁻¹ in acetonitrile) was treated on the meso-TiO₂ layer by spin coating at 3000 rpm for 40 s including 10 s of loading time. Cs_{0.05}MA_{0.16}FA_{0.79}Pb(I_{0.84}Br_{0.16})₃ precursor solution was prepared by mixing the FAI (1 M), PbI₂ (1.1 M), PbBr₂ (0.2 M), MABr (0.2 M), and CsI (0.06 M) in a mixed solvent of DMF:DMSO (at a volume ratio 4:1). The prepared solution was stirred at 60 °C for 2 h and filtered with a 0.45 μm PTFE syringe filter before use. The aged perovskite precursor solution was dropped on the FTO/c-TiO₂/Li-doped meso-TiO₂ substrate and directly spin-coated in a two steps process at 1000 and 4000 rpm for 10 and 23 s, respectively. During the second step, 180 μl of chlorobenzene was poured onto the spinning substrate 10 s prior to the

end of the process. After the entire coating process was completed, the substrate was annealed at 100 °C for 20 min under ambient air (30% RH, 25 °C) to crystallize the perovskite layer. To introduce the carbon electrode, a graphite-based carbon paste blended with carbon black (2 wt%) was screen-printed on the perovskite film, followed by drying at 70 °C for 30 min. The screen-printing and drying process was repeated three times to prepare an optimized thickness carbon-paste electrode, successively. To fabricate an interfacial MAPbI₃ layer based on a colloidal PbI₂ solution, the colloidal solution was dropped on the fabricated PSC containing a printed-carbon electrode and waited for sufficient Infiltration of the PbI₂. After wetting for 30 s, the substrate was spin-coated at 3000 rpm for 30 s and dried at 120 °C for 5 min. Secondary growth of MAPbI₃ film was fabricated by spin-coating the MAI solution (20 mg mL⁻¹) onto the PbI₂-treated device at 3000 rpm for 45 s, including the permeation time through the carbon electrode, and then annealed at 100 °C for 10 min in air.

2.2.3. Characterization of C-PSCs with secondary growth MAPbI₃ interfacial layer

FE-SEM image of the surface and cross-sectional morphology of the

device and FE-EPMA elemental mapping image were obtained from JSM-6701F (JEOL Ltd.) and JXA-8530F (JEOL Ltd.), respectively, which are installed at the National Center for Inter-University Research Facilities (NCIRF) at Seoul National University. Both the surface of topography and electrical properties were simultaneously investigated using PinPoint™ scan mode of the NX-10 atomic force microscopy (AFM) (Park system) which is installed at the Research Institute of Advanced Materials (RIAM) at Seoul National University. The nitrogen adsorption–desorption isotherms were analyzed using an ASAP 2010 (Micrometrics) equipment. In detail, pore size distribution and surface area were measured by Brunauer–Emmett–Teller (BET) and Barrett–Joyner–Halenda (BJH) methods. Transmission electron microscopy (TEM) images were obtained from a JEM-2100 (JEOL Ltd.), which are installed at the NCIRF at Seoul National University. The HR-TEM image and selected area electron diffraction (SAED) pattern were acquired using a JEM-2100F (JEOL Ltd.), which are installed at the RIAM at Seoul National University. XRD measurements were performed on a SmartLab X-ray Diffractometer (Rigaku) using Cu K α radiation ($\lambda = 1.5406 \text{ \AA}$) at 40 kV and 300 mA (12 W). Fourier-transform infrared (FT-IR) spectra of the perovskite surfaces were measured by a Spotlight 200i

(PerkinElmer). Raman spectra were obtained by DXR2xi (Thermo Scientific™). The Ultraviolet photoelectron spectroscopy (UPS) analysis was conducted using an AXIS Ultra DLD (Kratos Analytical) with an excitation source (He I, 21.2eV), which is installed at the Korea Basic Science Institute (KBIS). UV–Vis absorbance spectra were measured by a V-770 UV-Vis spectrophotometer (JASCO). All of the photo-luminescent experiments were performed using a home-built microscope. SSPL and TRPL spectra carried out using a time-correlated single-photon-counting (TCSPC) board (SPC-150, Becker & Hickl GmbH) under exposure to 420 nm and 520 nm pulse laser (Picoquant), respectively. J – V curves were investigated using an MP-160 I–V tracer (Eko instruments) under standard AM 1.5 G irradiation with a power density of 100 mW cm⁻² (XIL Model 05A50KS source units) from a xenon lamp (530 W), calibrated with a KG-5 filtered Si Ref. Cell (K-801; McScience Inc). IPCE spectra were measured by QEX7 Solar Cell Spectral Response EQE/IPCE Measurement System (PV Measurements) under a short-circuit current. EIS spectra characteristics (Nyquist plot) and stabilized power output (SPO) of devices were conducted using Zive Lab equipment (WonATech). The measured EIS spectra were fitted to equivalent electrical circuits using Z-view analyst software (ZMAN). J –

V plots and trap-filled limit voltage of hole-only devices was measured on the planar specimen (FTO / PEDOT:PSS (PH 1000) / triple cation-mixed halide perovskite / (MAPbI₃) / carbon) by Zahner Elektrik IM6 analyzer (Zahner Elektrik GmbH & Co). Mott-Gurney law equation was employed to calculate the hole mobility. The equation is below:

$$J = \frac{9}{8} \mu \epsilon_0 \epsilon_r \frac{V^2}{L^3}$$

μ : hole mobility

ϵ_0 : free space permittivity

ϵ_r : dielectric constant

L: film thickness

The direct current conductivity (σ_0) of the carbon electrode was calculated by extracting the slopes from I - V curves with an equation, $I = \sigma_0 A d^{-1} V$ as a previous report [122].

2.3. Interface engineering of C-PSCs based on energy level adjustment *via* F-plasma treatment

2.3.1. Fabrication of C-PSCs with F-doped carbon layer

FTO glass substrates were etched with 2.0 M aqueous HCl and Zn powder to form the patterned electrode. The patterned FTO substrates were ultrasonically cleaned in deionized water, acetone and IPA for 60 min, sequentially. To deposit the c-TiO₂ layer, a solution of titanium (IV) isopropoxide (1 mL) in 15 mL mixed solution of EtOH:HCl (at a volumetric ratio 4:1) was spin-coated onto the substrate at 3000 rpm for 30 s, followed by preheating at 120 °C for 10 min in ambient air. The preheated substrate was sintered at 500 °C for 60 min in a muffle furnace and then cooled at room temperature. A solution of TiO₂ paste, which was diluted in ethanol (1:3.5 at molar ratio) to form the meso-TiO₂ layer, was spin-coated on the c-TiO₂ layer at 3000 rpm for 30 s. The substrate was annealed at 150 °C for 10 min and then sintered at 500 °C for 60 min. To prepare Li-doped TiO₂, Li-TFSI (15 mg mL⁻¹ in acetonitrile) was treated on the meso-TiO₂ layer by spin-coating at 3000 rpm for 30 s. The treated substrate was preheated at 150 °C for 10 min, followed by the sintering process at 500 °C for 30 min. Cs_{0.05}MA_{0.16}FA_{0.79}Pb(I_{0.84}Br_{0.16})₃ precursor solution was prepared by mixing the PbI₂ (1.1 M), PbBr₂ (0.2

M), FAI (1 M), MABr (0.2 M), and CsI (0.06 M) in a mixed solvent of DMF:DMSO (at a volumetric ratio 4:1). The mixed solution was stirred at 60 °C for 2 h and filtered with a 0.45 µm PTFE syringe filter before spin coating. The prepared perovskite precursor solution spread onto the substrate and spin-coated by two steps process at 1000 and 4000 rpm for 10 and 23 s, respectively. After entering the second step, 180 µl of chlorobenzene was poured onto the substrate 10 s before the end of the process. After the entire spin coating process is completed, the substrate is placed on a 100 °C hot plate and annealed for 30 min to crystallize the perovskite layer. To form the carbon electrode, a carbon paste mixed with carbon black (2 wt%) was screen printed on the perovskite layer, and the printed carbon paste was dried at 80 °C for 10 min. This carbon-printing process was repeated three times, successively. To introduce fluorine atoms into the carbon electrode, a fluorine vacuum plasma treatment was performed on the substrate on which the carbon electrode was printed. In the plasma system (Korea vacuum Co.), which was used in experiments, an ICP (inductively coupled plasma) source was formed with RF power in a vacuum vessel. The fluorine source, C₄F₈ gas, was flowed at a rate of 5 sccm under 25 Pa and treated with 100 W power for 20 min. The fluorine source injection conditions were optimized based

on previous reports [123]. With the exception of the plasma treatment, all manufacturing processes were carried out under controlled atmospheric conditions with a relative humidity of 25 °C and 40%.

2.3.2. Characterization of C-PSCs with F-doped carbon layer

The FE-EPMA elemental mapping image and cross-sectional FE-SEM image were measured by JXA-8530F (JEOL) which is installed at the National Center for Inter-University Research Facilities (NCIRF) at Seoul National University. The XPS spectra of the carbon electrode were characterized by AXIS-Hsi (SHIMAZU-Kratos) and the FT-IR spectra of the carbon electrode were measured by Spotlight 200i (Perkinelmer) which are installed at the chemical and biological engineering research facilities (CBERF) at Seoul National University. The Raman spectra were measured by DXR2xi, which is installed at the National Center for Inter-University Research Facilities (NCIRF) at Seoul National University. The UPS measurements were obtained by PHI 5000 Versa Probe, which is installed at the KIST Advanced Analysis Center at Korea Institute of Science and Technology. TRPL spectra were characterized under exposure to 520 nm pulse laser (Pico-Quant). The photovoltaic properties of the PSCs were measured using I–V tracer (MP-160) under

standard AM 1.5 G (100 mW cm^{-2}) illumination from a xenon lamp (500 W), calibrated with a KG 5-filtered Si reference cell (K801; McScience Inc). The IPCE spectra were measured using K3100 Solar Cell IPCE System (McScience) without bias light. V_{oc} at the light condition and EIS of the PSCs were characterized by the Zive Lab equipment (WonATech). The measured EIS spectra were fitted to equivalent electrical circuits using the Z-view analyst software (ZMAN). The apparent contact angles of deionized water on the untreated and fluorine plasma-treated carbon electrode surfaces were measured by SmartDrop (FEMTOFAB Co., Korea). The perovskite surface change of the active layer after immersion in water was observed using an optical microscope (Lv100 microscope; Nikon).

3. Results and Discussion

3.1. Interface engineering of C-PSCs based on 2D perovskite interfacial layer

3.1.1. Fabrication of interface-engineered C-PSCs with 2D PSK perovskite

Figure 28 indicates a schematic illustration of the processes used for the introduction of carbon electrode on 3D PSK and interfacial growth of PSK layer. To fabricate C-PSCs, c-TiO₂, meso-TiO₂, and 3D PSK layers were processed by the same method with the conventional methods employing spiro-OMeTAD and Au electrode [124]. Triple cation-mixed halide perovskite was used for high efficient and stable device, and its composition contains excess PbI₂ (3 mol%) to passivate GBs and induce larger crystalline grains [125]. The 3D PSK layer was prepared using a one-step solvent engineering method as described in the previous research [124]. Conductive carbon paste, composed of graphite, carbon black and binder, was deposited onto the 3D PSK film using a screen-printing method to form about a 70 μm-thick carbon electrode. For the interfacial growth of 2D PSK layer, 10 mg mL⁻¹ of PEAI solution in IPA was dropped onto a carbon electrode. Prior to spin coating, the

sample was set aside for 30 s so that the solution penetrated sufficiently through the carbon into the 3D PSK/carbon interface. PEAI reaching the 3D PSK surface reacted with the residual PbI_2 on the GB and surface of 3D PSK, bring about *in situ* growth of PEA_2PbI_4 as an interfacial 2D PSK layer. FE-SEM images express cross-sections of C-PSC, prepared according to the above method, as presented in **Figure 29**.

The interfacial growth of 2D PSK is expected to provide better contact between the perovskite and carbon layer, thereby improving hole transport by eliminating the voids at the interface. An energy band diagram of the device and charge transport behavior that occurs by employing the 2D PSK interfacial layer is illustrated in **Figure 30**. Generally, the 2D PSK has a higher valence energy level and wider bandgap than the 3D PSK [88], and especially PEA_2PbI_4 has a lined up valence energy level with a triple cation-mixed halide perovskite for favorable hole transport, and higher conduction levels to block the charge recombination, induced by undesirable electron flow [89].

Elemental mapping using the FE-EPMA was performed to confirm PEAI permeation through the carbon electrode following PEAI treatment (**Figure 31**). C and I elemental signals were detected on the cross-section of a manufactured device treated with PEAI. In the region

of perovskite layers below the carbon electrode, the weak C atomic signal and the strong I atomic signal are indicated in blue and red, respectively. As a result of this, strong C signal and weak I signal were measured for the entire carbon electrode suggesting PEAI penetration.

To verify the formation of the 2D/3D hybrid PSK film, the perovskite layer was investigated after peeling off the deposited carbon electrode. In the **Figure 32**, FE-SEM images indicated the changes in the morphology of the 3D PSK surface according to PEAI treatment on the carbon electrode. The pristine 3D PSK film is densely packed, with 200 – 400 nm crystallites with grain boundaries. In contrast, the perovskite film after PEAI treatment formed a 2D/3D hybrid PSK, revealing a smoother surface morphology with completely covered and passivated GBs by the 2D PSK. This indicates that the surface defects present in the 3D PSK film were reduced through the interfacial growth of the 2D PSK [126]. As additional information on interfacial 2D PSK layer formation, XRD patterns were collected from the 3D PSK and 2D/3D hybrid PSK films. Both samples exhibited typical diffraction peaks corresponding to the black perovskite phase, and a peak at 12.7° indicates the presence of excess PbI_2 in the crystalline 3D PSK films (**Figure 33**) [91]. In an enlarged range XRD pattern, a pronounced peak at 5.4° appeared for the

PEAI-treated sample, which is ascribed to the (002) crystal plane of $\text{PEAI}_2\text{PbI}_4$ [127, 128]. Moreover, it is also noteworthy that the peak intensity of PbI_2 after PEA treatment was reduced due to the reaction of PbI_2 and PEA. This clearly demonstrates the formation of PEA_2PbI_4 from residual PbI_2 on the 3D PSK layer through PEA treatment on the carbon electrode. SSPL measurements were conducted to confirm the presence of a 2D PSK interlayer and to analyze the PL properties, as indicated in **Figure 34**. The samples were prepared on a glass substrate to eliminate the quenching effect by TiO_2 , which tends to extract excited electrons. Given the high absorption coefficient of the perovskite layer at an excitation wavelength of 430 nm, the light penetration depth was only about 100 nm [98, 129]. Thus, most charges were generated near the top or bottom surface, depending on the excitation direction. The samples were excited from the glass side or top surface of perovskite film; there was little difference between the two spectra. When excited from the top surface of perovskite film, the spectrum corresponding to the PEA-treated sample exhibited a characteristic PEA_2PbI_4 peak at 510 nm [84], indicating 2D PSK formation on the top surface. Additionally, considering the short light penetration depth, the relatively small peak of the 2D PSK compared with the peak of the 3D PSK (at 760 nm) implies

that the newly formed 2D PSK layer was extremely thin, as it grows in the gap between the 3D PSK and carbon layers. Taken together, these results provide convincing evidence for the interfacial growth of the 2D PSK at the 3D PSK/carbon interface with PEAI treatment.

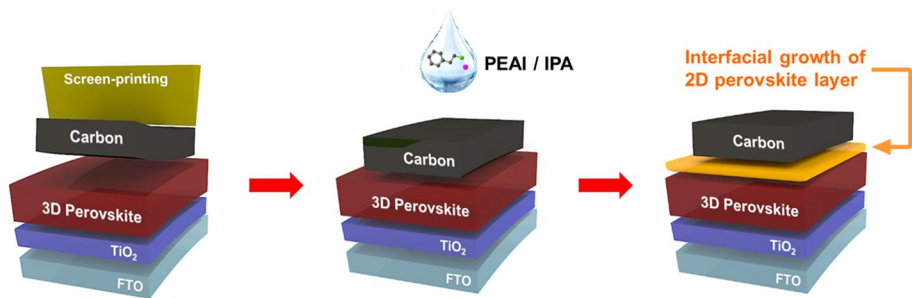


Figure 28. Schematic illustration showing the procedures to deposit a carbon electrode and induce interfacial growth of the 2D PSK layer.

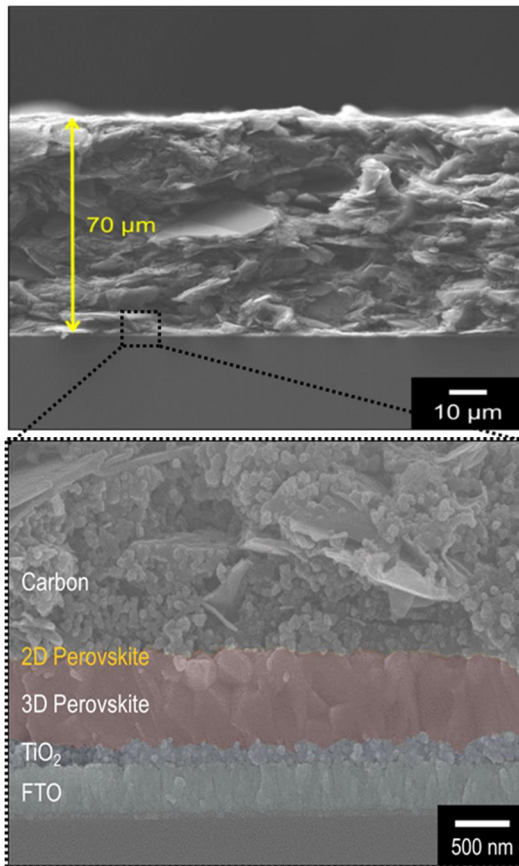


Figure 29. Cross-sectional FE-SEM images of the C-PSC with the 2D PSK interfacial layer.

N

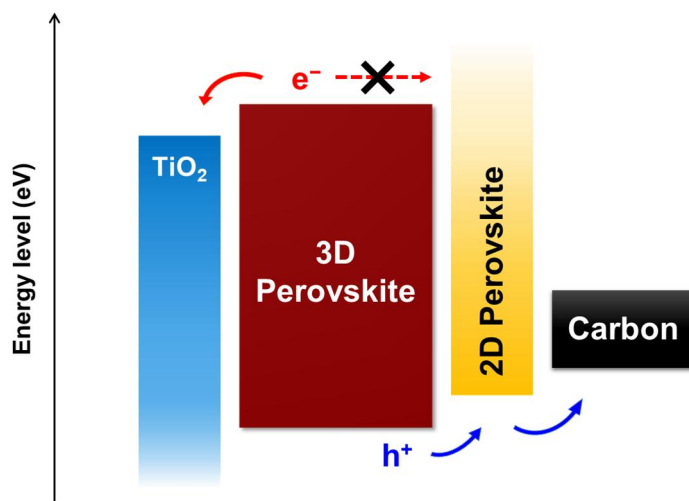


Figure 30. Energy band diagram of each component in the fabricated C-PSC.

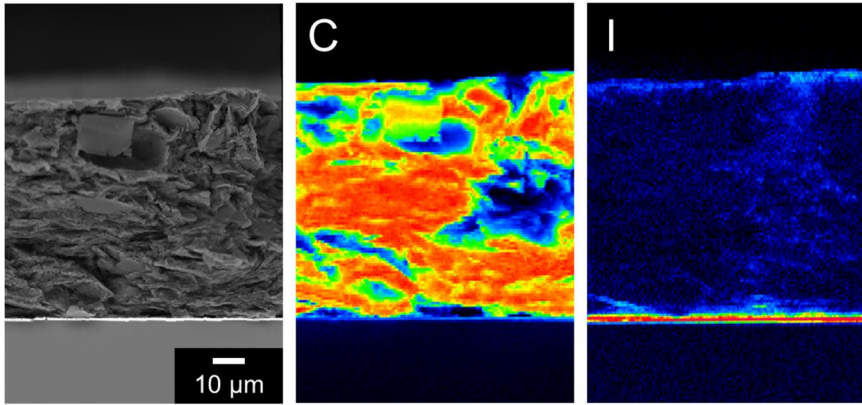


Figure 31. Backscattered electron image (BSE) and elemental mapping using FE-EPMA of carbon (C) and iodine (I) in a cross-section of the fabricated C-PSC.

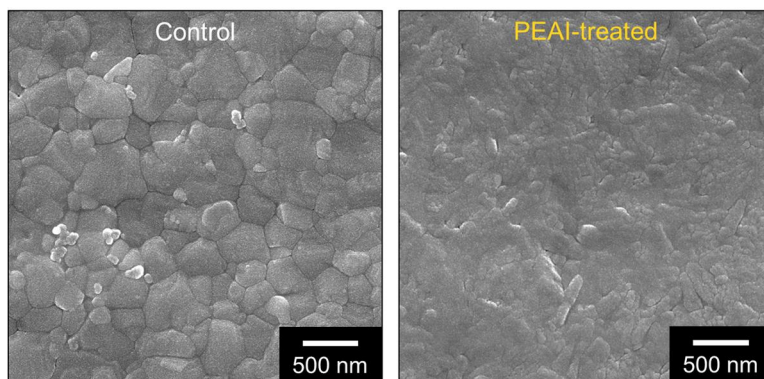


Figure 32. Top view of FE-SEM image w/o and with PEAI treatment.

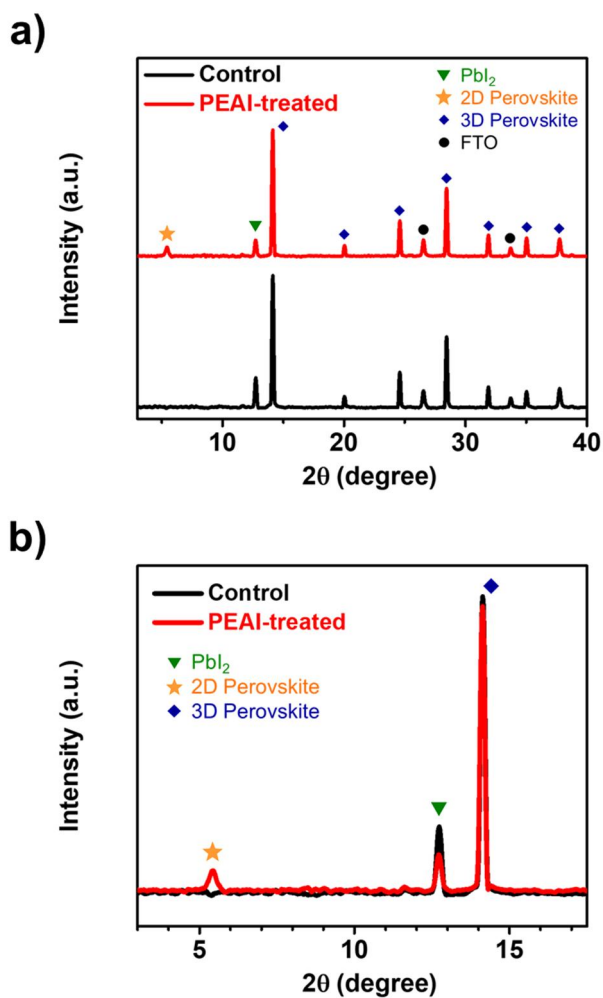


Figure 33. (a) Full and (b) expanded range of XRD patterns of the perovskite films w/o and with PEAI treatment. Note that the carbon layer was peeled off to reveal the perovskite layer underneath for measurement.

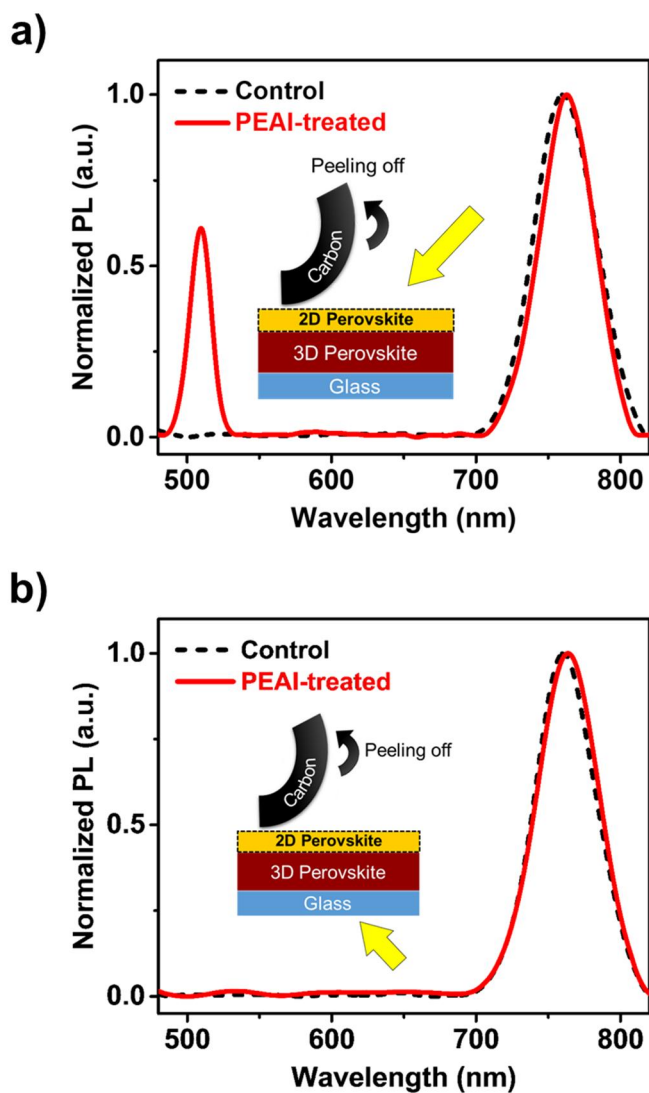


Figure 34. SSPL spectra of the perovskite films w/o and with PEAI treatment. (a) Samples were excited from the top surface of PSK, and (b) glass side by light irradiation at 430 nm, respectively. The carbon layer was peeled back to eliminate its quenching effect.

3.1.2. Photovoltaic performance of interface-engineered C-PSCs with 2D perovskite

The effects of interfacial growth of the 2D PSK on the photovoltaic performance of C-PSC were investigated. J - V curves for the control (without PEAI treatment) and PEAI-treated devices are shown in **Figure 35** and the extracted PV parameters are summarized in **Table 1**. The pristine 3D PSK-based C-PSC exhibited a power conversion efficiency (PCE) of 11.86%. After PEAI treatment, PCE increased to 14.90% and overall PV parameters improved. Apart from efficiency improvement, it is prominent that J - V hysteresis was also alleviated by the PEAI treatment ($\text{PCE}_{\text{rev-fwd}} = 1.02\%$) compared with that of the control device ($\text{PCE}_{\text{rev-fwd}} = 1.96\%$). Previous studies have reported that the hysteresis behavior of PSC mainly comes from ion migration and subsequent accumulation at the interfaces of the perovskite and contact layers [130, 131]. Because low-dimensional perovskites have a high ion migration barrier [83], this 2D/3D hybrid PSK-based C-PSC effectively blocked the ion migration pathway and revealed a less hysteresis behavior.

To highlight an exceptional effect of post-PEAI treatment on the deposited carbon electrode, PEAI pre-treated C-PSC on 3D PSK before carbon electrode printing and C-PSC treated after MAI were prepared for comparison purposes. J - V curves of each device are displayed in

Figure 36. MAI treatment on the carbon electrode, instead of PEAI, increased the PCE from 11.72% to 12.80%, demonstrating improved interfacial contact between perovskite/carbon *via* the additional 3D PSK growth [100]. However, only the fill factor (FF) was slightly improved, and overall efficiency improvements were limited. PEAI solution (10 mg mL⁻¹) was directly applied to the 3D PSK layer to form a 2D/3D hybrid PSK having a 2D PSK as a capping layer, followed by a deposition of the carbon electrode. Although the 2D PSK layer formed by PEAI pre-treatment improved the V_{oc} and FF by reducing charge recombination, this enhancement was inferior to that obtained by the post-treatment on carbon in the proposed approach. This indicates that this method has the synergistic effects of bridging the gap at the perovskite/carbon interface and inducing optimum band alignment, thus minimizing charge recombination.

The $I-V$ curve of the best-performing device with PEAI treatment is shown in **Figure 37**; this device has a PCE of 15.66% with a short-circuit current density (J_{sc}) of 21.44 mA cm⁻², V_{oc} of 1.07 V, and a FF of 0.68. Statistical distributions and parameters of PCE were confirmed with 25 devices of each type, as presented in **Figure 38**. The average PCEs of the control and PEAI-treated devices were 11.53% and 14.54%, respectively.

In particular, since V_{oc} is the most improved parameter, this improvement was verified by measuring steady-state V_{oc} [132]. As described in **Figure 39a**, the stabilized V_{oc} values for the control and PEAI-treated devices were 0.99 V and 1.03 V, respectively. And also, the IPCE spectra illustrated in **Figure 39b** support the enhancement of J_{sc} by forming a 2D/3D hybrid PSK. The spectrum of the PEAI-treated device manifested a high external quantum efficiency (EQE) of over 85% in the range of 450 – 750 nm; the integrated J_{sc} was 21.56 mA cm⁻², higher than that of the control device (20.54 mA cm⁻²). The steady-state output of the PEAI-treated device was monitored at a maximum power voltage (0.785 V). A stabilized photo-current density of 18.65 mA cm⁻² and stabilized PCE of 14.64% were achieved immediately, which then remained stable over 300 s under illumination (**Figure 39c**). This result is in good agreement with the PV parameters based on J - V characteristics and demonstrates the reliability of the device, supporting a low hysteresis effect [133, 134]. Furthermore, device performance was measured for a larger active area of 1 cm². As shown in **Figure 39d**, the device exhibited a PCE of 10.05% with a J_{sc} of 21.33 mA cm⁻², V_{oc} of 1.03 V, and FF of 0.45.

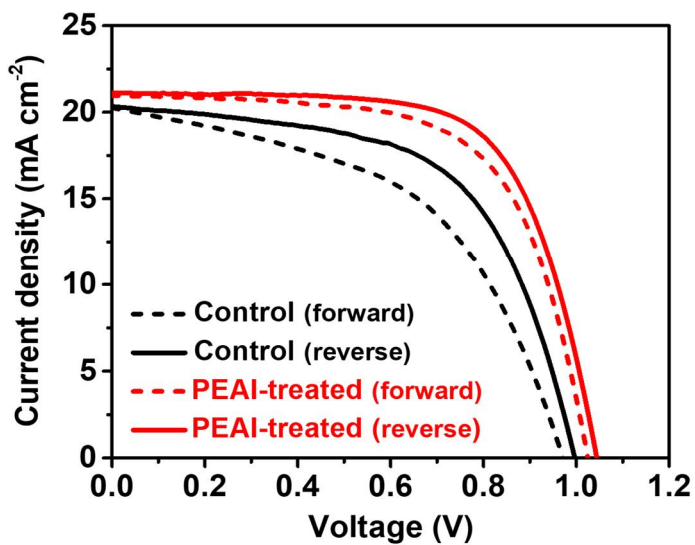


Figure 35. J - V characteristics of PSCs w/o and with PEAI treatment as a function of scan direction.

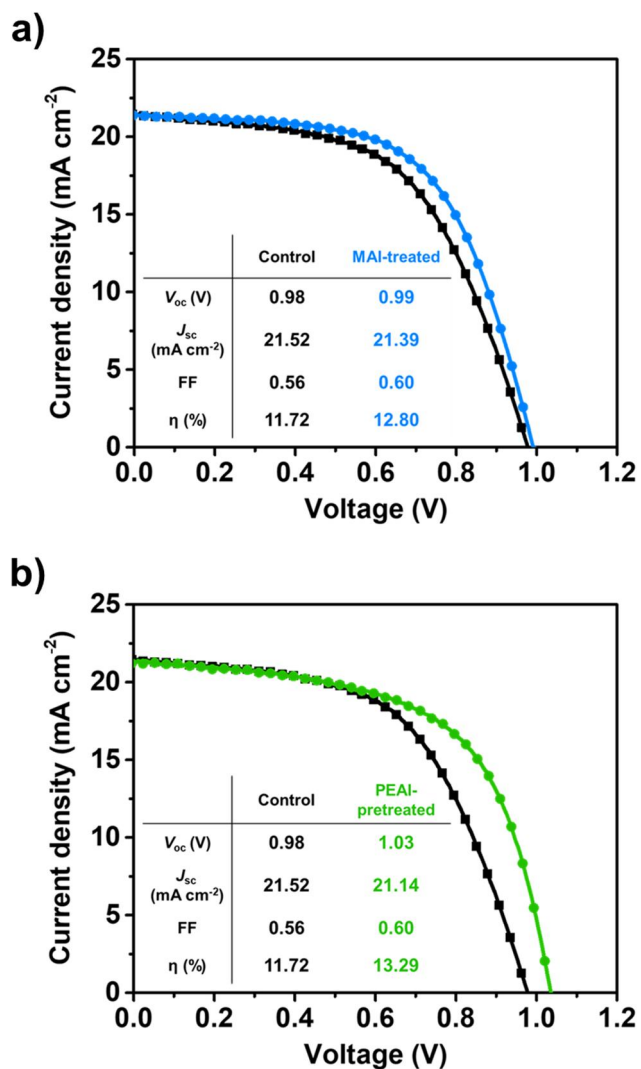


Figure 36. J - V characteristic comparison for C-PSCs with (a) MAI post-treatment and (b) PEAI pre-treatment.

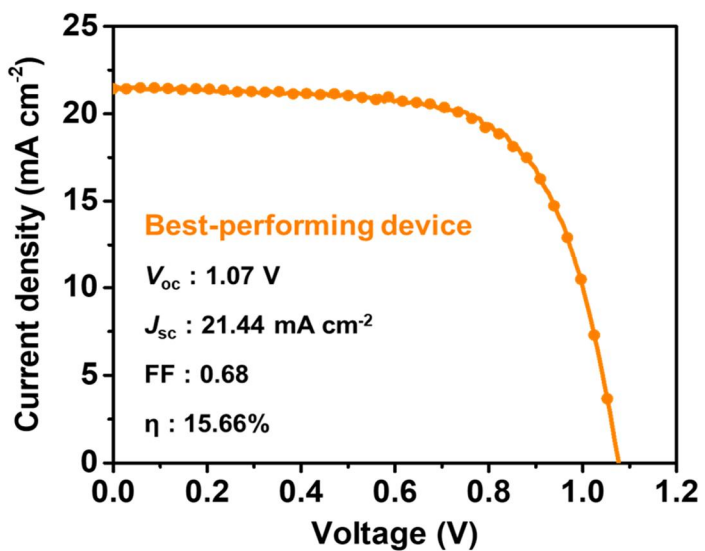


Figure 37. J - V characteristics of the best-performing device with 2D/3D hybrid PSK.

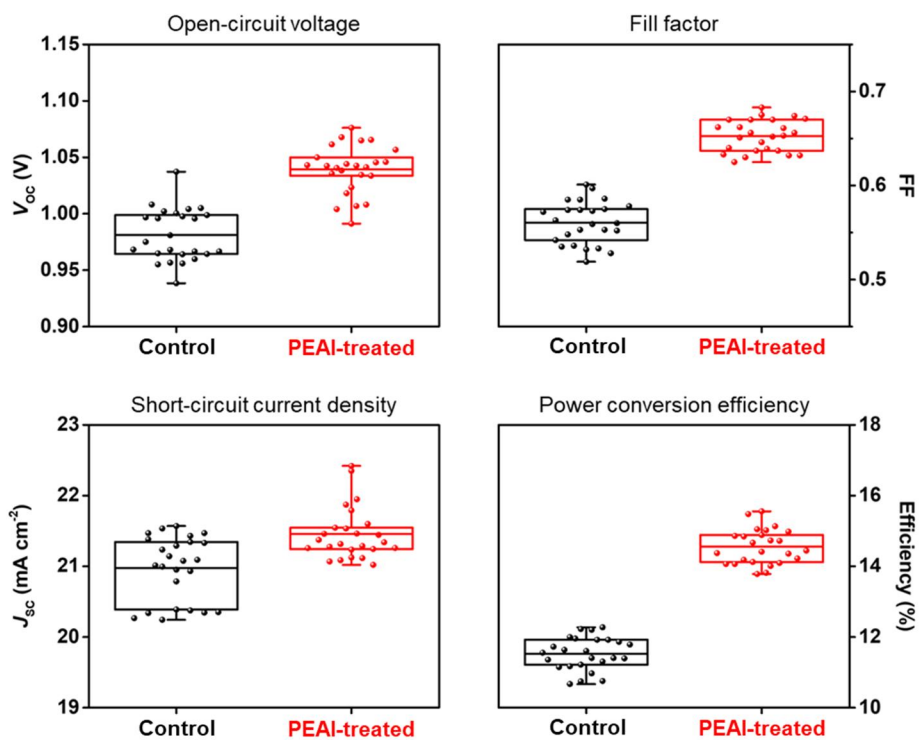


Figure 38. Distribution of photovoltaic parameters (V_{oc} , FF, J_{sc} , and PCE) of C-PSCs w/o and with PEAI treatment. The mean values are marked as solid lines in the boxes.

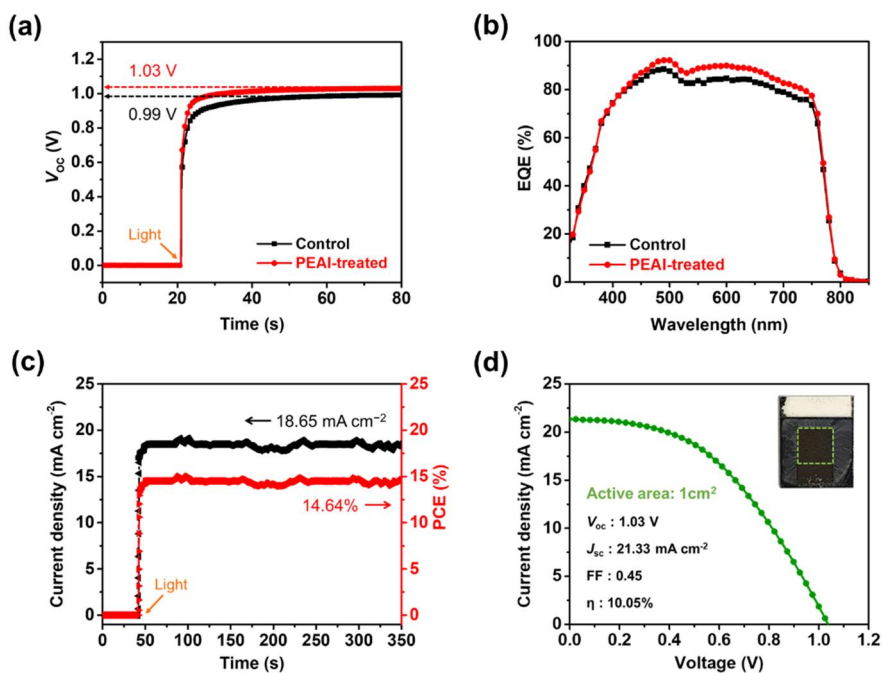


Figure 39. (a) The steady-state V_{oc} curves measured under 1 sun illumination of each type. (b) IPCE spectra of C-PSCs w/o and with PEAI treatment. The integrated J_{sc} is 20.54 and 21.56 mA cm^{-2} , respectively. (c) steady-state performance measured at V_{max} of 0.785 V, and (d) device performance with an active area of 1 cm^2 . The inset displays a digital photograph of C-PSC with PEAI post-treatment; the dashed green square represents an active area.

Table 1. Photovoltaic parameters C-PSCs w/o and with PEAI treatment, depending on scan direction.

Device	Scan direction	J_{sc} (mA cm ⁻²)	V_{oc} (V)	FF	PCE (%)
Control	Forward	20.26	0.97	0.50	9.90
	Reverse	20.35	0.99	0.59	11.86
PEAI-treated	Forward	20.97	1.02	0.65	13.88
	Reverse	21.12	1.04	0.68	14.90

3.1.3. Interfacial charge carrier dynamics in interface-engineered C-PSCs with 2D perovskite

First of all, to check the charge transfer at the interface, direct current conductivities (σ_0) for pristine and PEAI-treated carbon were obtained from I - V characteristics (**Figure 40**) using the equation $I = \sigma_0 A d^{-1} V$, where A is the active area and d is the thickness of the carbon [122]. The calculated conductivities indicated a value of 9.2 S cm^{-1} , indicating no change in the conductivity of carbon by PEAI incorporation. Therefore, the improvement in device performance originates solely from the PSK/carbon interface. Specifically, the interfacial growth of the 2D PSK layer provides better perovskite/carbon contact by bridging the gap in the interface. More importantly, the well-matched valence band and higher conduction band of the 2D PSK enable faster hole transport and less charge recombination at the perovskite/carbon interface.

TRPL decay measurements were performed to validate the hypothesis base on interfacial hole transfer kinetics between the perovskite/carbon electrode. The PL decay curves were fitted with a bi-exponential decay function [135]; the fitted parameters are summarized in **Table 2**. The average PL lifetime (τ_{avg}) was estimated from two-time components (τ_1 and τ_2), based on the equation:

$$\tau_{avg} = \sum_i A_i \tau_i^2 / \sum_i A_i \tau_i$$

Figure 41a describes the decay curves of the samples after peeling away the carbon electrode, similar to the procedure used prior to steady-state PL measurements. τ_{avg} increased from 81.7 to 95.2 ns with PEAI treatment. The increase in the PL lifetime indicates that the 2D PSK interface layer efficiently eliminated the trap states on the 3D PSK surface by passivation, ultimately reducing non-radiative recombination [136]. Conversely, upon contact with the carbon electrode, the PEAI-treated sample manifested a greatly shortened τ_{avg} (36.9 ns) compared with the control sample (41.3 ns) without PEAI treatment (**Figure 41b**). This dramatically quenched PL lifetime is attributable to more efficient hole transport *via* the favorable alignment of energy level [89, 91].

V_{oc} as a function of light intensity gives details of the recombination processes (**Figure 42**). Slopes in the semi-logarithmic plots for the devices without and with PEAI treatment are calculated to be $1.94 kT/q$ and $1.49 kT/q$, respectively (where k is Boltzmann's constant, T is the absolute temperature, and q is the elementary charge). A slope value close to kT/q suggests dominant bi-molecular recombination and minor trap-assisted recombination in the device [137-139]. The decrease in the slope value with PEAI treatment implies that trap-assisted recombination

was reduced by passivation and the pore-filling effects of the 2D PSK.

EIS measurements were conducted to further characterize the interfacial charge transport and recombination dynamics of the devices.

Figure 43 presents Nyquist plots in the frequency range (1 MHz to 1 Hz) under 1 sun illumination at different biases ranging from 0 V to 1.0 V. Two main arcs were apparent in the plots. The first arc at a high frequency typically corresponds to charge transport processes in the HTM or at the HTM/electrode interface. However, in the sample, it corresponds to the hole transport process at the perovskite/carbon interface [140, 141]. The arc at low frequency is related to interfacial charge recombination [75, 126]. The results were fitted using an equivalent circuit model. The fitted parameters are summarized in **Table 3**. The reduced charge transport resistance (R_{ct}) of the PEAI-treated device indicates less resistive energy loss during charge transport through the perovskite/carbon interface and the carbon itself. This should lead to a higher FF for the PEAI-treated device consistent with $J-V$ characteristics [142]. In contrast, the PEAI-treated device exhibited increased charge recombination resistance (R_{rec}). Despite the absence of an HTM, the higher conduction level of the 2D PSK layer than that of the 3D PSK effectively prevented electron diffusion into the carbon and

contributed to an enhancement of V_{oc} .

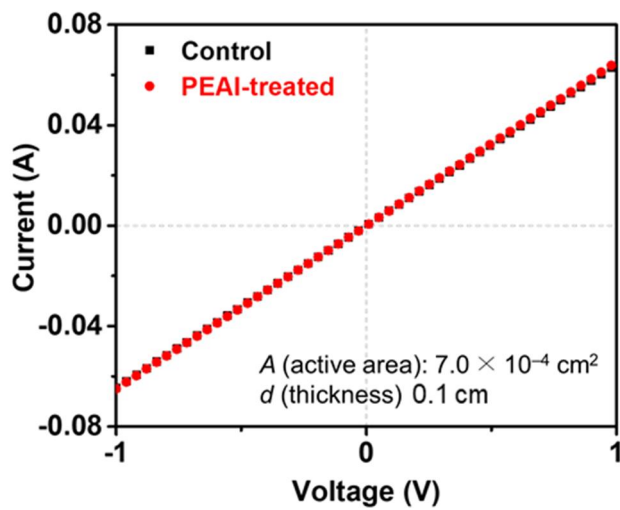


Figure 40. I - V characteristics for carbon electrodes w/o and with PEAI treatment.

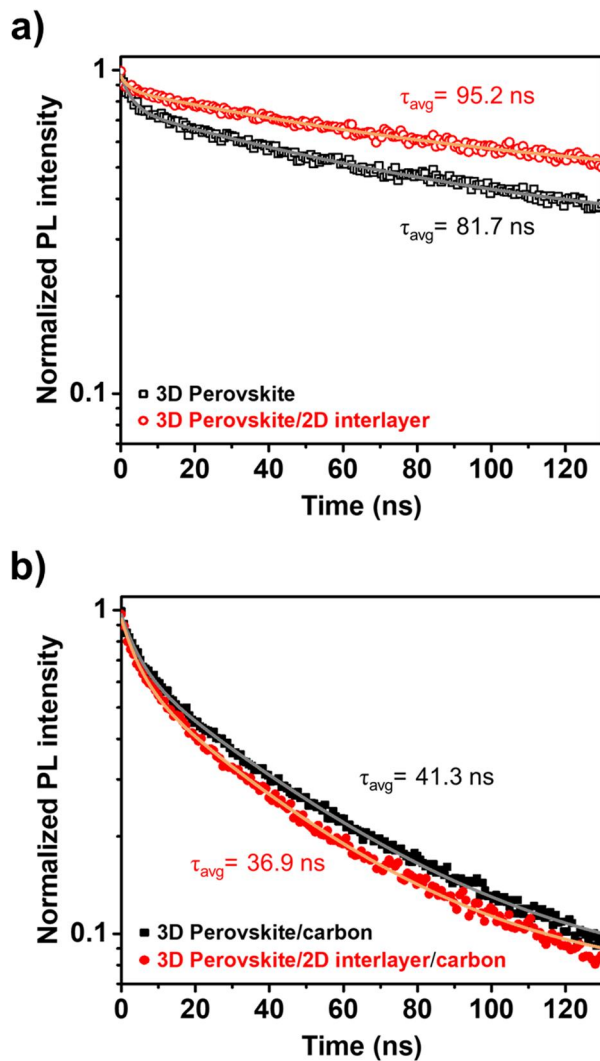


Figure 41. TRPL decay curves for perovskite films w/o and with PEAI treatment. The samples were prepared on glass and examined (a) w/o carbon (likewise for SSPL measurements) and (b) with carbon. The samples were excited from the glass side by light irradiation at 405 nm.

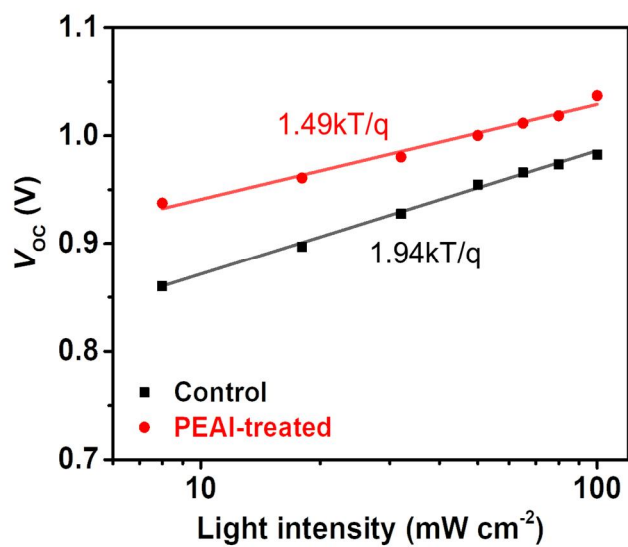


Figure 42. The V_{oc} as a function of light intensity for PSCs w/o and with PEAI treatment plotted on a semi-log scale.

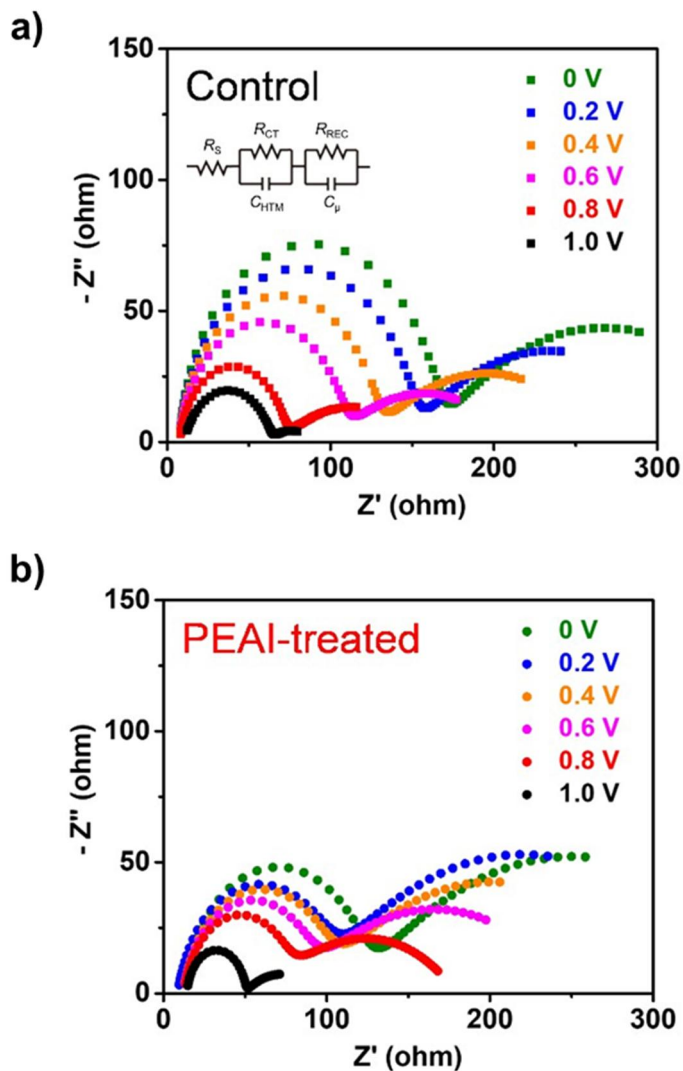


Figure 43. Nyquist plots for PSCs (a) w/o and (b) with PEAI treatment measured under illumination at different applied bias ranged from 0 V to 1.0 V. The scanning frequency ranged from 1 MHz to 1 Hz. The inset shows the equivalent circuit.

Table 2. TRPL decay parameters for the perovskite films w/o and with PEAI treatment. The bi-exponential decay equation was used for fitting the curves.

Sample	τ_1 (ns)	τ_2 (ns)	$^a)\tau_{avg}$ (ns)	A_1	A_2
Glass/3D PSK	3.1	83.0	81.7	0.21	0.47
Glass/3D PSK /interfacial 2D PSK	2.4	95.6	95.2	0.09	0.46
Glass/3D PSK/C	4.8	43.3	41.3	0.30	0.60
Glass/3D PSK /interfacial 2D PSK/C	4.8	39.2	36.9	0.32	0.55

$$^a)\tau_{avg} = \sum_i A_i \tau_i^2 / \sum_i A_i \tau_i$$

Table 3. EIS parameters for the PSCs w/o and with PEAI treatment, obtained from the Nyquist plots.

Device	V_{app} (V)	R_s (Ω)	R_{ct} (Ω)	R_{rec} (Ω)
Control	0	7.46	1.55×10^2	2.09×10^2
	0.2	7.37	1.41×10^2	1.71×10^2
	0.4	7.41	1.17×10^2	1.41×10^2
	0.6	7.43	0.97×10^2	1.05×10^2
	0.8	7.39	0.62×10^2	0.88×10^2
	1.0	10.4	0.52×10^2	0.25×10^2
PEAI-treated	0	11.8	1.08×10^2	2.62×10^2
	0.2	8.53	0.86×10^2	2.51×10^2
	0.4	11.8	0.84×10^2	2.12×10^2
	0.6	12.0	0.72×10^2	1.65×10^2
	0.8	12.3	0.57×10^2	1.10×10^2
	1.0	14.3	0.45×10^2	0.35×10^2

3.1.4. Device stability of interface-engineered C-PSCs with 2D perovskite

To test the stability, the PEAI-treated C-PSC was compared with a conventional PSC made of FTO / TiO₂ / 3D PSK / spiro-OMeTAD / Au structures. *J-V* characteristics and PV parameters of fabricated conventional PSC are indicated in **Figure 44**. The long-term stability of the non-encapsulated devices stored under ambient conditions (temperature: 25 °C, relative humidity: 40 ± 5%), as described in **Figure 45a**. The PCE of the conventional device was 18.92% at the beginning, but gradually declined over 1000 h to 13.11%, 69% of the initial performance. The conventional device can suffer from degradation, induced by both a hygroscopic dopant (Li-TFSI) in the HTM and an unstable HTM/Au interface [143, 144]. On the other hand, C-PSCs are not only free from those hazards, but the perovskite layer is protected by a hydrophobic carbon electrode. The control carbon-based device showed a smaller degradation in efficiency, from 12.20% to 9.90%, retaining 81% of its initial performance. Strikingly, the efficiency of the PEAI-treated device decreased only slightly, to 92% of its initial performance (PCE = 15.07% to 13.82%), thereby demonstrating outstanding ambient stability. It is because the 2D PSK incorporating

hydrophobic cations provided secondary protection against moisture invasion [77, 86]. The thermal stability of devices (**Figure 45b**) was investigated by periodically checking the performances of three devices heated at 100 °C and 150 °C. While heating at 100 °C, both carbon-based devices retained their performance, and even revealed enhanced efficiency, due to the reinforced perovskite/carbon interface [141]. However, the conventional device became severely degraded by the thermal diffusion of ions from the perovskite to the HTM [145]. In addition, the electrical properties of spiro-OMeTAD degraded due to void generation near the HTM/Au interface as a result of the thermal stress [146]. As the temperature increased to 150 °C, the relative efficiency of the untreated carbon-based device gradually decreased to 85%. According to the previous report, thermal decomposition is initiated at 127 °C in a triple cation-mixed halide perovskite due to the formation of mobile ions and volatilization, especially involving MA and I ions [147]. However, the PEAI-treated device maintained a high relative efficiency of 102% even after the test at 150 °C. The 2D PSK interlayer suppressed the ion migration triggered by thermal stress due to its high ion migration barrier [81, 83]. It passivated the 3D PSK surface and grain boundaries where thermal decomposition usually

begins [148]. Additionally, the remaining PEAI in the carbon electrode, as confirmed by FE-EPMA mappings, should suppress thermal decomposition [141]. Consequently, the results demonstrated that this method to post-treat the carbon electrode with PEAI is an effective way to ameliorate the ambient and thermal stabilities of PSCs.

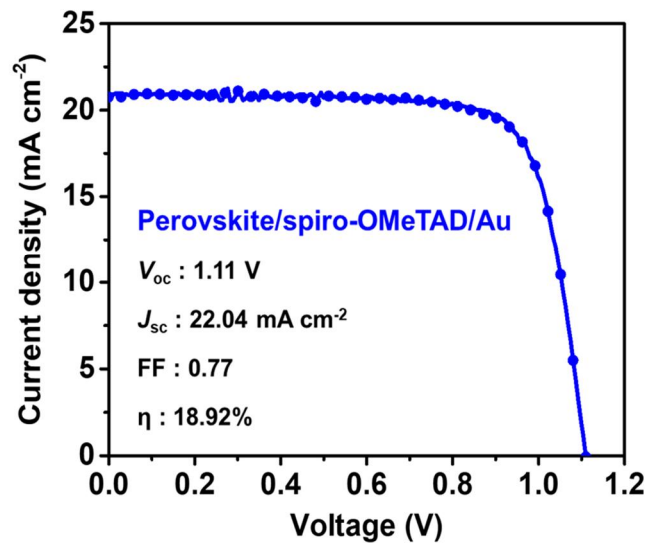


Figure 44. J - V characteristic for a conventional PSC with FTO / TiO₂ / 3D PSK / spiro-OMeTAD / Au structure.

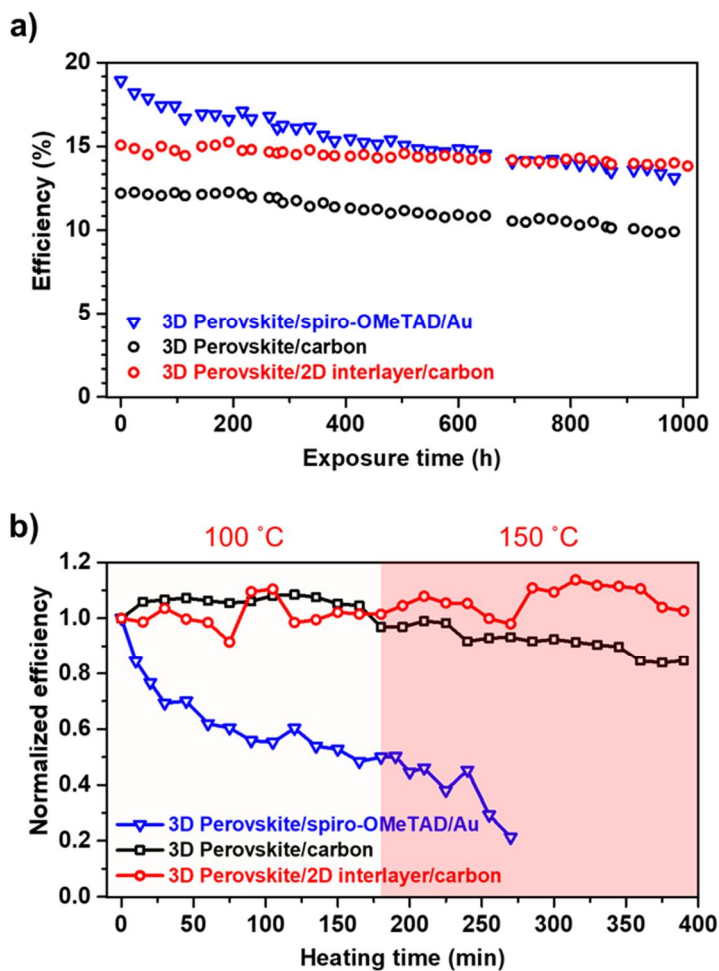


Figure 45. (a) The PCE evolution of a conventional PSC 2 an FTO / TiO₂ / 3D PSK / spiro-OMeTAD / Au structure, and C-PSCs w/o and with PEAI treatment under ambient conditions (temperature: 25 °C, relative humidity: 40 ± 5%). (b) Normalized PCE evolution of the PSCs as a function of heating time at 100 °C (0 – 180 min) and 150 °C (180 – 390 min).

3.2. Interface engineering of C-PSCs based on secondary growth of MAPbI₃ interfacial layer

3.2.1. Synthesis of colloidal PbI₂ and fabrication of C-PSCs with MAPbI₃ interfacial layer

To introduce additional PbI₂ at the interface of C-PSC, PbI₂ powder and aliphatic chain-based organic acid (number of carbon on alkyl chain (C_n) = 4, 6, and 8) were mixed in 1:2 molar ratios, and a pre-chelated structure was formed through ultra-sonication. Subsequently, it was mixed with CB at a ratio of 10 mg mL⁻¹, followed by a colloidal PbI₂ capped with an organic acid that was prepared through ultra-sonication as an external energy source capable of forming colloids. As displayed in **Figure 46a**, a colloidal PbI₂ solution dispersed evenly in a non-polar solvent was prepared. Generally, PbI₂ molecules and PbI₂-based perovskite precursor dissolve easily in polar and polar aprotic solvents (e.g. DMF, GBL, DMSO, and DMA), when considering Mayer bond order [149], Hansen's solubility parameters (HSP) [150], dielectric constant and donor number (D_N) [151], while anti-solvents such as CF, CB, TOL, DCB, and DEE are almost impossible to dissolve or disperse [152]. On the other hand, in the colloidal PbI₂, the carboxylic acid group of the organic acid interacted with PbI₂, so that a hydrophobic alkyl chain

appeared in the direction of the CB and could be well dispersed. The chemical reaction to form colloidal PbI_2 can occur via three possible mechanisms, as schematically illustrated in **Figure 46b**. In general, carboxylic acid or aliphatic organic acid molecules can form monodentate ($\text{C}=\text{O}-\text{PbI}_2$) or a bidentate ($\text{COO}=\text{PbI}_2$) chelate with Pb (II) to replace the I^- ligand located at the corner of the octahedron $[\text{PbI}_{6-x}]^{4-}$ ($x = 4, 5, \text{ or } 6$) through HI volatilization [153]. Interestingly, the adjusted octahedral structure has a considerably larger configurational Gibbs entropy than the original $\text{I}-\text{Pb}-\text{I}$ layer structure [154]. In a previously known study, inorganic perovskite quantum dots (QDs) capped with organic acids were produced by the reaction of long alkyl chains ($C_n \geq 9$) with organic acids at high temperatures [155, 156], and micron-sized PbI_2 sheets were formed through chemical substitution of organic acids or aggregation of PbI_2 nanoparticles [157, 158].

FE-SEM and TEM images (**Figures 47a and 47b**) show that the colloidal PbI_2 was present in a hexagonal crystal having a size of about 50 nm. In addition, HR-TEM images indicate that the prepared colloidal PbI_2 is a crystal with three-dimensionality (**Figure 47c**). According to the SAED pattern of PbI_2 , colloidal PbI_2 has a well-shaped hexagonal tetradecahedron structure grown in the (001) and (011) lattice directions

(Figure 47d) [159, 160]. In addition, the (011) facet ratio of colloidal PbI_2 is higher than that of conventional powder PbI_2 , which is evident in Figure 48.

Figure 49 illustrates the device structure of the C-PSC fabricated in this section and the formation of the secondary growth of the MAPbI_3 interfacial layer based on colloidal PbI_2 . For secondary growth-based hierarchical perovskite layer *via* post-treatment of colloidal PbI_2 , 10 mg mL^{-1} of colloidal PbI_2 solution was dropped onto a carbon electrode on a fabricated C-PSC. Prior to spin-coating, the sample was set aside for 30 s so that the solution penetrated sufficiently through the carbon into the perovskite/carbon interface. After the introduction of additional PbI_2 , 20 mg mL^{-1} of MAI solution in IPA was dropped onto a carbon electrode, followed by 10 s of wetting time for sufficient penetration of MAI through the carbon electrode. MAI reaching the perovskite interface reacts with colloidal PbI_2 , resulting in *in situ* growth of the additional MAPbI_3 interfacial layer. Digital photographs of pristine C-PSC and C-PSC that have been through each processing step for interfacial growth are exhibited in Figure 50.

To verify that the carbon electrode has enough pores to pass through the colloidal PbI_2 nanocrystals, specific surface area analysis of the

carbon electrode was performed while confirming the amount of nitrogen adsorption/desorption based on the BET equation. In **Figure 51**, FE-SEM images showed the cross-section and surface morphology of the deposited carbon electrode to be used for specific surface area analysis. The pore volume ($0.073 \text{ cm}^3 \text{ g}^{-1}$) and average pore size (55.31 nm) calculated by the BJH equation were confirmed, which is indicated in **Figure 52** and the relevant parameters are summarized in **Table 4**. Elemental mapping using the FE-EPMA was performed to confirm colloidal PbI_2 permeation through the carbon electrode and interfacial growth of MAPbI_3 following MAI treatment (**Figure 53**). Carbon (C), lead (Pb) and iodine (I) elemental signals were detected on the cross-section of a manufactured device treated with colloidal PbI_2 and MAI. In the region of the perovskite layer below the carbon electrode, the weak C atomic signal and the strong Pb, I atomic signal are indicated in blue and red, respectively. As a result of this, strong C signal and weak Pb, I signal were measured for the entire carbon electrode suggesting colloidal PbI_2 and MAI penetration.

a)



b)

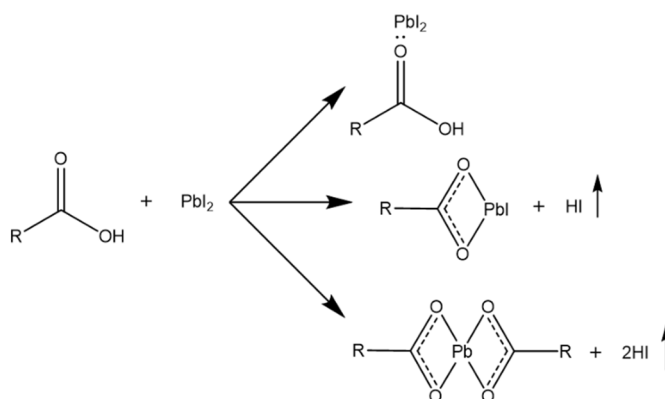


Figure 46. (a) Digital photograph of colloidal PbI_2 solution dispersed in chlorobenzene. (b) Proposed chemical reaction mechanisms of carboxylic acids and PbI_2 .

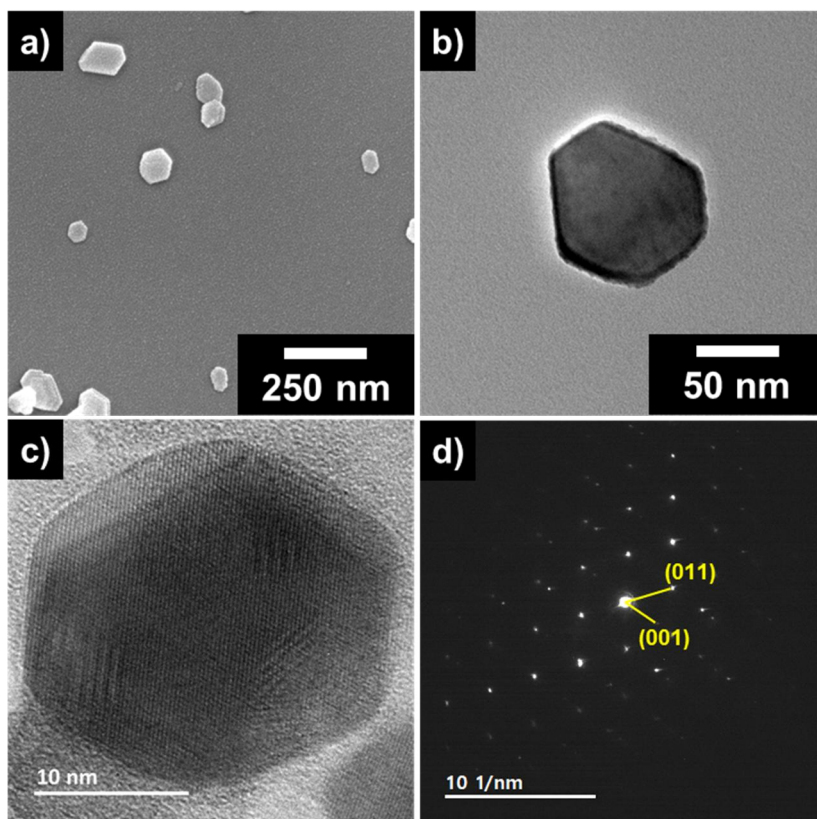


Figure 47. (a) FE-SEM image of spin-coated colloidal PbI_2 on Si wafer. (b) TEM image of the colloidal PbI_2 . (c) HR-TEM image of colloidal PbI_2 . (d) SAED pattern of colloidal PbI_2 .

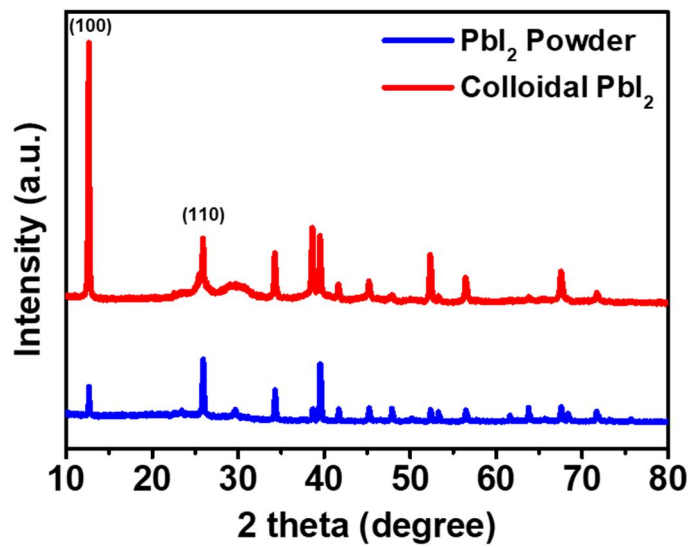


Figure 48. XRD patterns of pristine PbI₂ power and prepared colloidal PbI₂ with typical PbI₂ peaks.

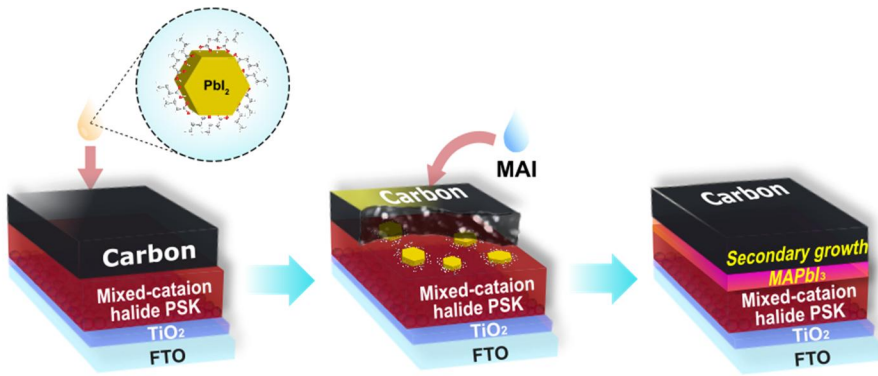


Figure 49. Schematic illustration showing the procedures to deposit a carbon electrode and induce interfacial growth of MAPbI₃ layer based on the introduction of colloidal PbI₂.

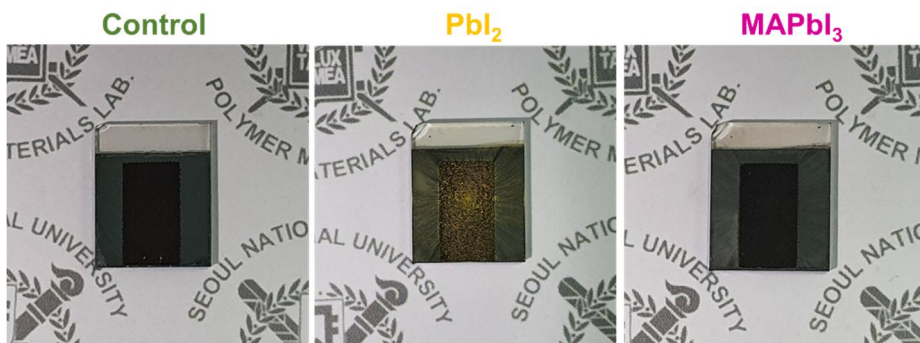


Figure 50. Digital photograph of pristine C-PSC, PbI₂-treated C-PSC, and C-PSC with secondary growth of MAPbI₃ of interfacial layer.

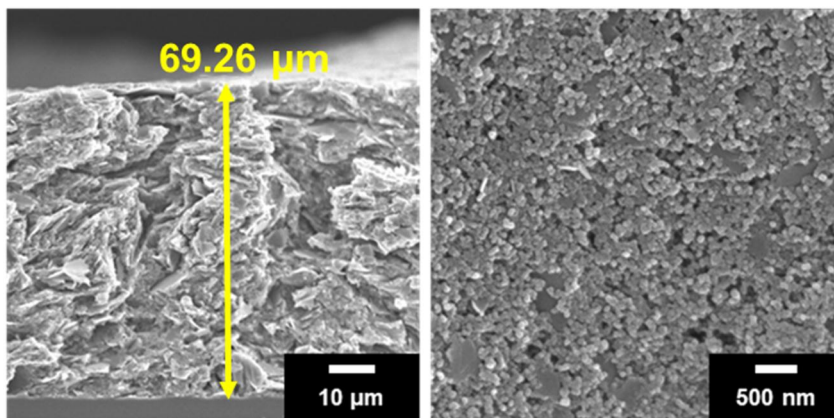


Figure 51. Cross-sectional and surficial FE-SEM images of the deposited carbon electrode using for specific surface area analysis.

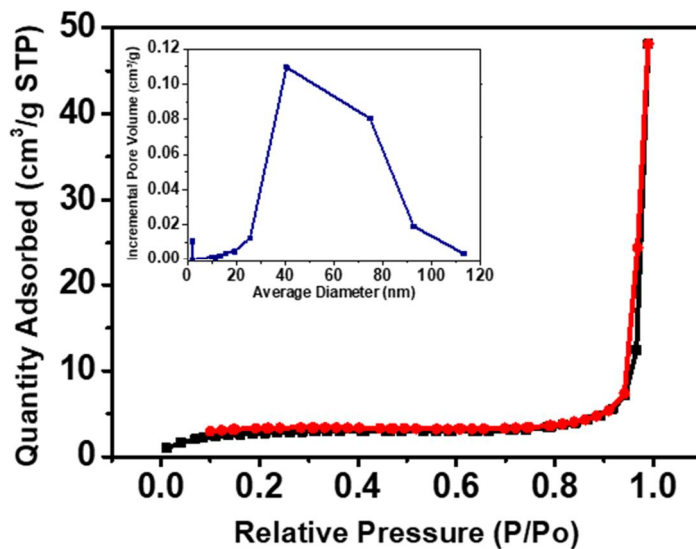


Figure 52. BET surface analysis of the carbon electrode. The inset indicates a distribution of average pore diameter.

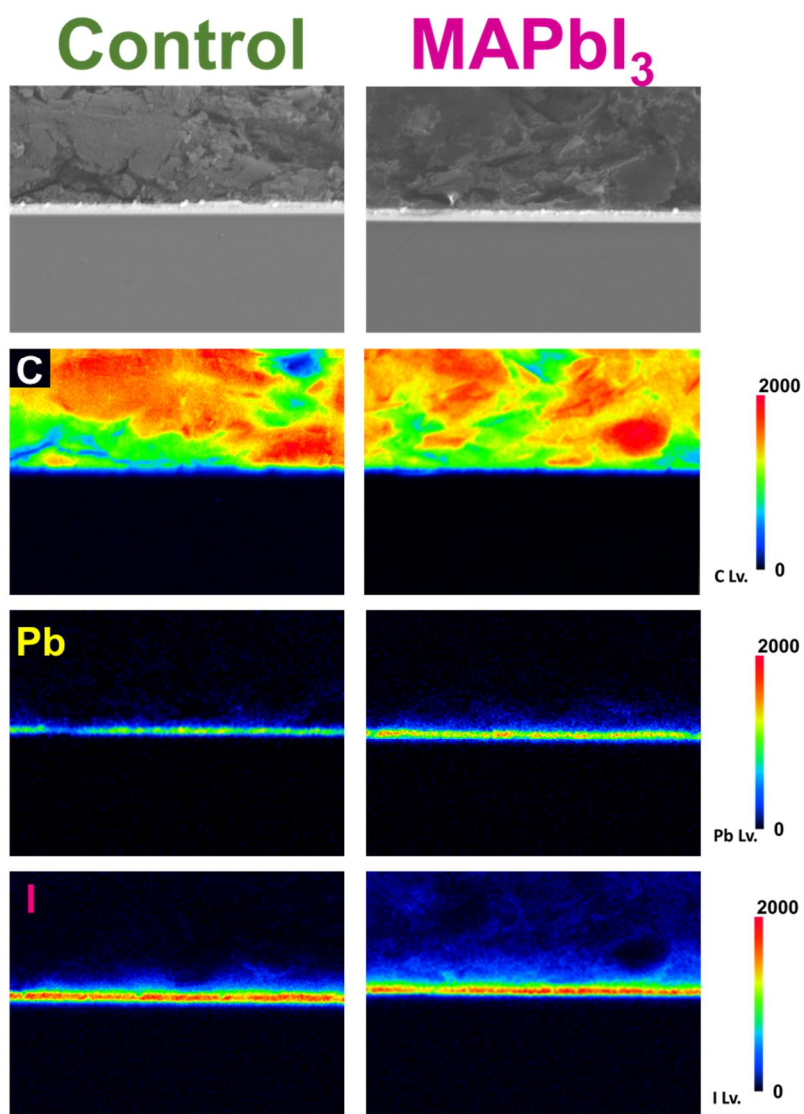


Figure 53. Elemental mapping using FE-EPMA of carbon (C), lead (Pb), and iodine (I) in a cross-section of the fabricated C-PSC w/o treatment, and with secondary growth of MAPbI₃ interfacial layer.

Table 4. BET and BJH analysis parameters for the carbon electrode.

Sample	BET surface Area (m²/g)	Pore volume (cm³/g)	Average pore size (nm)
Painted-carbon Electrode	6.92	0.073	55.31

3.2.2. Characterization of colloidal PbI_2 -based MAPbI_3 interfacial layer

To verify the formation of the second growth MAPbI_3 based on colloidal PbI_2 , the perovskite layer was investigated after peeling off the deposited carbon electrode. In **Figure 54**, FE-SEM images showed the changes in the morphology of an intrinsic triple cation PSK surface according to colloidal PbI_2 and sequential MAI treatment on the carbon electrode. The pristine perovskite film is densely packed, with 200 – 400 nm crystalline with grain boundaries. After the treatment of the colloidal PbI_2 solution, nano-sized hexagonal PbI_2 particles were evenly applied to the surface of the perovskite film. Further, the MAPbI_3 interfacial layer was grown secondarily by further treating the MAI solution on the PSK surface where the PbI_2 particles were distributed. The additionally processed MAI reacts with the introduced PbI_2 nanoparticles. In addition to newly growing the MAPbI_3 perovskite interfacial layer, it reacts with the residual PbI_2 present in the defect site and GB in the existing PSK layer to form a hierarchical PSK in which crystals are interconnected [161, 162]. **Figure 55** indicates the change in surface morphology due to the increase in Z-height and the formation of the interfacial layer due to the introduction of additional PbI_2 particles and the formation of the

MAPbI₃ interfacial layer using AFM.

As additional information on MAPbI₃ interfacial layer, XRD patterns were collected from the triple cation-based original perovskite film and the film treated with each solution (colloidal PbI₂, MAI), sequentially. Samples exhibited typical diffraction peaks corresponding to the black perovskite phase, and a peak at 12.7° indicates the presence of excess PbI₂ in the crystalline triple cation perovskite films (**Figure 56**) [91]. The crystallinity of the perovskite is slightly lower in the hierarchical film with MAPbI₃ interfacial layer than the original PSK, confirmed from the change of full width at half maximum (FWHM) value. Specifically, this result manifests that the peak distribution is dispersed according to the perovskite peak shift in the enlarged range XRD pattern (12.5° to 14.5° and 28.0° to 32.5°) [124, 163]. Moreover, it is also noteworthy that the overall peak intensity of PbI₂ after MAI treatment was slightly reduced due to the reaction of PbI₂ and MAI, compared with the XRD pattern of original triple cation PSK. These results clearly prove the formation of the passivated MAPbI₃ layer from residual PbI₂ on the 3D perovskite layer through MAI treatment on the carbon electrode. In addition, the change of functional groups of perovskite film was confirmed through FT-IR analysis (**Figure 57**). The strong N–H₃⁺/CH₃ rock (911 cm⁻¹) and

C–N stretch (963 cm^{-1}) peaks are typical peaks of MAPbI_3 [164, 165]. In particular, after treatment with MAI, the symmetric NH_3^+ bending peak, the main peak from MA cation-based perovskite at 1470 cm^{-1} , demonstrates the interface formation of MAPbI_3 . SSPL measurements were conducted to confirm the presence of colloidal PbI_2 and secondary growth MAPbI_3 , and to analyze the PL properties, as shown in **Figure 58**. The samples were prepared on a glass substrate to eliminate the quenching effect by TiO_2 , which tends to extract excited electrons. Given the high absorption coefficient of the perovskite layer at an excitation wavelength of 430 nm , the light penetration depth was only about 100 nm [98, 129]. Thus, most charges were generated near the top or bottom surface, depending on the excitation direction. The samples were excited from the glass side or top surface of perovskite film; there was little difference between the two spectra. When excited from the top surface of the perovskite film w/o and with the treatment of PbI_2 and additional MAI, the spectrum exhibited a characteristic PbI_2 peak at 530 nm [166], indicating PbI_2 formation on the top surface. According to MAI treatment, the decreased PL intensity of PbI_2 , indicating that PbI_2 presented on the surface reacts. In addition, the redshift of fluorescence peak occurred from 765 nm to 780 nm and the perovskite fluorescence

intensity increased. This is due to the further growth of the MAPbI₃ layer on the triple cation perovskite layer comprising Cs and Br and the reaction with residual PbI₂ in the GB of triple cation perovskite [124] [161, 167]. Taken together, these results provide convincing evidence for interfacial secondary growth of the MAPbI₃ layer at the triple cation perovskite/carbon interface *via* colloidal PbI₂ treatment and continuous MAI treatment.

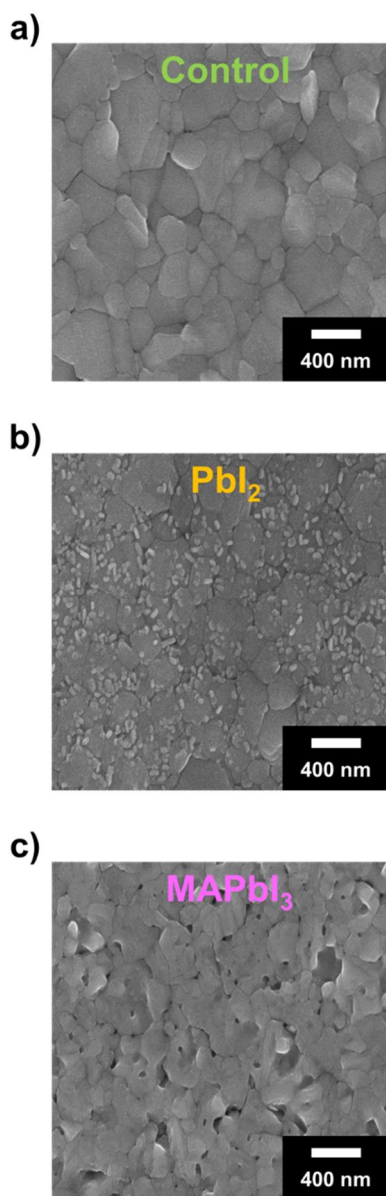


Figure 54. Surficial FE-SEM images showing perovskite films (a) w/o and with (b) colloidal PbI₂ and (c) secondary grown MAPbI₃ interfacial layer.

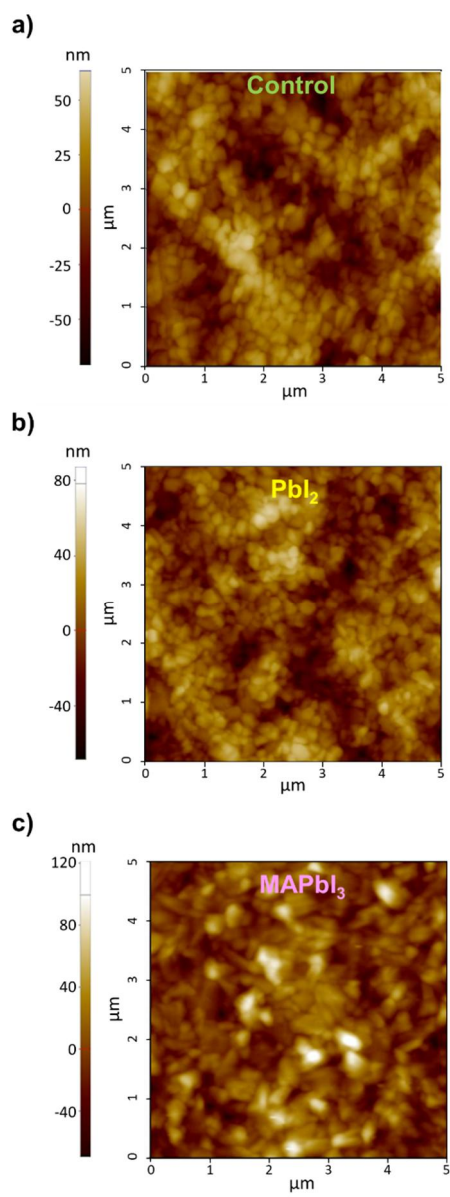


Figure 55. Surficial AFM images indicating perovskite films (a) w/o and with (b) colloidal PbI₂ and (c) secondary grown MAPbI₃ interfacial layer.

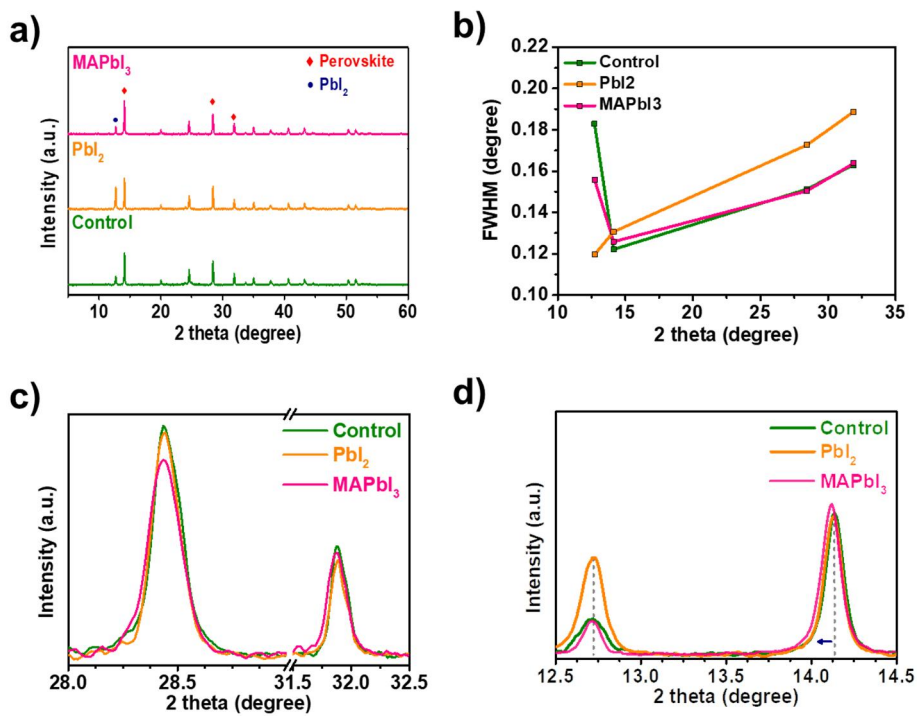


Figure 56. (a) Full and (c, d) expanded range of XRD patterns, including (b) FWHM of specific peaks, of the perovskite films w/o and with colloidal PbI₂ and secondary grown MAPbI₃ interfacial layer.

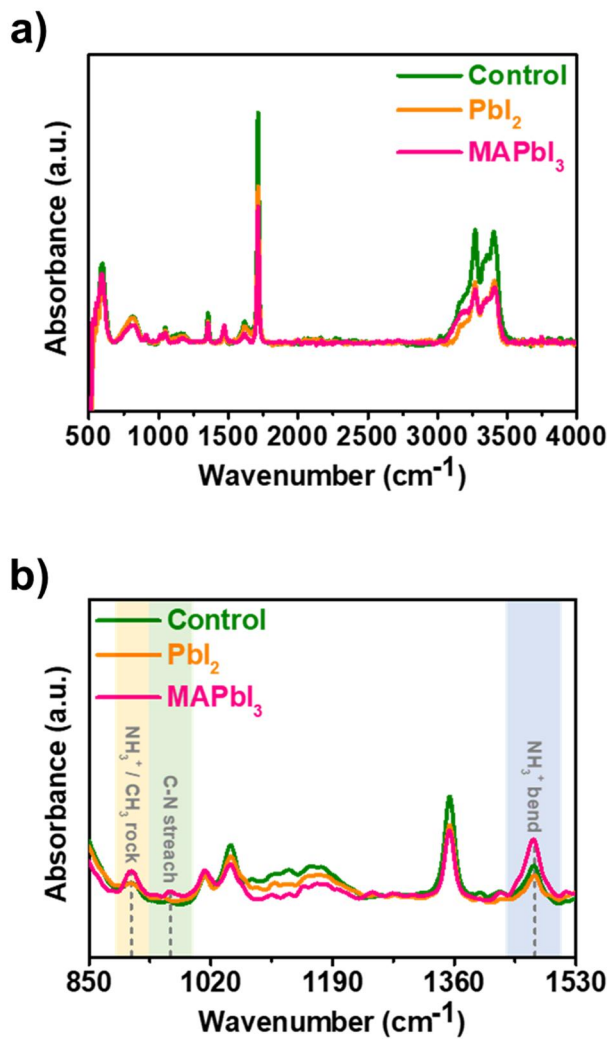


Figure 57. (a) Full range and (b) enlarged range of FT-IR spectra of the perovskite films w/o and with colloidal PbI₂ and secondary growth of MAPbI₃ interfacial layer treatment.

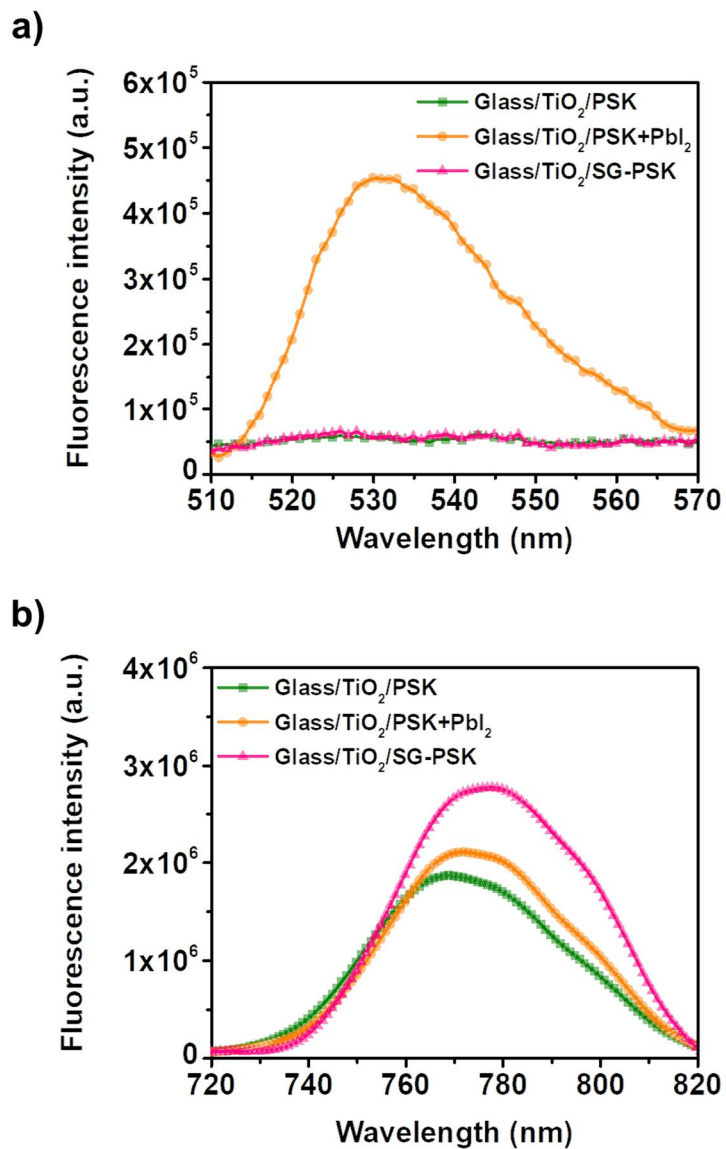


Figure 58. SSPL spectra for (a) fluorescence of PbI_2 and (b) perovskite films w/o and with colloidal PbI_2 and secondary grown MAPbI_3 interfacial layer.

3.2.3. Photovoltaic performance of C-PSCs with MAPbI₃ interfacial layer

The effects of interfacial secondary growth of MAPbI₃ *via* treated-colloidal PbI₂ on the photovoltaic performance of C-PSC were investigated. *J-V* curves for the control (without any post-treatment), PbI₂-treated devices and further MAI-treated devices are described in **Figure 59a**. When only the colloidal PbI₂ solution is treated, overall performance is slightly improved compared to the conventional C-PSC, but the difference is negligible. However, all PV parameters improved dramatically in secondary growth MAPbI₃-based C-PSC. The V_{oc} , which is generally defined as the difference between the lowest unoccupied molecular orbital (LUMO) level of the perovskite and the highest occupied molecular orbital (HOMO) of the HTM, exceeded 1.03 V in MAPbI₃ in C-PSC with MAPbI₃ interfacial layer [168]. There would have been considerable changes in the aligned energy levels due to the introduced interfacial layer between perovskite and carbon electrode. Moreover, the introduced MAPbI₃ interfacial layer effectively passivates the contact and provides optimal charge extraction and significantly improves device performance with improved FF [169].

The obtained photocurrents were in good agreement with the IPCE spectra (**Figure 59b**). The champion efficiency of 16.98% was achieved

with J_{sc} of 22.81 mA cm⁻², V_{oc} of 1.03 V, and FF of 0.72 (**Figure 59c**). This result is the highest efficiency of C-PSC without hole conductors to date [47]. **Figure 59d** exhibits that cell performance was improved according to the alkyl chain length of organic acid in the colloidal PbI₂ solution. If the length of the alkyl chain is too short, the effective colloid formation becomes difficult, and the amount of PbI₂ introduced into C-PSC decreases, resulting in a slight decrease in efficiency. On the other hand, if the chain length is longer, since the organic acid acts as an obstacle for forming perovskite crystals, the efficiency increase is small because the MAPbI₃ interface layer does not grow properly [170, 171].

The average PV parameters achieved from 26 untreated C-PSCs, PbI₂, and MAPbI₃-treated C-PSCs were compared to demonstrate the reliability of this design (**Figure 60, Table 5**). Introduction of MAPbI₃ interfacial layer caused the average J_{sc} to increase from 20.06 to 22.60 mA cm⁻², the V_{oc} to increase from 0.97 to 1.03 V, and FF to increase remarkably from 0.58 to 0.70. In addition, the device performance for a larger active area of 1 cm² was measured. As indicated in **Figure 61**, it exhibited PCE of 11.97% with J_{sc} of 21.41 mA cm⁻², V_{oc} of 1.10 V, and FF of 0.51.

To accurately approve the confidence of performance measured from

secondary growth of MAPbI₃-based C-PSC, and to ensure the extent of device hysteresis, the steady-state photocurrent density and PCE were estimated at maximum power output (0.847 V deduced from reverse scan result) for 100 s in **Figure 62**. The stabilized photocurrent density of MAPbI₃-based C-PSC was 18.73 mA cm⁻² (navy line), corresponding to a power output of 15.87 mW cm⁻² (= PCE of 15.87 %, pink line). The SPO is close to the average value of efficiencies obtained from forward and reverse scan direction, which denotes the performance credibility of MAPbI₃-based C-PSCs.

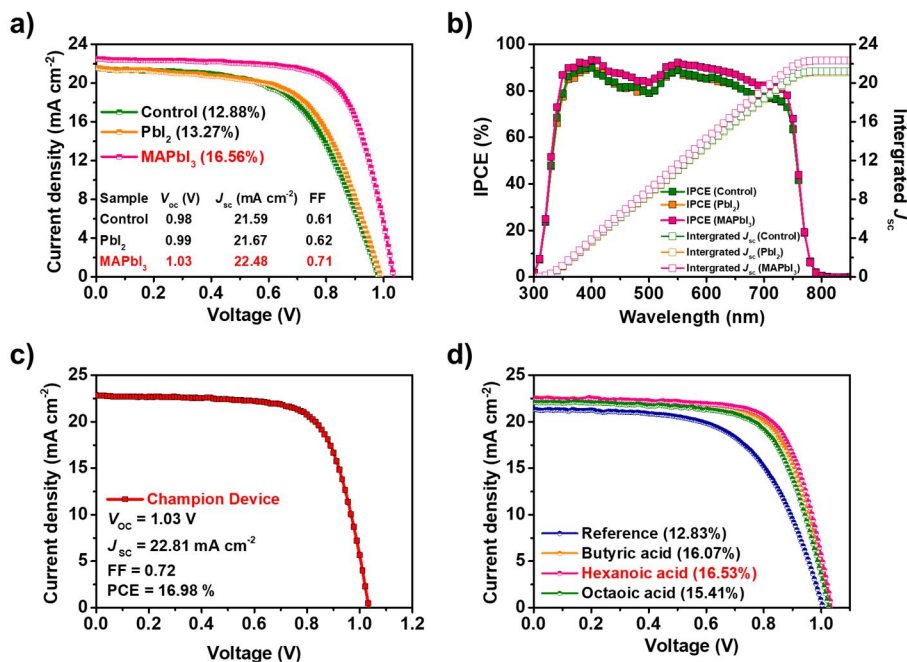


Figure 59. (a) J - V characteristics and (b) IPCE spectra of pristine C-PSC and post-treated C-PSC with colloidal PbI_2 and sequential MAI treatment. (c) Performance data of the champion device. (d) Comparison of J - V characteristics according to the chain length of organic acid.

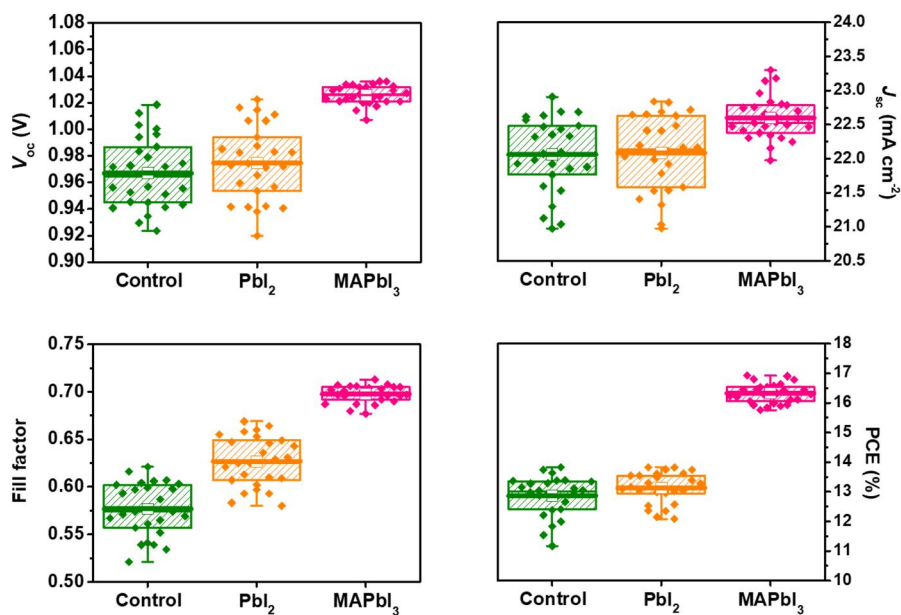


Figure 60. Variation and comparison of the PV parameters such as V_{oc} , J_{sc} , FF, and PCE of the C-PSC w/o and with colloidal PbI₂ and MAI treatment. These parameters were evaluated from 26 devices fabricated for each concentration.

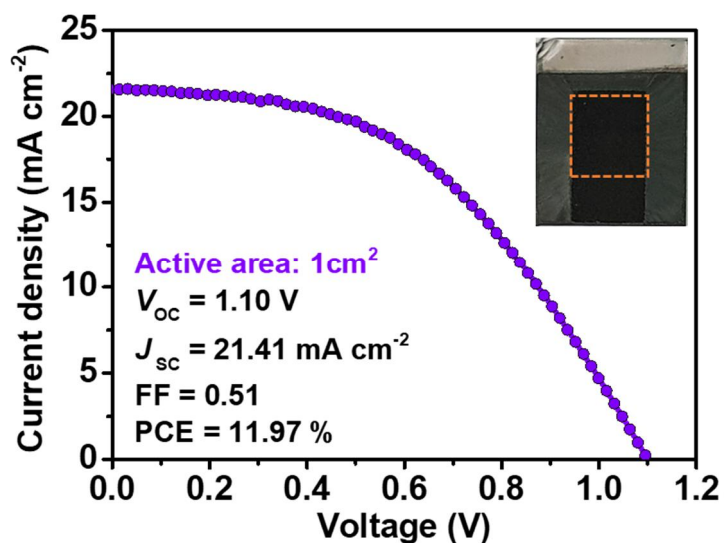


Figure 61. J - V characteristic of the device with an active area of 1 cm². The inset shows a digital photograph of C-PSC with MAPbI₃ interfacial layer and the dashed orange square represents an active area.

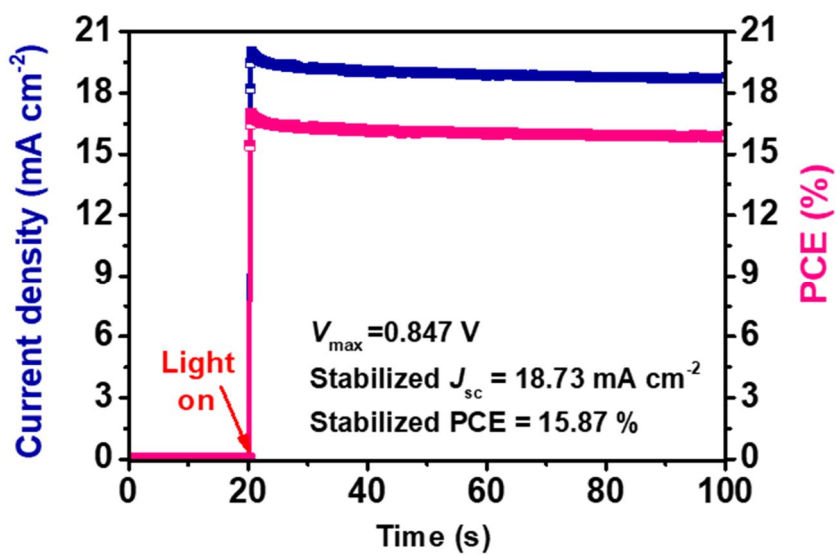


Figure 62. Stabilized photocurrent and PCE of secondary-grown MAPbI₃-based C-PSCs fabricated by optimized condition, measured at the maximum power point (0.847 V) for 100 s.

Table 5. Average PV parameters evaluated from 25 each type devices measured under 100 mW cm^{-2} of simulated AM 1.5G illumination.

Type of substrate	J_{sc} (mA cm^{-2})	V_{oc} (V)	FF	η_{avg} (%)
Control	22.06 ± 0.43	0.97 ± 0.02	0.58 ± 0.02	12.87 ± 0.50
PbI₂	22.08 ± 0.43	0.98 ± 0.02	0.63 ± 0.02	13.13 ± 0.40
MAPbI₃	22.60 ± 0.24	1.03 ± 0.01	0.70 ± 0.01	16.32 ± 0.27

η_{avg} : average power conversion efficiency.

3.2.4. Interfacial charge carrier dynamics in C-PSCs with MAPbI₃ interfacial layer

To address the change in charge carrier (specifically hole) dynamics at the interface perovskite/carbon, SSPL and TRPL analyses, which have been used to reveal the dynamics of charge transfer [135], were performed on glass / TiO₂ / triple cation PSK / carbon electrode samples without and with the treatment of colloidal PbI₂ and sequential MAI, and carbon (for convenience, the untreated triple cation perovskite was named R-PSK, and perovskite with the secondary grown MAPbI₃ interface was termed SG-PSK) (**Figure 63 and 64a**). For PbI₂ or MAPbI₃-treated samples, the PL signals were quickly quenched by increasing the hole extraction and decreasing charge recombination at the interface. When only PbI₂ was treated, PbI₂ present at the interface partially gave a passivation effect and PL quenching became faster, and a more densely packed carbon electrode was formed by the treated non-polar solvent. In particular, the adjusted interfacial energy level according to MAPbI₃ formed by MAI treatment further improved hole extraction ability and suppressed charge recombination. **Figure 64b** shows that charge transfer occurs to TiO₂ in the absence of a carbon electrode and gradual PL decay. When the MAPbI₃ interfacial layer was

introduced, the PL lifetime considerably increased. The formed MAPbI₃ interfacial layer effectively removed trap conditions on the pristine perovskite surface and demonstrated a passivation effect and reduced non-radioactive recombination. The resulting TRPL curves for each sample were fitted using a bi-exponential decay equation and related parameters are summarized in **Table 6**. The fast decay part (A_1, τ_1) is involved in non-radiative recombination and electron transport to the FTO in this experiment and the slow decay part (A_2, τ_2) mirrors the radiative recombination in the bulk perovskite [153]. The PL decay time of the untreated sample with a τ_{avg} of 78.4 ns increased to 129.8 ns for the secondary growth of MAPbI₃-treated sample.

UPS analysis and UV-Vis absorption spectra suggested that improve the performance of C-PSC with respect to adjusting the energy level with the secondary growth of MAPbI₃ interfacial layer, as suggested in **Figure 65 and Table 7**. The Work function (WF) and valence band maximum (VBM) values were obtained from UPS analysis and determined by equation $\Phi = h\omega - |E_{sec} - E_{FE}|$, where $h\omega = 21.22$ eV (He I source), E_{sec} is the onset of the secondary emission, and E_{FE} is the Fermi edge, which is set to 0 eV. UV-Vis spectra were calculated through Tauc plot (using $(F(R)h\nu)^2$ as a function of the photon energy) to obtain optical

bandgap and conduction band minimum (CBM) values. With the introduction of the MAPbI₃ interfacial layer, the energy level gap between the perovskite VBM and the WF of the carbon electrode was reduced to improve hole extraction capability at the interface. In addition, the MAPbI₃ interfacial layer exhibits energy levels higher than the CBM of conventional perovskite and significantly reduces interfacial charge recombination due to the appropriate energy level [172, 173]. At this time, the introduced colloidal PbI₂ exhibits a passivation effect due to a large bandgap and high CBM, so even if only PbI₂ is treated, the interfacial charge recombination is partially suppressed, and device performance is slightly improved [174]. The energy level alignments of the component layers are presented in **Figure 66**.

To assure the hypothesis about the interfacial charge recombination and charge extraction between perovskite and carbon electrode, the EIS was measured from 1 Hz to 1 MHz under full illumination of simulated solar AM1.5 global light at 100 mW cm⁻² with 1.0 V bias (**Figure 67**). The arcs of Nyquist plots recorded in the high-frequency region indicated internal charge transport resistance (R_{ct}) with sheet resistance (R_s) at the interface between intrinsic perovskite and carbon electrode [175]. Small arcs were obtained for the treated-devices with PbI₂ and sequential MAI,

which represented excellent hole transport into carbon electrode. Furthermore, the device with secondary grown-MAPbI₃ interfacial layer exhibited a larger second arc and increased charge recombination resistance (R_{rec}). As all interfaces in the PSCs are constant apart from perovskite/carbon interface, it represents that interfacial recombination at perovskite and carbon reduced by secondary growth of MAPbI₃ interfacial layer. Interfacial MAPbI₃ effectively prevents electron diffusion to the carbon electrode and improves interfacial contact, contributing to remarkable V_{oc} and FF improvement. Furthermore, a change in resistance was confirmed through a difference in the formation of an interfacial layer according to the alkyl chain length of the organic acid used when preparing the colloidal PbI₂ (**Figure 67b**). EIS data parameters are listed in **Table 8**. This EIS results were consistent with the trends in the TRPL data and the PV performances.

To identify the change of hole transporting ability to carbon electrode by secondary growth of MAPbI₃ interfacial layer, the direct current (DC) conductivity and hole mobility were measured from current–voltage (I – V) characteristics of the FTO / PEDOT:PSS / triple cation PSK/ (MAPbI₃) / carbon electrode configuration. In the ohmic region of I – V curve (**Figure 68a**), the DC conductivity (σ_0) of each device was calculated

using the equation ($I = \sigma_0 A d^{-1} V$), where A is the active area and d is the thickness of the HTL [176]. The active area was $7 \times 10^{-4} \text{ cm}^2$ and the thickness of the carbon electrode is 0.1 cm. The electrical conductivity of the untreated C-PSC and PbI_2 treated and sequential MAI treated C-PSC obtained 6.8 S cm^{-1} and 9.8 S cm^{-1} respectively. Also, the increased hole mobility of C-PSC with secondary grown-MAPbI₃ interfacial layer was obtained from a relation of $\sigma_0 = ne\mu_0$ and the Mott–Gurney law: $J = (9/8)\mu\epsilon_0\epsilon(V^2/d^3)$; where n , e , μ , ϵ_0 , ϵ , and d are the hole density, elementary charge, charge mobility, free space permittivity, relative dielectric constant, and film thickness, respectively. Furthermore, the current density increases linearly and nonlinearly with voltages in **Figure 68b**, and the voltage at the kink point is determined the trap-filled limit voltage (V_{TFL}), which determines the trap state density (n_{trap}) on the basis of the following equation: $n_{\text{trap}} = 2\epsilon\epsilon_0 V_{\text{TFL}}/eL^2$ [177]. The dielectric constant of perovskite film is $\epsilon = 46.9$ and each value came from previous studies [178]. The n_{trap} decreases from $5.50 \times 10^{16} \text{ cm}^{-3}$ for the untreated device to $2.28 \times 10^{16} \text{ cm}^{-3}$ for secondary growth of MAPbI₃ interfacial layer on the device, respectively, indicating that the introduction of MAPbI₃ interfacial layer effectively heals the defect in the interface between perovskite and carbon electrode. **Figure 69** shows a C-AFM

image under a bias voltage of 1V and increased surface currents were observed in the PbI_2 treated and additional MAI treated samples. Brighter contrast indicates more conduction current flow through the perovskite layer [179]. More increased surface currents were observed in the PbI_2 treated and additional MAI treated samples. Moreover, blurred GB indicated brighter contrast demonstrates that the current more efficiently was carried on the GB.

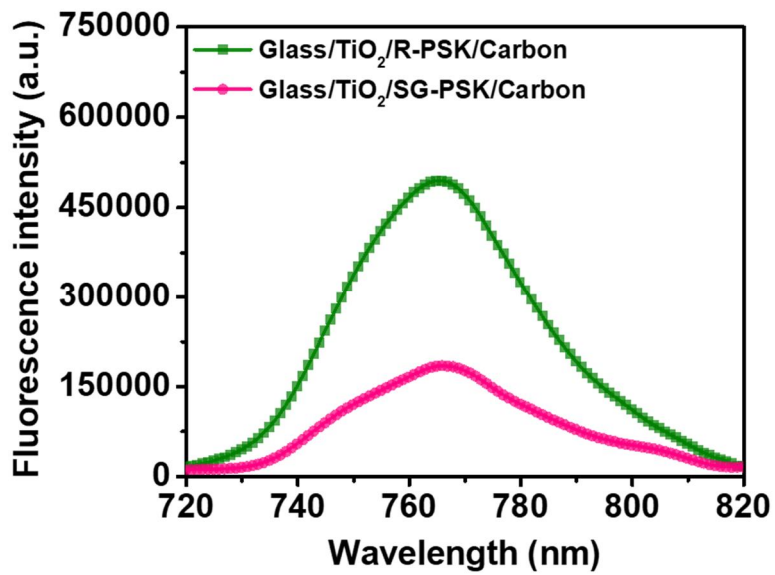


Figure 63. SSPL decay curve according to the introduction of MAPbI₃ interfacial layer (excitation wavelength: 420 nm).

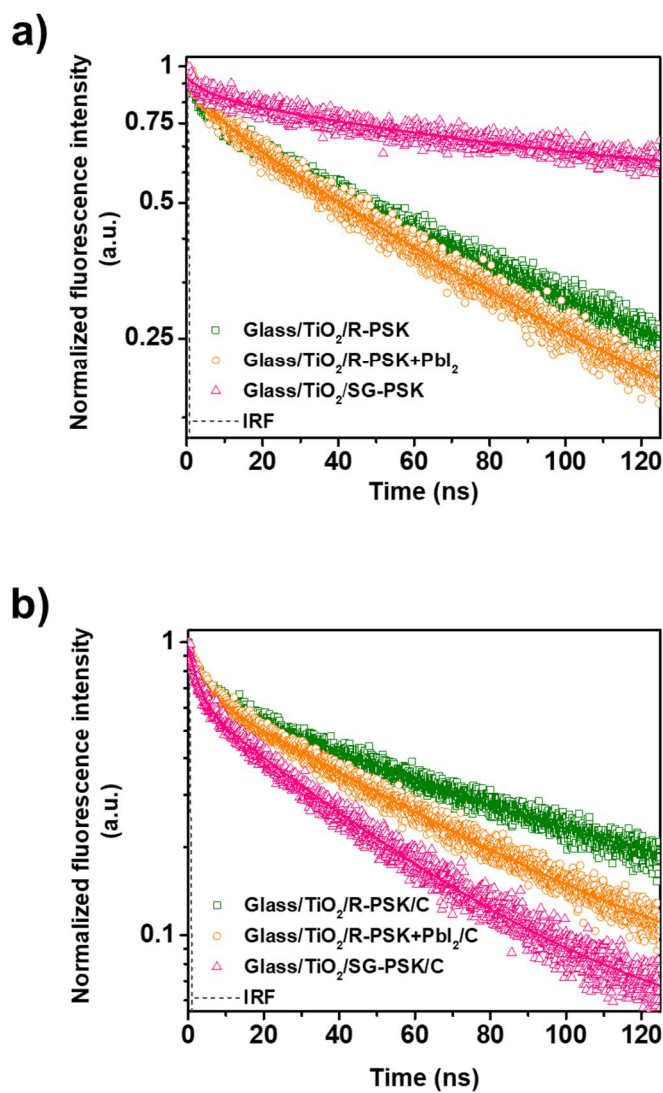


Figure 64. TRPL decay curves extracted from untreated and treated-samples (a) w/o and (b) with carbon electrode. TRPL spectra were recorded under exposure to 520 nm pulse laser.

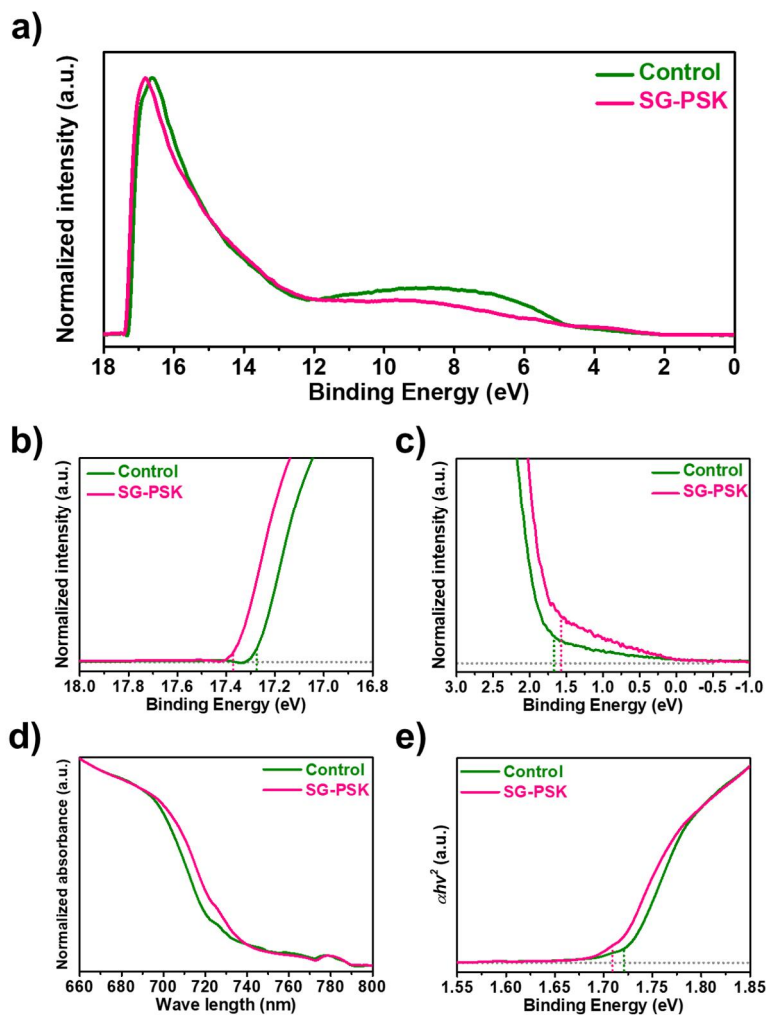


Figure 65. (a) Overall UPS spectra of control and SG-PSK based on C-PSCs; (b) and (c) the expanded spectra at secondary electron cutoff and Fermi-edge regions, respectively. (d) UV-vis absorption spectra of pristine triple cation perovskite and secondary-grown perovskite film. (e) Optical band gap energy determination *via* Tauc plot analysis.

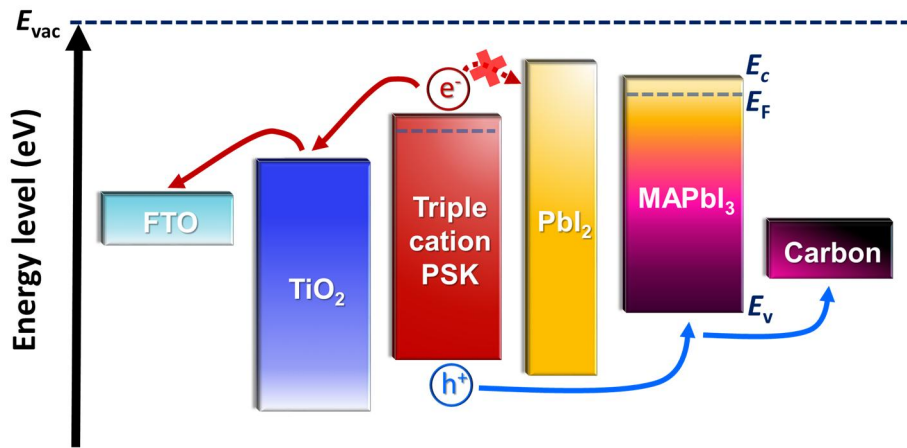


Figure 66. Energy level diagram of the component layers in the C-PSC with the introduction of colloidal PbI₂ and MAPbI₃ interfacial layer.

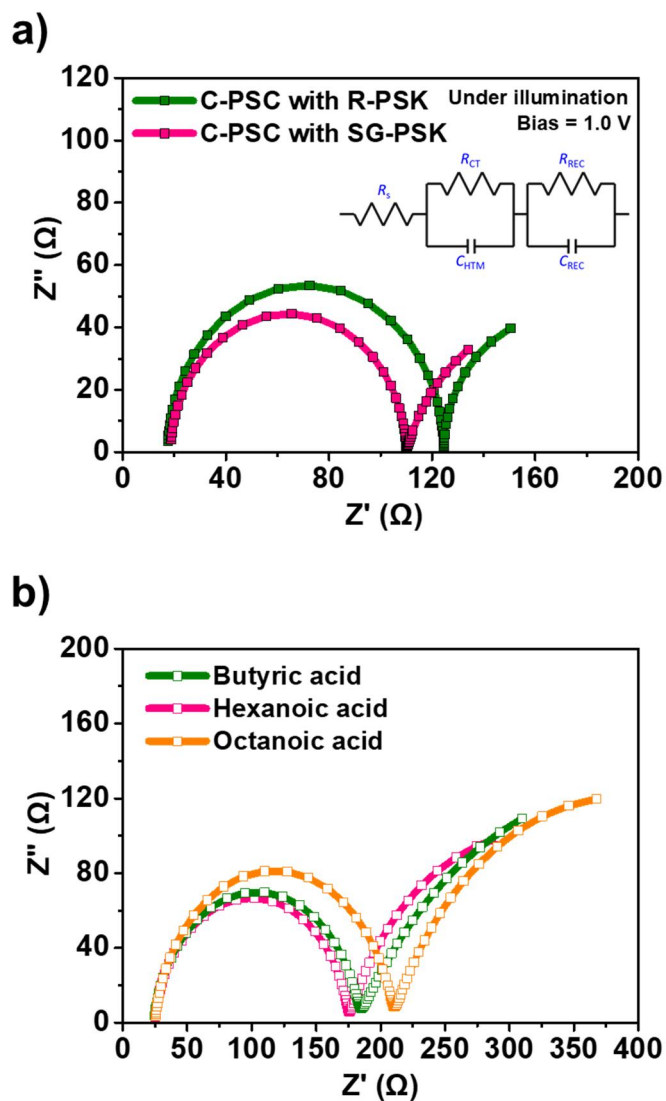


Figure 67. Nyquist plots of the C-PSCs (a) without treatment and with secondary grown-MAPbI₃ interfacial layer, and (b) with the treatment of adjusted alkyl chain length of organic acid in colloidal PbI₂ solution, which are measured under illumination at 1.0 V bias.

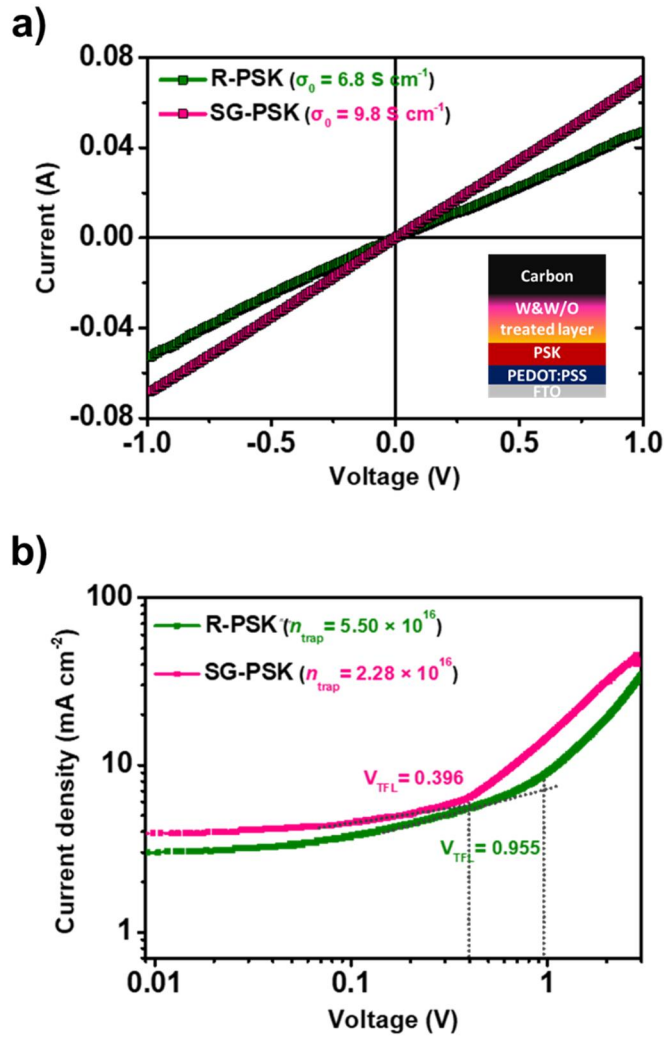


Figure 68. (a) J - V characteristics for hole only devices based on FTO / PEDOT:PSS / triple cation PSK / (MAPbI₃) / carbon electrode structure (inset) and the calculated electrical conductivity (σ_0). (b) The SCLC region of dark current–voltage (J_d - V) characteristics for controlled hole only devices with V_{TFL} kink point and the n_{trap} .

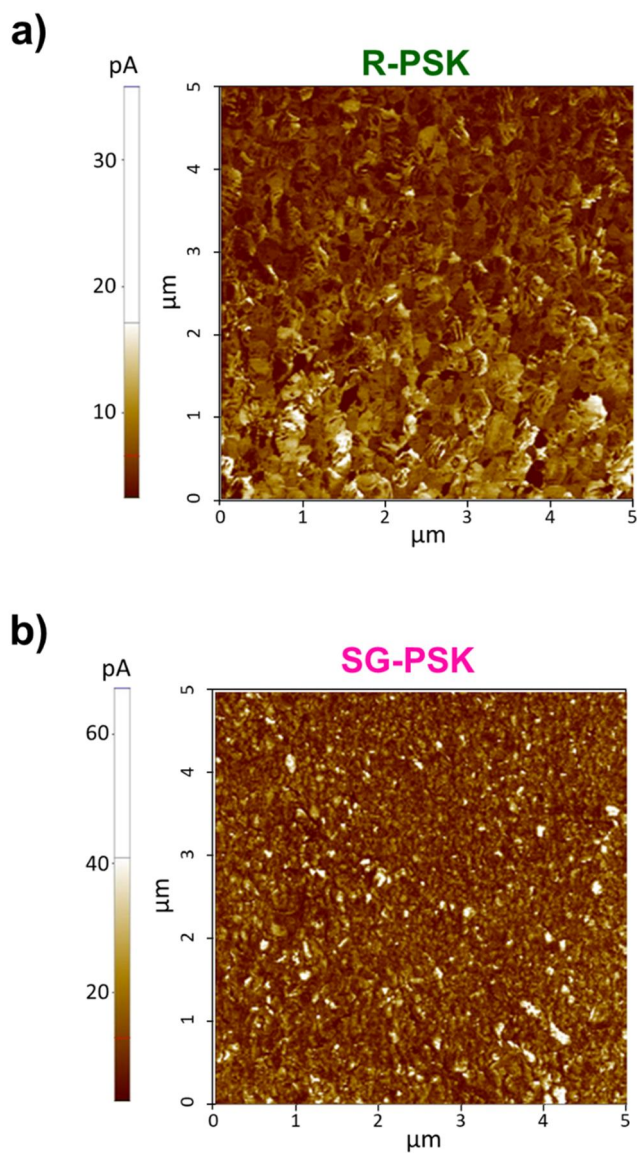


Figure 69. C-AFM current mapping images of perovskite films (a) w/o and with (b) secondary grown-MAPbI₃ interfacial layer treatment under room light condition with a bias of 1.0 V, respectively.

Table 6. TRPL decay parameters for the perovskite films w/o and with PbI₂ and additional MAI treatment. The bi-exponential decay equation was used for fitting the curves.

Sample	τ_1 (ns)	τ_2 (ns)	^{a)} τ_{avg} (ns)	A ₁	A ₂
Glass/TiO₂/R-PSK	3.2	79.1	78.4	19.5	80.5
Glass/TiO₂/R-PSK+PbI₂	3.9	75.8	75.0	17.9	82.1
Glass/TiO₂/SG-PSK	4.5	130.4	129.8	11.8	88.2
Glass/TiO₂/ R-PSK/Carbon	3.0	65.7	64.5	29.0	71.0
Glass/TiO₂/ R-PSK+PbI₂/Carbon	3.8	54.7	53.3	28.8	71.2
Glass/TiO₂/ SG-PSK/Carbon	3.0	40.7	39.2	36.1	63.9

$$^a)\tau_{avg} = \sum_i A_i \tau_i^2 / \sum_i A_i \tau_i$$

Table 7. Comparison of parameters related to energy level of C-PSC w/o and with MAPbI₃ interfacial layer.

Samples	E_{SEC}	^aWF	VBM	Bandgap
R-PSK	17.28	3.94	5.61	1.72
SG-PSK	17.37	3.85	5.42	1.71

^a)E_f = 0 eV

Table 8. EIS parameters of the C-PSCs w/o and with secondary grown-MAPbI₃ interfacial layer, obtained by fitting the Nyquist plots. Note that the alkyl chain length of colloidal PbI₂ was controlled butyric acid to octanoic acid.

Samples	R_s (Ω)	R_{ct} (Ω)	R_{rec} (Ω)
C-PSC with R-PSK	17.5	119.5	53.6
C-PSC with MAPbI₃	18.4	86.8	60.2
Butyric acid-based PbI₂	24.3	158.6	357.6
Hexanoic acid-based PbI₂	24.9	150.3	431.8
Octanoic acid-based PbI₂	29.6	184.5	293.9

3.2.5. Device hysteresis and long-term stability of C-PSCs with MAPbI₃ interfacial layer

To confirm the manufacturing uniformity of the C-PSC device with and without the introduction of the MAPbI₃ interfacial layer, a histogram of the efficiency of 30 samples was obtained (**Figure 70a**). The average power conversion efficiency (PCE_{avg}) of the devices obtained from 30 samples was 12.93% and 16.30%, depending on the presence or absence of the MAPbI₃ interfacial layer, respectively. These results showed an average 26% improvement in device efficiency and overall stability of the interfacial introduction process. The hysteretic behaviors of the C-PSCs were also evaluated using the PSCs fabricated by the introduction of MAPbI₃ interfacial layer (**Figure 70b and Table 9**). The ratio of forward-scan PCE and reverse scan PCE is about 0.86, and the difference is reduced compared to the ratio value of C-PSC without MAPbI₃ interfacial layer, which is a low-level hysteresis conductor considering the absence of holes.

The durability C-PSCs w/o and with PbI₂ and MAPbI₃ treatment in an ambient environment was tested without encapsulation (**Figure 71**). The PCE of C-PSC without treatment had a slightly lower 91% of initial performance over a month with high ambient stability. This is because

the carbon electrode-based PSC has no instability in the deterioration of the metal electrode at the interface, and the hydrophobic carbon electrode protects the perovskite layer. On the other hand, in the case of C-PSC treated only with colloidal PbI_2 , the efficiency gradually decreased after a certain period and maintained at 78% of the initial efficiency after 1 month. This is because PbI_2 present at the interface promotes perovskite degradation [180]. However, despite the presence of PbI_2 at the interface, the reason that the long-term efficiency did not decrease significantly is because of the protective effect of the colloidal PbI_2 by the hydrophobic organic acid [181-183]. Surprisingly, in the case of C-PSC in which the secondary growth of MAPbI_3 interfacial layer was introduced through MAI treatment, 96% of the initial efficiency was maintained even after 750 h, and the interfacial layer was shown to function properly as a passivation layer [184].

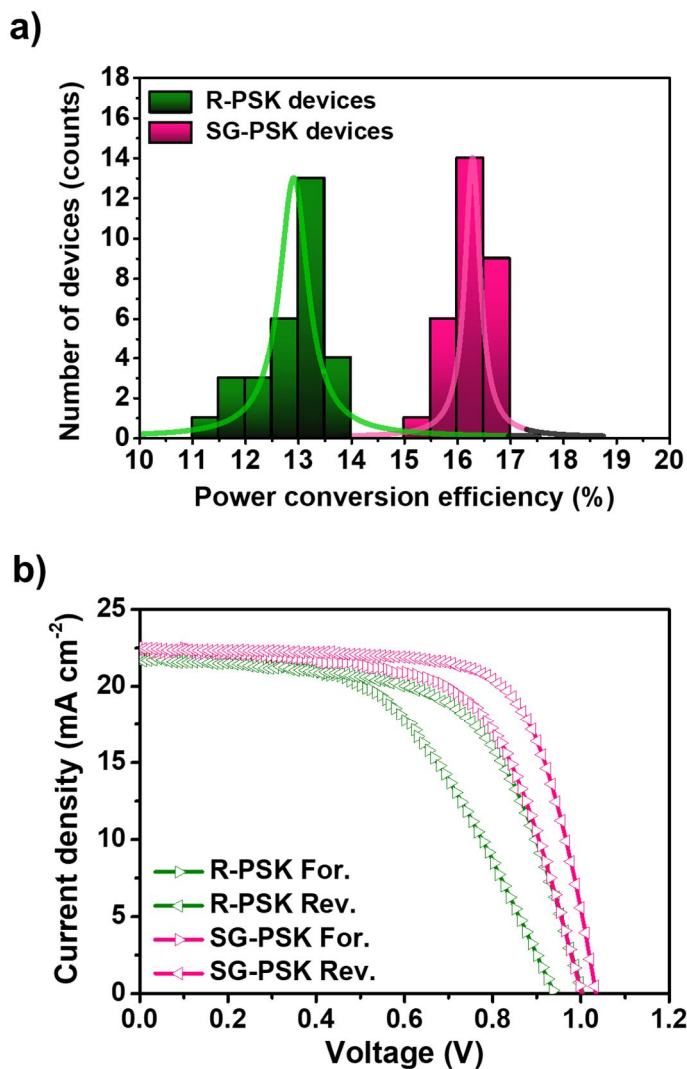


Figure 70. (a) Histogram of the PCE values obtained from 30 C-PSC w/o ($PCE_{avg} = 12.93\%$) and with secondary growth of $MAPbI_3$ interfacial layer ($PCE_{avg} = 16.30\%$). (b) $J-V$ curves of each type of PSC measured by forward and reverse scans where the hysteresis was alleviated by the introduction of $MAPbI_3$ interfacial layer.

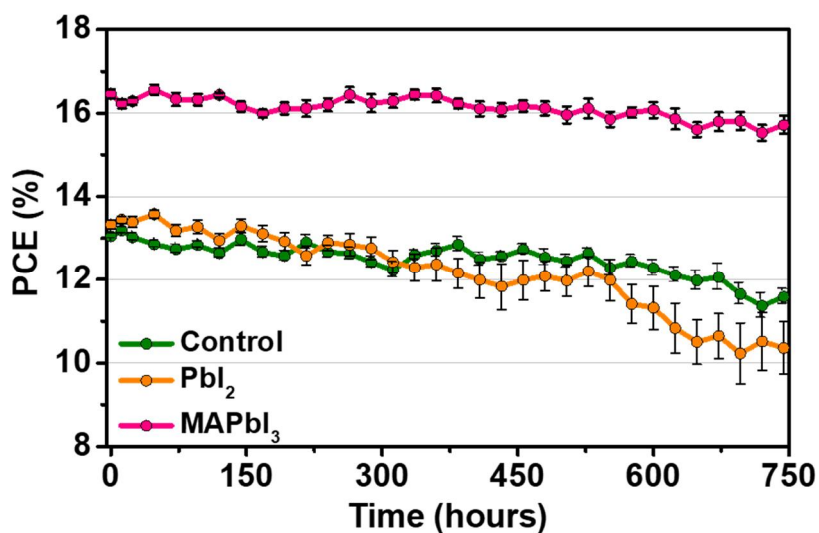


Figure 71. Normalized PCE evolution of C-PSC w/o and with treatment PbI₂ and sequential MAI for secondary growth of MAPbI₃ interfacial layer, stored in the controlled ambient conditions (temperature = 25 °C, relative humidity = 40 ± 5%).

Table 9. PV parameters of C-PSC w/o and with secondary growth of MAPbI₃ interfacial layer as a function of scan direction.

Device	Scan direction	J_{sc} (mA cm⁻²)	V_{oc} (V)	FF	PCE (%)
R-PSK	Forward	22.14	0.94	0.52	10.82
	Reverse	21.74	1.00	0.61	13.26
SG-PSK	Forward	22.55	1.00	0.63	14.21
	Reverse	22.47	1.03	0.71	16.43

3.3. Interface engineering of C-PSCs based on energy level adjustment *via* F-plasma treatment

3.3.1. Fabrication of F-doped C-PSCs

Figure 72 represents a schematic diagram of the process used for the fabrication of carbon electrode and F-doping on the carbon electrode. Briefly, compact TiO₂, mesoporous TiO₂, and perovskite layers were prepared using a general two-step method, and then the carbon layer was applied by the screen-printing method without the hole-transporting materials. F-doped carbon electrode-based PSC (FC-PSC) was prepared by C₄F₈ vacuum plasma treatment on the fabricated carbon electrode-based PSC (C-PSC). To confirm the change in the F-doped carbon, X-ray photoelectron spectroscopy (XPS), FT-IR spectroscopy, and Raman spectroscopy analysis were used to investigate an elemental composition and structural characteristics of FC-PSC. For FC-PSC, the intensity of the C1s (286 eV) and O1s (534 eV) peaks decreased, while the intensity of the F1s (689 eV) peak increased significantly compared to C-PSC (**Figure 73**). Fluorine atoms were introduced to form various C–F_x (x = 1 – 3, 288 – 294 eV) through covalent bonds with the carbon atoms that comprise the carbon electrode, as shown in **Figure 74**. Particularly in the formation of C-F_x groups, F atoms are introduced to a large number of

oxygen defects present in the carbon electrode composed of carbon and oxygen atoms (**Table 10**) [185]. In addition, the change of functional groups on the carbon electrode was confirmed through FT-IR analysis. The strong O–H stretch peak ($3200 - 3600 \text{ cm}^{-1}$), C=O stretch peak, C–O stretch peak and carboxylic O–H bend peak ($1350 - 1700 \text{ cm}^{-1}$) intensities of the existing carbon electrodes decreased after the F plasma treatment, and the broad C–F stretch peak ($1000 - 1300 \text{ cm}^{-1}$) and the C–F stretch peak intensity of 1263 cm^{-1} were clearly observed (**Figure 75a**). Also, in the Raman spectrum, the D / G peak intensity ratio increased in F-treated cells ($I_D / I_G = 0.90$) compared to untreated cells ($I_D / I_G = 0.87$) and indicated peak shifts and decreases of the 2D peak. The doping of F atoms in the graphite carbon multilayer proved an increase in surface defects and bond disorder (**Figure 75b and Table 11**) [186]. As displayed in **Figure 77**, the F atoms were introduced to the surface of the carbon electrode as well as penetrated through meso-sized interstices present in stacked carbon layers and existed in a gradient distribution up to the interface with the perovskite. These results indicated that F atoms were well doped both on the surface and inside of the carbon electrode.

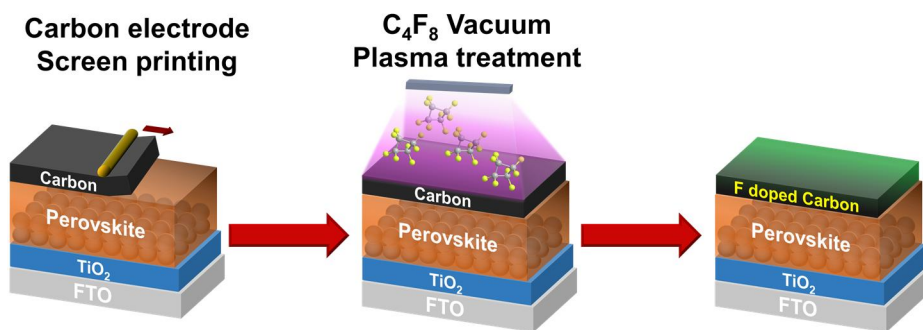


Figure 72. Schematic illustration of the FC-PSC fabrication process.

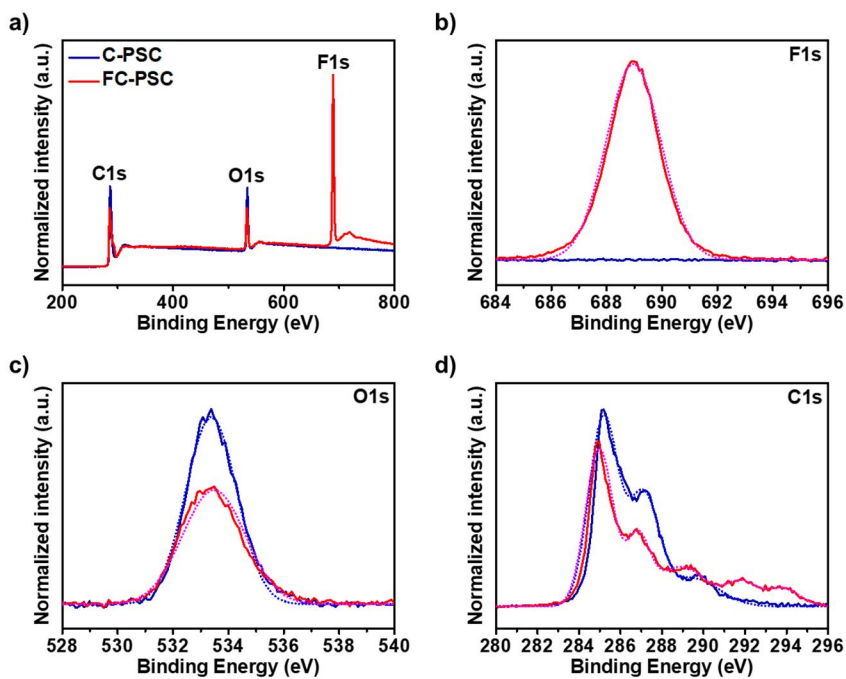


Figure 73. XPS spectra of a carbon electrode and F-doped carbon electrode. (a) XPS survey spectra. (b), (c), and (d) F1s, O1s, and C1s XPS spectra, respectively.

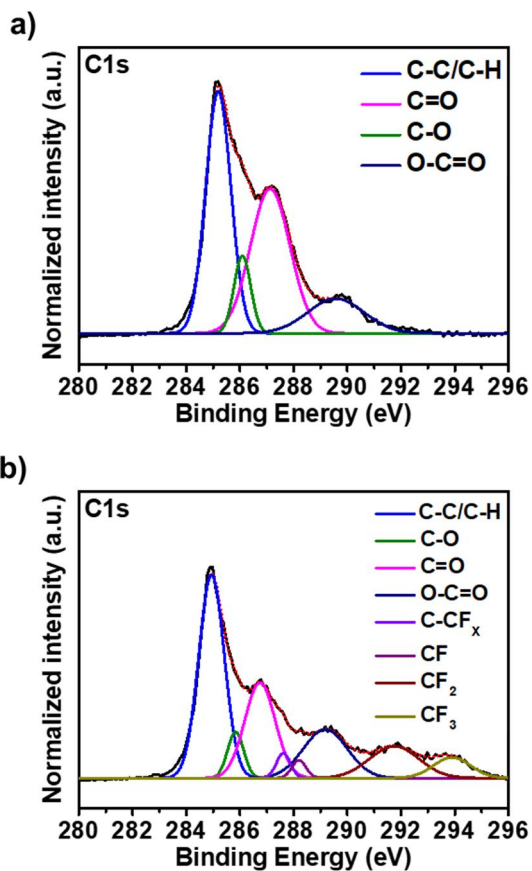


Figure 74. XPS spectra exhibiting deconvolution curves of C1s (a) without F plasma treatment and (b) with F plasma treatment, respectively.

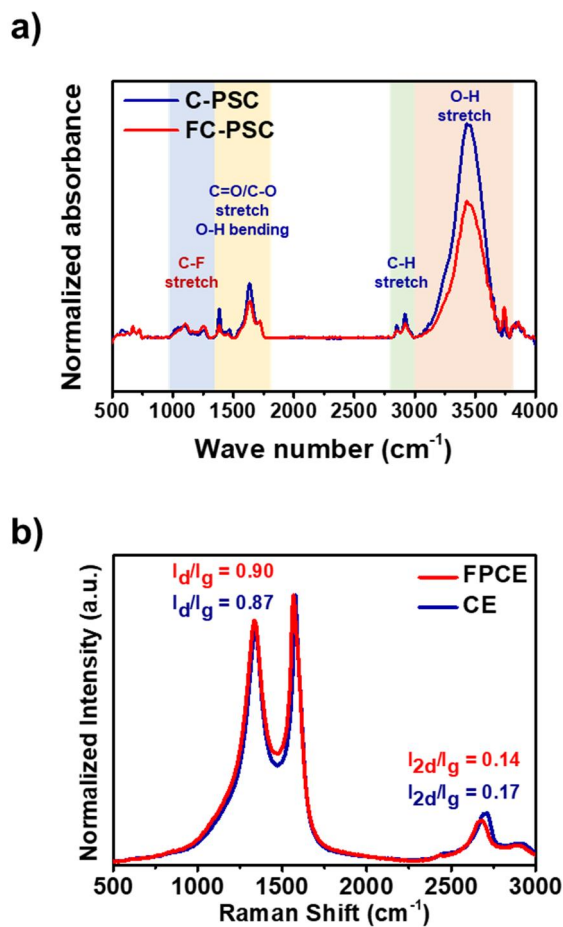


Figure 75. (a) FT-IR spectra of C-PSC w/o and with F plasma treatment. (b) Raman spectra and calculated intensity ratio of C-PSC and FC-PSC.

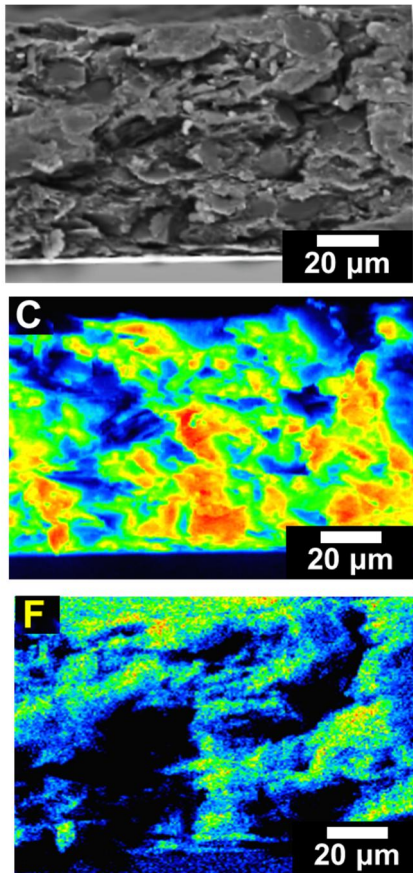


Figure 76. BSE image and FE-EPMA elemental mapping of carbon (C) and fluorine (F) atom in a cross-section of fluorine-doped carbon electrode.

Table 10. Elemental composition of the carbon electrode w/o and with F plasma treatment.

Sample	XPS (at %)					
	C	O	F	F/C Ratio	O/C Ratio	F/O Ratio
C-PSC	80.06	19.94	-	-	0.25	-
FC-PSC	57.97	11.07	30.96	0.53	0.19	2.80

Table 11. Raman spectra peak positions and intensity ratio.

Sample	Assignment	Raman shift (cm⁻¹)	FWHM
C-PSC	D	1342.66	226.63
	G	1577.94	94.81
	2D	2701.27	122.77
FC-PSC	D	1334.95	235.08
	G	1566.36	98.62
	2D	2675.11	114.53

3.3.2. Photovoltaic performance of the F-doped C-PSCs

The photovoltaic performance of C-PSC and FC-PSC was evaluated. $J-V$ characteristics of FC-PSC and C-PSC were measured for the active layer measuring 0.132 cm^2 under the illumination of AM 1.5 G, 100 mW cm^{-2} and presented in **Figure 77**; the hysteresis behavior of the PSC along the scan direction in the $J-V$ curve was also evaluated and the results are summarized in **Figure 78a** and **Table 12**. In the case of a carbon electrode PSC, it is difficult to manufacture a PSC having high FF due to poor contact at the interface between the perovskite and the carbon electrode. However, F plasma treatment led to better contact between the perovskite and the carbon electrode. Thereby, after F plasma treatment, the PCE increased by about 20% (from 11.76% up to 14.70%), and the FF was noticeably improved from 0.58 to 0.69. The relevant analyses are described in detail later.

The PCE distribution histograms were conformed from 40 C-PSCs and FC-PSCs, respectively, as shown in **Figure 78b**. The average PCE of the C-PSC and FC-PSC was 11.89% and 14.07%, respectively. **Figure 78c**, the stabilized V_{oc} for the C-PSC and FC-PSC were 0.96 V and 1.01 V, and the stabilized PCE of the device was 12.86% and 14.02%, respectively. It was confirmed that the FC-PSC has a relatively high V_{oc}

and PCE, and stably operates under light irradiation conditions. IPCE spectra, exhibited in **Figure 78d**, represent a slight enhancement of J_{sc} by F plasma treatment. The spectrum of the FPCE manifested a high EQE close to 90% in a range of 450 – 750 nm, in which the integrated J_{sc} of C-PSC and FC-PSC were 20.23 and 20.85 mA cm⁻², respectively. The rise of PV parameters (FF, V_{oc} , and J_{sc}) was attributed to the energy level alignment at the interface of the carbon electrode to the perovskite layer and improved hole extraction properties. The J – V characteristics of the highest performing device with F plasma treatment are indicated in **Figure 79** and **Table 13**; this device exhibited a PCE of 14.86% with J_{sc} of 22.20 mA cm⁻², V_{oc} of 1.03 V and FF of 0.65. Moreover, the device performance was measured on larger active areas (1 cm²). As revealed in **Figure 80**, the device has a PCE of 9.63% with J_{sc} of 22.83 mA cm⁻², V_{oc} of 0.98 V, and FF of 0.43.

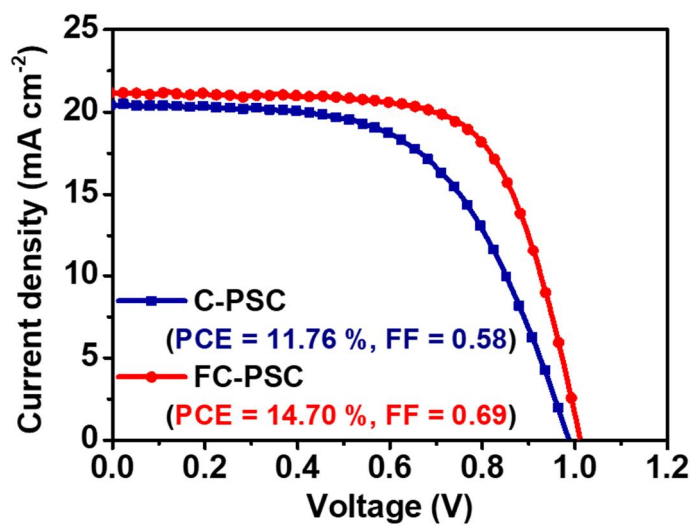


Figure 77. J - V characteristics of PSCs w/o and with F plasma treatment.

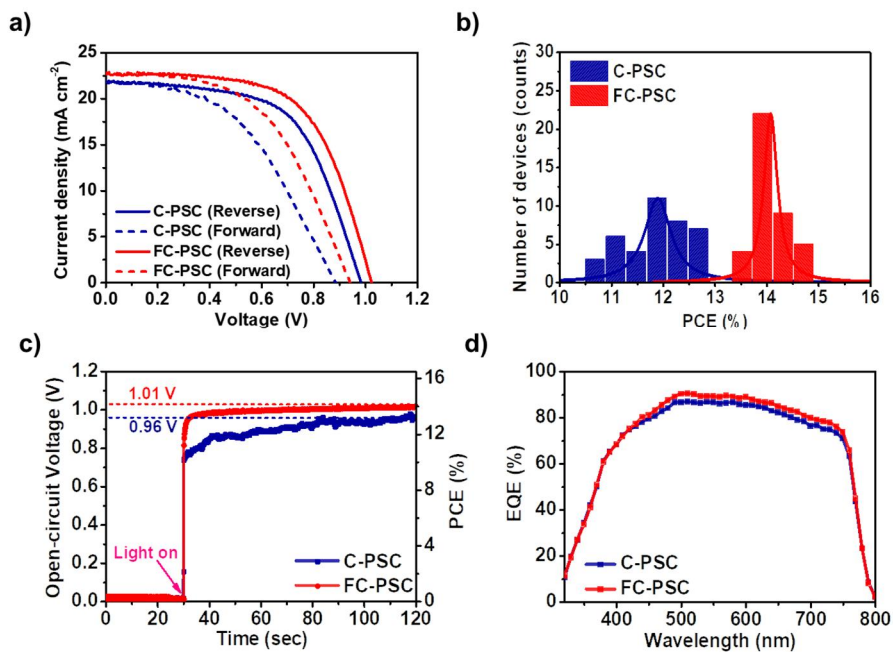


Figure 78. (a) $J-V$ characteristics of carbon-based PSCs w/o and with F plasma treatment as a function of scan direction. (b) PCE distribution for 40 C-PSC and FC-PSC devices, respectively. (c) Stabilized V_{oc} and PCE of each device. (d) IPCE spectra for C-PSC and FC-PSC.

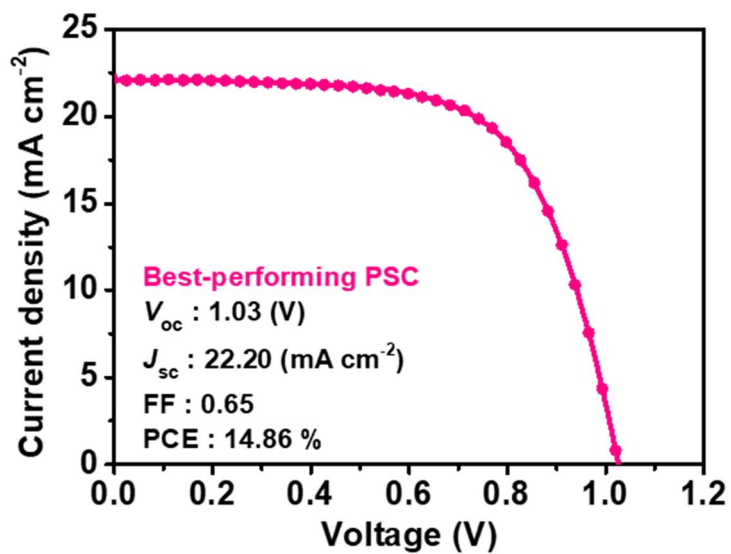


Figure 79. J - V characteristics of the best-performing device (active layer size: 0.132 cm^2).

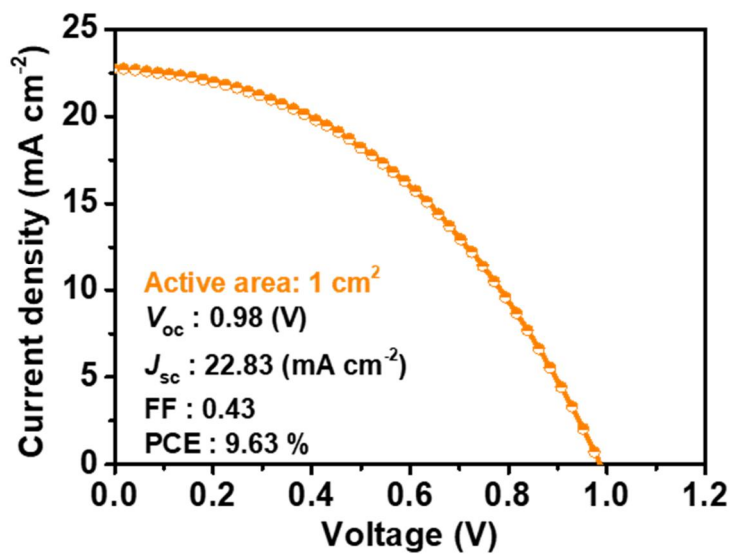


Figure 80. J - V characteristics of the device with an active area of 1 cm^2 .

Table 12. PV parameters of C-PSC w/o and with F plasma treatment according to scan direction.

Device	Scan direction	V_{oc} (V)	J_{sc} (mA cm ⁻²)	FF	PCE (%)
C-PSC	Forward	0.89	21.81	0.45	8.77
	Reverse	0.98	21.90	0.58	12.50
FC-PSC	Forward	0.94	22.78	0.50	10.81
	Reverse	1.02	22.66	0.60	13.97

Table 13. PV parameters of best performing C-PSC with F plasma treatment, compared with average of 40 FC-PSCs.

Sample type	V_{oc} (V)	J_{sc} (mA cm⁻²)	FF	PCE (%)
Champion	1.03	22.20	0.65	14.86
Average	1.02 ± 9.79	21.38 ± 0.50	0.65 ± 0.015	14.07 ± 0.33

3.3.3. Interfacial charge carrier dynamics in F-doped C-PSCs

The contributing factors to the improvement of the PV characteristics were analyzed based on interfacial charge carrier dynamics between the carbon electrode and the perovskite layer. First, the WF of the carbon electrode w/o and with F plasma treatment was confirmed by UPS analysis (**Figure 81a**). The WF of the carbon electrode increased from 4.86 eV to 5.78 eV after F plasma treatment as a secondary electron cut-off edge change, as described in **Figure 81b**. The work function of the F-doped carbon electrode on the surface of the carbon electrode is significantly different from that of the perovskite band edge (5.3 – 5.4 eV). However, as described above, the gradient F doping concentration induced the slope of the energy level on the carbon electrode. Thus, the WF of the F plasma-treated carbon electrode is well aligned with the perovskite valence band edge at the perovskite/carbon interface, thereby improving the hole extraction ability. A schematic energy diagram for this is illustrated in **Figure 82**.

To verify the hypothesis, a TRPL decay rate change was verified. The PL decay curve was fitted with a bi-exponential decay function. The fitted parameters are listed in **Table 14**. The decay curves of samples with and without F plasma treatment were shown in **Figure 83a**. The τ_{avg}

decreased from 77.6 to 34.5 ns by F plasma treatment, and this drastically quenched PL lifetime is due to more efficient hole injection to carbon electrode via the favorable alignment of energy bands. Additionally, EIS measurements were performed to further characterize the interface charge transport properties of the devices. **Figure 83b** presents Nyquist plots in the frequency range from 1 MHz to 1 Hz under 1 sun illumination. High-frequency arcs generally correspond to the charge transport process at the HTM or HTM/electrode interface. But in the device, it corresponds to the hole transport process of perovskite/carbon interface [126, 141]. The reduced R_{ct} of the F plasma-treated device indicates less resistive energy loss (97.45 to 86.27 $\Omega \text{ cm}^2$) during charge transport through the perovskite/carbon interface and in the carbon electrode. Also, the improved interface contact-induced fewer series resistance (R_s) loss. This characteristic change led to a higher FF in the F plasma-treated device, which was consistent with measured $J-V$ characteristics [187]. The results were fitted using an equivalent circuit model (inset in **Figure 83b**) and the fitted parameters are summarized in **Table 15**. In this case, the resistance of the FC-PSC was slightly reduced, but the performance improvement of the device was more affected by the interface contact enhancement, as described in **Figure 84**.

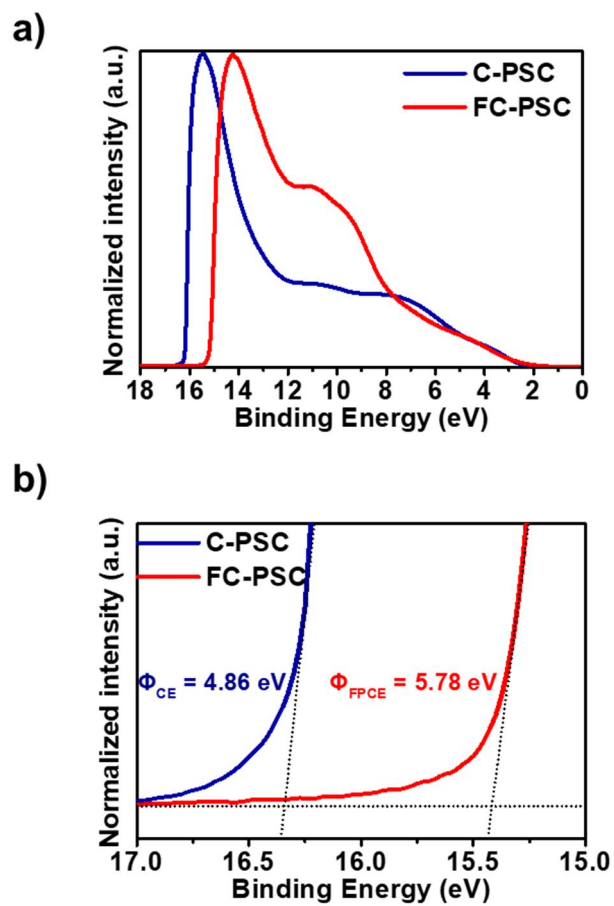


Figure 81. (a) Whole UPS spectra, and (b) magnified view of the secondary electron cut-off region of w/o and with F plasma-treated cell.

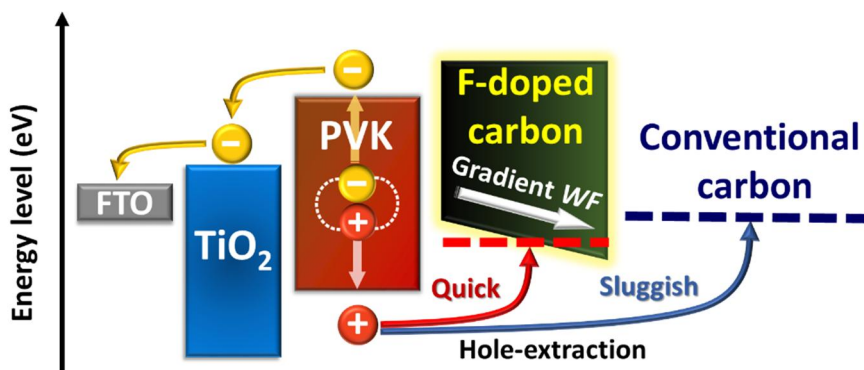


Figure 82. Energy band diagram of each component in the fabricated C-PSC w/o and with F-plasma treatment, showing the separation and transport of photo-generated carriers.

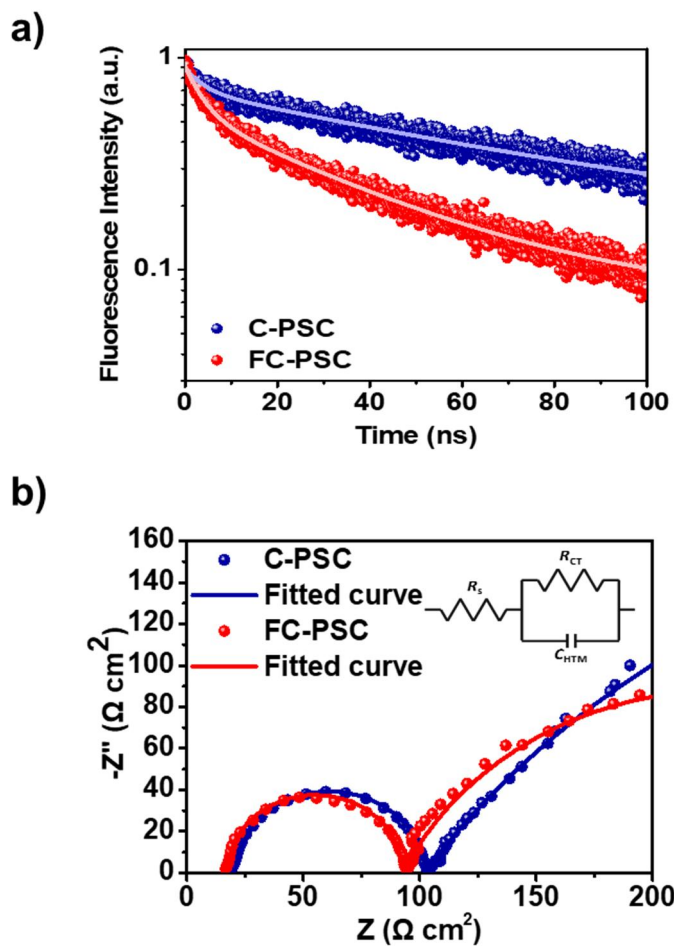


Figure 83. (a) TRPL decay curve for C-PSC and FC-PSC sample. (b) Nyquist plots of C-PSC and FC-PSC devices (inset: the equivalent circuit diagram).

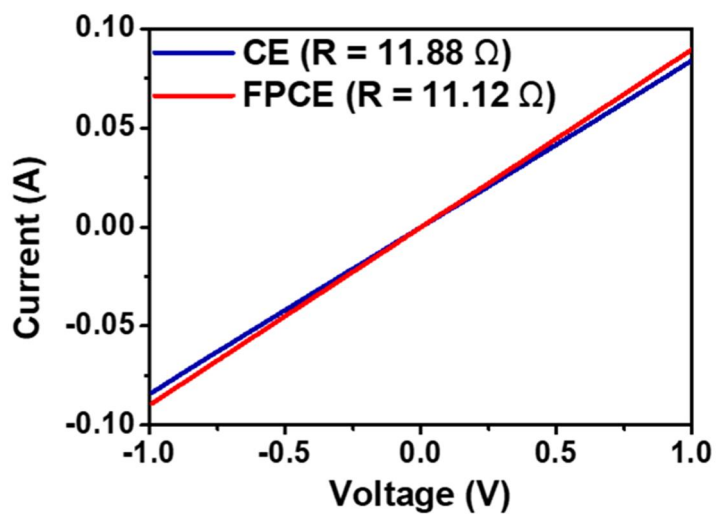


Figure 84. *I-V* curves of the carbon electrode without and with F plasma treatment (CE: Carbon electrode, FPCE: Fluorine plasma-treated carbon electrode).

Table 14. TRPL decay parameters for the perovskite films w/o and with F plasma treatment on the carbon electrode. The curves were fitted with the bi-exponential decay equation.

Samples	τ_1 (ns)	τ_2 (ns)	^{a)} τ_{avg} (ns)	A1	A2
Glass / TiO ₂ / Perovskite / carbon electrode	3.98	78.32	77.62	0.11	0.56
Glass / TiO ₂ / Perovskite / F-doped carbon electrode	3.97	37.34	34.51	0.43	0.49

$$^{\text{a)}} \tau_{\text{avg}} = \frac{\sum_i A_i \tau_i^2}{\sum_i A_i \tau_i}$$

Table 15. EIS results of w/o and with F plasma treatment on the carbon-based PSC.

Device	R_s (Ω)	R_{ct} (Ω)
C-PSC	20.46	97.45
FC-PSC	17.46	86.27

3.3.4. Ambient and moisture stabilities of F-doped C-PSCs

To confirm that device stability by fluorination is further improved, FC-PSC was compared with a conventional C-PSC. **Figure 85** indicates the long-term stability of C-PSC w/o and with F-plasma treatment stored under ambient conditions (temperature: 25 °C, relative humidity: $40 \pm 5\%$). The initial PCE of the pristine C-PSC was 12.85% at the start of measurement but gradually decreased to 10.95% after 1000 h, maintaining about 85% of the initial performance. In carbon-based PSCs, there is no deterioration factor at the interface due to HTM, which ensures relatively long-term stability. Surprisingly, the efficiency of the F plasma-treated device was maintained 95% of its initial performance (from 14.67% to 14.01%), demonstrating excellent ambient stability. In addition, the fluorinated carbon electrode showed a decrease in efficiency even under relatively high humidity conditions (RH = 60 or $80 \pm 5\%$), but revealed higher moisture stability than conventional carbon electrodes (**Figure 86**). Since hydrophobic fluorine atoms are introduced into the existing hydrophobic carbon layer, a synergistic effect forms a super-hydrophobic layer, which provides additional protection against water penetration [188]. The contact angle was measured to confirm the increase in hydrophobicity. For the conventional

carbon electrode, the contact angle was 97.8° , but the contact angle of the F-treated carbon electrode highly increased to 135.5° due to the improvement of hydrophobicity, as illustrated in **Figure 87**.

An efficiency change after immersion in water to confirm the increased water stability of FC-PSC with enhanced hydrophobicity (**Figure 88a**). The moisture stability test was conducted under severe conditions of dipping C-PSC and FC-PSC for 10 min in a water bath. C-PSC sample manifested 32% of initial efficiency after immersion in the water bath, while the FC-PSC maintained 82% of initial PCE. These results mean that the hydrophobic carbon itself partially inhibited moisture penetration onto the perovskite active layer, but the carbon layer containing hydrophobic fluorine blocked the penetrable moisture more effectively into pores present in the carbon layer. To verify the inhibiting moisture penetration of the FC-PSC, which had been immersed in water, was immersed in CB to peel off the carbon, and the perovskite film was observed. Optical microscopic and digital photographic images in **Figure 88b**, show the difference in the damage of the perovskite under the carbon following F plasma treatment. It was affirmed that the perovskite layer under the F-treated carbon electrode was hardly damaged and the water permeability was well suppressed.

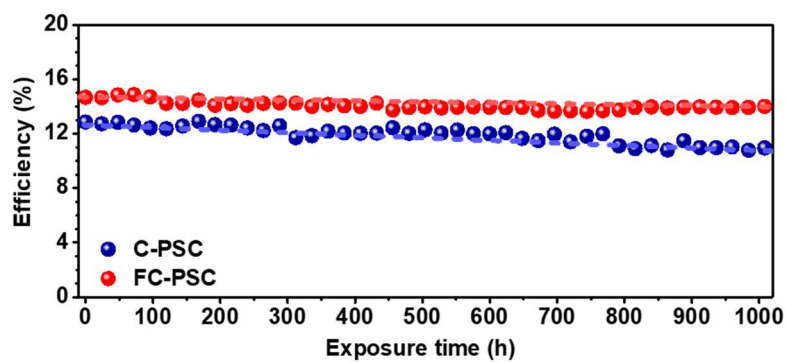


Figure 85. Long-term stability of the C-PSC and FC-PSC devices under controlled ambient conditions (temperature: 25 °C; relative humidity: 40 ± 5%).

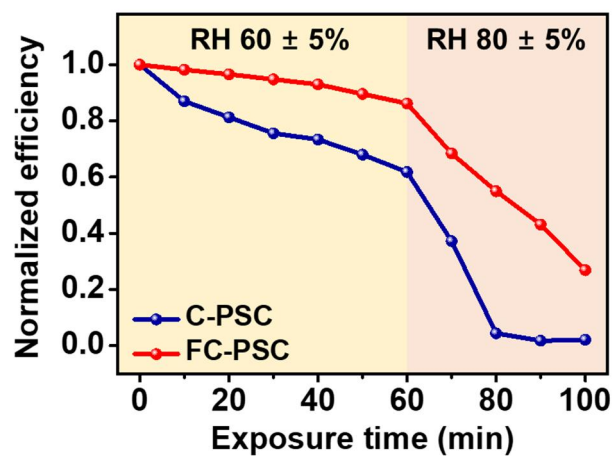


Figure 86. (a) Stability test of the CE and FPCE devices under high humidity conditions (temperature: 25 °C; relative humidity: 60 and 80 ± 5 %).

a)

W/O F-plasma treatment
97.8 °



b)

With F-plasma treatment
135.5 °



Figure 87. Water contact angles (a) w/o and (b) with F plasma treatment on the carbon electrode (C-PSC = 97.8°, FC-PSC = 135.5°).

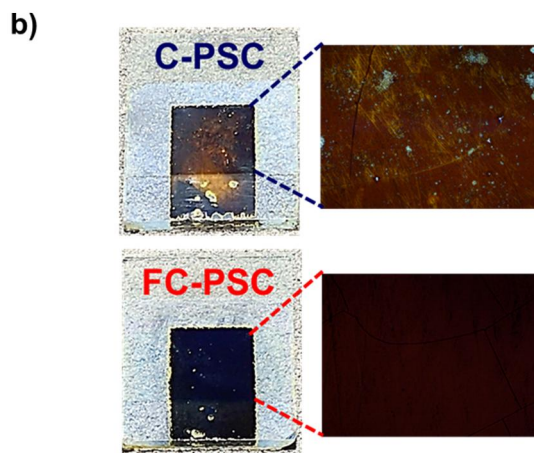
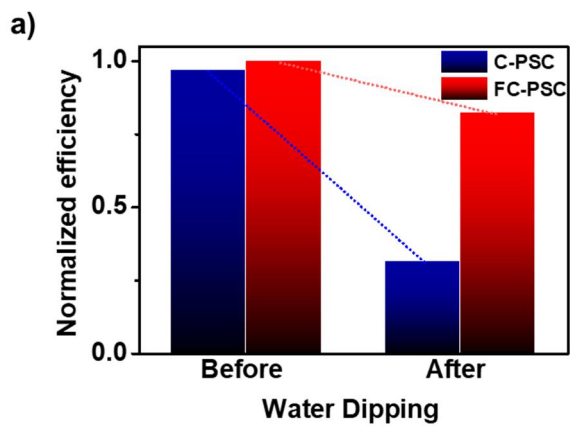


Figure 88. (a) Efficiency change of w/o and with F plasma-treated device after 10 min immersion test. (b) Digital photographic and optical microscopic images of the device.

4. Conclusion

Various process/material-based interface engineering of carbon electrode-based PSCs were fabricated to improve process efficiency and device stability issues related to commercialization, as well as to improve performance, and successfully produced a remarkable efficiency comparable with conventional PSCs through various interface engineering. The two-dimensional perovskite interfacial layer was introduced to the prepared C-PSCs through a post-treatment process. Furthermore, the secondary growth of the MAPbI₃ interfacial layer was induced through the further introduction of colloidal PbI₂ based on an organic acid dispersed in a non-polar solvent and sequential MAI treatment. This result recorded the highest efficiency among the existing hole conductor-free C-PSCs. In terms of the process, through the plasma process, rather than the solution process, a study was conducted to control the interfacial energy level through the introduction of specific elements. In this study, the interface energy level was well-aligned by the fabrication of a fluorine-doped carbon electrode *via* F-plasma treatment to improve the device performance. The C-PSC produced through the

interfacial process showed high atmospheric stability and improved performance. The subtopics are concluded in the viewpoint of each subtopic as follows:

1. The carbon electrode is post-treated with a phenylethylammonium iodide (PEAI) solution, for the growth of a two-dimensional perovskite (2D PSK) at the interface between the perovskite and the carbon layer. The ultra-thin PEA_2PbI_4 layer formed within the perovskite/carbon interface improved poor contact between the perovskite and carbon. The favorable conduction and valence band energy levels of the 2D perovskite interfacial layer significantly inhibited interfacial charge recombination due to the absence of HTM. Using this interface engineering method based on solution treatment of large organic spacer, the average PCE of the device improved from 11.5% to 14.5% with minimal hysteresis loss, and the maximum PCE reached 15.6%. Additionally, the PEAi treatment device manifested excellent ambient stability. The synergetic protection of the hydrophobic carbon and 2D perovskite layer can maintain 92% of the initial PCE after exposure to ambient conditions (relative humidity: $40 \pm 5\%$) for 1000 h. The thermal

stability of the device was also improved to suppress the ion migration and there was no efficiency loss after thermal testing at 150 °C.

2. To form an interface layer with improved interfacial contact properties, colloidal PbI_2 capped with an organic acid that can be dispersed in anti-solvent (chlorobenzene) is prepared to introduce as an additional PbI_2 source on a prepared PSC. Nano-sized hexagonal crystalline PbI_2 uniformly dispersed in chlorobenzene passed through the mesoporous carbon layer and introduced at the interface between the carbon electrode and perovskite layers. Subsequently, a secondary grown MAPbI_3 interfacial layer was introduced by treatment with methylammonium iodide (MAI). In the case of additional PbI_2 treatment, the efficiency is slightly improved compared to the existing device efficiency (PCE= 12.86% to 13.12%), because treatment of the non-polar solvent recrystallizes the carbon electrode and PbI_2 acts as a partial passivation layer. On the other hand, when a second-grown MAPbI_3 interfacial layer is introduced according to additional organic ligand treatment, the PCE of the device increases from 12.86% to 16.32% and the maximum value reaches 16.98% ($V_{oc} = 1.03$ V, $J_{sc} = 22.81$ mA cm⁻², FF = 0.72). This result demonstrates the highest efficiency of the hole conductor-free C-

PSCs studied to date. Also, even in a large active area test of 1 cm², device performance is greatly improved with an efficiency close to 12%. The device performance improvement is because the hole extraction ability for the carbon electrode is improved and the interface charge recombination is suppressed by the energy level alignment by the hierarchical PSK structure formed by the secondary-grown MAPbI₃ interfacial layer. In long-term stability testing, C-PSCs with MAPbI₃ interfacial layer retain 95% of initial efficiency over a month's ambient exposure, with little performance degradation. These results are believed to be due to the effect of inhibiting water penetration by organic acids present in colloidal PbI₂. Besides, when only PbI₂ is treated, it is confirmed that the excessively large amount of PbI₂ acts as a factor that promotes the deterioration of the bulk perovskite film, and the efficiency was greatly reduced after a certain period.

3. In this section, Fluorine (F)-doped carbon electrodes were prepared by C₄F₈ vacuum plasma treatment on hydrophobic carbon to form superhydrophobic carbon electrodes through synergistic effect improving long-term stability and moisture resistance of C-PSC. In addition, plasma-based fluorine treatment adjusts the energy level while

introducing fluorine in a concentration gradient to the carbon layer and increases PCE by improving hole extraction at the interface between the perovskite and carbon electrode. After the plasma treatment, PCE increased by about 20% (from 11.76% to 14.70%), and in particular, the FF was noticeably improved from 0.58 to 0.69, demonstrating improved interface charge mobility. The efficiency of the F plasma-treated C-PSC maintained 95% (14.67% to 14.01%) of the initial performance even after 1000 h and showed excellent ambient stability. Also, the high water-resistance of the device was confirmed by maintaining 82% of the initial efficiency even when immersed directly in a water bath for 10 min.

References

- [1] Q. Schiermeier, J. Tollefson, T. Scully, A. Witze, O. Morton, *Nature*, **2008**, 454, 816.
- [2] F. Creutzig, P. Agoston, J. C. Goldschmidt, G. Luderer, G. Nemet, R. C. Pietzcker, *Nature Energy*, **2017**, 2.
- [3] K. Yoshikawa, H. Kawasaki, W. Yoshida, T. Irie, K. Konishi, K. Nakano, T. Uto, D. Adachi, M. Kanematsu, H. Uzu, K. Yamamoto, *Nature Energy*, **2017**, 2, 17032.
- [4] W. Metaferia, K. L. Schulte, J. Simon, S. Johnston, A. J. Ptak, *Nature Communications*, **2019**, 10.
- [5] A. Chirilă, S. Buecheler, F. Pianezzi, P. Bloesch, C. Gretener, A. R. Uhl, C. Fella, L. Kranz, J. Perrenoud, S. Seyrling, R. Verma, S. Nishiwaki, Y. E. Romanyuk, G. Bilger, A. N. Tiwari, *Nature Materials*, **2011**, 10, 857.
- [6] W. Li, R. Yang, D. Wang, *Solar Energy Materials and Solar Cells*, **2014**, 123, 249.
- [7] T. R. Andersen, H. F. Dam, M. Hösel, M. Helgesen, J. E. Carlé, T. T. Larsen-Olsen, S. A. Gevorgyan, J. W. Andreasen, J. Adams, N. Li, F. Machui, G. D. Spyropoulos, T. Ameri, N. Lemaître, M. Legros, A. Scheel, D. Gaiser, K. Kreul, S. Berny, O. R. Lozman, S. Nordman, M. Välimäki, M. Vilkmann, R. R. Søndergaard, M. Jørgensen, C. J. Brabec, F. C. Krebs, *Energy & Environmental Science*, **2014**, 7, 2925.
- [8] B. O'Regan, M. Grätzel, *Nature*, **1991**, 353, 737.
- [9] T. Ibn-Mohammed, S. C. L. Koh, I. M. Reaney, A. Acquaye, G. Schileo, K. B. Mustapha, R. Greenough, *Renewable and Sustainable Energy Reviews*, **2017**, 80, 1321.
- [10] A. Kojima, K. Teshima, Y. Shirai, T. Miyasaka, *Journal of the American Chemical Society*, **2009**, 131, 6050.

- [11] G. Hodes, *Science*, **2013**, 342, 317.
- [12] E. H. Jung, N. J. Jeon, E. Y. Park, C. S. Moon, T. J. Shin, T.-Y. Yang, J. H. Noh, J. Seo, *Nature*, **2019**, 567, 511.
- [13] Research Cell Efficiency Records. Available online: <https://www.nrel.gov/pv/assets/pdfs/best-research-cell-efficiencies.20200406.pdf> (accessed on 23 May 2020).
- [14] X. Zhao, M. Wang, *Materials Today Energy*, **2018**, 7, 208.
- [15] G. E. Eperon, S. D. Stranks, C. Menelaou, M. B. Johnston, L. M. Herz, H. J. Snaith, *Energy & Environmental Science*, **2014**, 7, 982.
- [16] W.-J. Yin, T. Shi, Y. Yan, *Advanced Materials*, **2014**, 26, 4653.
- [17] S. De Wolf, J. Holovsky, S.-J. Moon, P. Löper, B. Niesen, M. Ledinsky, F.-J. Haug, J.-H. Yum, C. Ballif, *The Journal of Physical Chemistry Letters*, **2014**, 5, 1035.
- [18] T. Leijtens, S. D. Stranks, G. E. Eperon, R. Lindblad, E. M. J. Johansson, I. J. McPherson, H. Rensmo, J. M. Ball, M. M. Lee, H. J. Snaith, *ACS Nano*, **2014**, 8, 7147.
- [19] D. Shi, V. Adinolfi, R. Comin, M. Yuan, E. Alarousu, A. Buin, Y. Chen, S. Hoogland, A. Rothenberger, K. Katsiev, Y. Losovyj, X. Zhang, P. A. Dowben, O. F. Mohammed, E. H. Sargent, O. M. Bakr, *Science*, **2015**, 347, 519.
- [20] Q. Dong, Y. Fang, Y. Shao, P. Mulligan, J. Qiu, L. Cao, J. Huang, *Science*, **2015**, 347, 967.
- [21] F. Li, C. Ma, H. Wang, W. Hu, W. Yu, A. D. Sheikh, T. Wu, *Nature Communications*, **2015**, 6, 8238.
- [22] D. P. McMeekin, G. Sadoughi, W. Rehman, G. E. Eperon, M. Saliba, M. T. Horantner, A. Haghighirad, N. Sakai, L. Korte, B. Rech, M. B. Johnston, L. M. Herz, H. J. Snaith, *Science*, **2016**, 351, 151.
- [23] F. Hao, C. C. Stoumpos, R. P. H. Chang, M. G. Kanatzidis, *Journal of the American Chemical Society*, **2014**, 136, 8094.
- [24] Z. Li, T. R. Klein, D. H. Kim, M. Yang, J. J. Berry, M. F. A. M.

- Van Hest, K. Zhu, *Nature Reviews Materials*, **2018**, 3, 18017.
- [25] Y. Zhou, K. Zhu, *ACS Energy Letters*, **2016**, 1, 64.
- [26] M. Qin, J. Cao, T. Zhang, J. Mai, T.-K. Lau, S. Zhou, Y. Zhou, J. Wang, Y.-J. Hsu, N. Zhao, J. Xu, X. Zhan, X. Lu, *Advanced Energy Materials*, **2018**, 8, 1703399.
- [27] N. J. Jeon, H. Na, E. H. Jung, T.-Y. Yang, Y. G. Lee, G. Kim, H.-W. Shin, S. Il Seok, J. Lee, J. Seo, *Nature Energy*, **2018**, 3, 682.
- [28] S. Ito, S. Tanaka, K. Manabe, H. Nishino, *The Journal of Physical Chemistry C*, **2014**, 118, 16995.
- [29] I. Hwang, I. Jeong, J. Lee, M. J. Ko, K. Yong, *ACS Applied Materials & Interfaces*, **2015**, 7, 17330.
- [30] Y. Chen, L. Zhang, Y. Zhang, H. Gao, H. Yan, *RSC Advances*, **2018**, 8, 10489.
- [31] S. Albrecht, M. Saliba, J. P. Correa Baena, F. Lang, L. Kegelman, M. Mews, L. Steier, A. Abate, J. Rappich, L. Korte, R. Schlattmann, M. K. Nazeeruddin, A. Hagfeldt, M. Grätzel, B. Rech, *Energy & Environmental Science*, **2016**, 9, 81.
- [32] J.-P. Correa-Baena, M. Saliba, T. Buonassisi, M. Grätzel, A. Abate, W. Tress, A. Hagfeldt, *Science*, **2017**, 358, 739.
- [33] M. Saliba, T. Matsui, K. Domanski, J. Y. Seo, A. Ummadisingu, S. M. Zakeeruddin, J. P. Correa-Baena, W. R. Tress, A. Abate, A. Hagfeldt, M. Grätzel, *Science*, **2016**, 354, 206.
- [34] R. Wang, M. Mujahid, Y. Duan, Z. K. Wang, J. Xue, Y. Yang, *Advanced Functional Materials*, **2019**, 29, 1808843.
- [35] J. Chen, J.-Y. Seo, N.-G. Park, *Advanced Energy Materials*, **2018**, 1702714.
- [36] K. O. Brinkmann, J. Zhao, N. Pourdavoud, T. Becker, T. Hu, S. Olthof, K. Meerholz, L. Hoffmann, T. Gahlmann, R. Heiderhoff, M. F. Oszajca, N. A. Luechinger, D. Rogalla, Y. Chen, B. Cheng, T. Riedl, *Nature Communications*, **2017**, 8, 13938.

- [37] Y. Kato, L. K. Ono, M. V. Lee, S. Wang, S. R. Raga, Y. Qi, *Advanced Materials Interfaces*, **2015**, 2, 1500195.
- [38] K. Domanski, J.-P. Correa-Baena, N. Mine, M. K. Nazeeruddin, A. Abate, M. Saliba, W. Tress, A. Hagfeldt, M. Grätzel, *ACS Nano*, **2016**, 10, 6306.
- [39] A. K. Jena, A. Kulkarni, T. Miyasaka, *Chemical Reviews*, **2019**, 119, 3036.
- [40] Z. Ku, Y. Rong, M. Xu, T. Liu, H. Han, *Scientific Reports*, **2013**, 3.
- [41] Y. Yang, J. Xiao, H. Wei, L. Zhu, D. Li, Y. Luo, H. Wu, Q. Meng, *RSC Adv.*, **2014**, 4, 52825.
- [42] Z. Wei, H. Chen, K. Yan, X. Zheng, S. Yang, *Journal of Materials Chemistry A*, **2015**, 3, 24226.
- [43] X. Zheng, H. Chen, Q. Li, Y. Yang, Z. Wei, Y. Bai, Y. Qiu, D. Zhou, K. S. Wong, S. Yang, **2017**.
- [44] Z. Wei, H. Chen, K. Yan, S. Yang, *Angewandte Chemie International Edition*, **2014**, 53, 13239.
- [45] H. Wei, J. Xiao, Y. Yang, S. Lv, J. Shi, X. Xu, J. Dong, Y. Luo, D. Li, Q. Meng, *Carbon*, **2015**, 93, 861.
- [46] F. Meng, L. Gao, Y. Yan, J. Cao, N. Wang, T. Wang, T. Ma, *Carbon*, **2019**, 145, 290.
- [47] Y. Yang, Z. Liu, W. K. Ng, L. Zhang, H. Zhang, X. Meng, Y. Bai, S. Xiao, T. Zhang, C. Hu, K. S. Wong, S. Yang, *Advanced Functional Materials*, **2019**, 29, 1806506.
- [48] H. Zhou, Y. Shi, Q. Dong, H. Zhang, Y. Xing, K. Wang, Y. Du, T. Ma, *The Journal of Physical Chemistry Letters*, **2014**, 5, 3241.
- [49] X. Wu, L. Xie, K. Lin, J. Lu, K. Wang, W. Feng, B. Fan, P. Yin, Z. Wei, *Journal of Materials Chemistry A*, **2019**, 7, 12236.
- [50] A. Mei, X. Li, L. Liu, Z. Ku, T. Liu, Y. Rong, M. Xu, M. Hu, J. Chen, Y. Yang, M. Gratzel, H. Han, *Science*, **2014**, 345, 295.

- [51] T. S. Sherkar, C. Momblona, L. Gil-Escrig, J. Ávila, M. Sessolo, H. J. Bolink, L. J. A. Koster, *ACS Energy Letters*, **2017**, 2, 1214.
- [52] T. Chen, Z. Sun, M. Liang, S. Xue, *Physical Chemistry Chemical Physics*, **2020**, 22, 245.
- [53] J. Shi, X. Xu, D. Li, Q. Meng, *Small*, **2015**, 11, 2472.
- [54] Z. Yang, J. Dou, M. Wang, *Solar RRL*, **2018**, 2, 1800177.
- [55] Z. Hawash, S. R. Raga, D.-Y. Son, L. K. Ono, N.-G. Park, Y. Qi, *The Journal of Physical Chemistry Letters*, **2017**, 8, 3947.
- [56] Y. Hou, X. Du, S. Scheiner, D. P. McMeekin, Z. Wang, N. Li, M. S. Killian, H. Chen, M. Richter, I. Levchuk, N. Schrenker, E. Spiecker, T. Stubhan, N. A. Luechinger, A. Hirsch, P. Schmuki, H.-P. Steinrück, R. H. Fink, M. Halik, H. J. Snaith, C. J. Brabec, *Science*, **2017**, 358, 1192.
- [57] N. K. Noel, A. Abate, S. D. Stranks, E. S. Parrott, V. M. Burlakov, A. Goriely, H. J. Snaith, *ACS Nano*, **2014**, 8, 9815.
- [58] F. Cai, J. Cai, L. Yang, W. Li, R. S. Gurney, H. Yi, A. Iraqi, D. Liu, T. Wang, *Nano Energy*, **2018**, 45, 28.
- [59] X. Xiao, J. Dai, Y. Fang, J. Zhao, X. Zheng, S. Tang, P. N. Rudd, X. C. Zeng, J. Huang, *ACS Energy Letters*, **2018**, 3, 684.
- [60] L. Zuo, Z. Gu, T. Ye, W. Fu, G. Wu, H. Li, H. Chen, *Journal of the American Chemical Society*, **2015**, 137, 2674.
- [61] S. N. Habisreutinger, T. Leijtens, G. E. Eperon, S. D. Stranks, R. J. Nicholas, H. J. Snaith, *Nano Letters*, **2014**, 14, 5561.
- [62] W.-Q. Wu, Q. Wang, Y. Fang, Y. Shao, S. Tang, Y. Deng, H. Lu, Y. Liu, T. Li, Z. Yang, A. Gruverman, J. Huang, *Nature Communications*, **2018**, 9.
- [63] M. Jung, S.-G. Ji, G. Kim, S. I. Seok, *Chemical Society Reviews*, **2019**, 48, 2011.
- [64] J. Yang, B. D. Siempelkamp, D. Liu, T. L. Kelly, *ACS Nano*, **2015**, 9, 1955.
- [65] K.-M. Lee, C.-J. Lin, B.-Y. Liou, S.-M. Yu, C.-C. Hsu, V.

- Suryanarayanan, M.-C. Wu, *Solar Energy Materials and Solar Cells*, **2017**, 172, 368.
- [66] Y. Wang, J. Wu, P. Zhang, D. Liu, T. Zhang, L. Ji, X. Gu, Z. David Chen, S. Li, *Nano Energy*, **2017**, 39, 616.
- [67] C.-C. Chueh, C.-Z. Li, A. K. Y. Jen, *Energy & Environmental Science*, **2015**, 8, 1160.
- [68] X. Zheng, B. Chen, J. Dai, Y. Fang, Y. Bai, Y. Lin, H. Wei, Xiao, J. Huang, *Nature Energy*, **2017**, 2, 17102.
- [69] L.-B. Huang, P.-Y. Su, J.-M. Liu, J.-F. Huang, Y.-F. Chen, S. Qin, J. Guo, Y.-W. Xu, C.-Y. Su, *Journal of Power Sources*, **2018**, 378, 483.
- [70] F. Wang, A. Shimazaki, F. Yang, K. Kanahashi, K. Matsuki, Y. Miyauchi, T. Takenobu, A. Wakamiya, Y. Murata, K. Matsuda, *The Journal of Physical Chemistry C*, **2017**, 121, 1562.
- [71] H. Zhang, J. Shi, L. Zhu, Y. Luo, D. Li, H. Wu, Q. Meng, *Nano Energy*, **2018**, 43, 383.
- [72] M. Cha, P. Da, J. Wang, W. Wang, Z. Chen, F. Xiu, G. Zheng, Z.-S. Wang, *Journal of the American Chemical Society*, **2016**, 138, 8581.
- [73] G. Huang, C. Wang, H. Zhang, S. Xu, Q. Xu, Y. Cui, *Journal of Materials Chemistry A*, **2018**, 6, 2449.
- [74] T. Liu, Z. Wang, L. Lou, S. Xiao, S. Zheng, S. Yang, *Solar RRL*, **2020**, 4, 1900278.
- [75] J. Ryu, K. Lee, J. Yun, H. Yu, J. Lee, J. Jang, *Small*, **2017**, 13, 1701225.
- [76] H. Tsai, W. Nie, J.-C. Blancon, C. C. Stoumpos, R. Asadpour, B. Harutyunyan, A. J. Neukirch, R. Verduzco, J. J. Crochet, S. Tretiak, L. Pedesseau, J. Even, M. A. Alam, G. Gupta, J. Lou, P. M. Ajayan, M. J. Bedzyk, M. G. Kanatzidis, A. D. Mohite, *Nature*, **2016**, 536, 312.
- [77] Y. Lin, Y. Bai, Y. Fang, Z. Chen, S. Yang, X. Zheng, S. Tang, Y. Liu, J. Zhao, J. Huang, *The Journal of Physical Chemistry Letters*, **2018**, 9, 654.

- [78] I. C. Smith, E. T. Hoke, D. Solis-Ibarra, M. D. McGehee, H. I. Karunadasa, *Angewandte Chemie International Edition*, **2014**, 53, 11232.
- [79] C. Ortiz-Cervantes, P. Carmona-Monroy, D. Solis-Ibarra, *ChemSusChem*, **2019**, 12, 1560.
- [80] L. Mao, W. Ke, L. Pedesseau, Y. Wu, C. Katan, J. Even, M. R. Wasielewski, C. C. Stoumpos, M. G. Kanatzidis, *Journal of the American Chemical Society*, **2018**, 140, 3775.
- [81] Y. Chen, S. Yu, Y. Sun, Z. Liang, *The Journal of Physical Chemistry Letters*, **2018**, 9, 2627.
- [82] C.-H. Chen, Z. Li, Q. Xue, Y.-A. Su, C.-C. Lee, H.-L. Yip, W.-C. Chen, C.-C. Chueh, *Organic Electronics*, **2019**, 75, 105400.
- [83] Y. Lin, Y. Bai, Y. Fang, Q. Wang, Y. Deng, J. Huang, *ACS Energy Letters*, **2017**, 2, 1571.
- [84] L. N. Quan, M. Yuan, R. Comin, O. Voznyy, E. M. Beaugard, S. Hoogland, A. Buin, A. R. Kirmani, K. Zhao, A. Amassian, D. H. Kim, E. H. Sargent, *Journal of the American Chemical Society*, **2016**, 138, 2649.
- [85] T. M. Koh, V. Shanmugam, J. Schlipf, L. Oesinghaus, P. Müller-Buschbaum, N. Ramakrishnan, V. Swamy, N. Mathews, P. P. Boix, S. G. Mhaisalkar, *Advanced Materials*, **2016**, 28, 3653.
- [86] D. S. Lee, J. S. Yun, J. Kim, A. M. Soufiani, S. Chen, Y. Cho, X. Deng, J. Seidel, S. Lim, S. Huang, A. W. Y. Ho-Baillie, *ACS Energy Letters*, **2018**, 3, 647.
- [87] F. Wang, W. Geng, Y. Zhou, H.-H. Fang, C.-J. Tong, M. A. Loi, L.-M. Liu, N. Zhao, *Advanced Materials*, **2016**, 28, 9986.
- [88] Y. Bai, S. Xiao, C. Hu, T. Zhang, X. Meng, H. Lin, Y. Yang, S. Yang, *Advanced Energy Materials*, **2017**, 7, 1701038.
- [89] K. T. Cho, G. Grancini, Y. Lee, E. Oveisi, J. Ryu, O. Almora, M. Tschumi, P. A. Schouwink, G. Seo, S. Heo, J. Park, J. Jang, S. Paek, G. Garcia-Belmonte, M. K. Nazeeruddin, *Energy & Environmental Science*,

2018, 11, 952.

[90] T. M. Koh, V. Shanmugam, X. Guo, S. S. Lim, O. Filonik, E. M. Herzig, P. Müller-Buschbaum, V. Swamy, S. T. Chien, S. G. Mhaisalkar, N. Mathews, *Journal of Materials Chemistry A*, **2018**, 6, 2122.

[91] P. Chen, Y. Bai, S. Wang, M. Lyu, J.-H. Yun, L. Wang, *Advanced Functional Materials*, **2018**, 28, 1706923.

[92] H. Kim, S. U. Lee, D. Y. Lee, M. J. Paik, H. Na, J. Lee, S. I. Seok, *Advanced Energy Materials*, **2019**, 9, 1902740.

[93] Y. Zhang, J. Chen, X. Lian, M. Qin, J. Li, T. R. Andersen, X. Lu, G. Wu, H. Li, H. Chen, *Small Methods*, **2019**, 3, 1900375.

[94] E. Aydin, M. Bastiani, S. Wolf, *Advanced Materials*, **2019**, 31, 1900428.

[95] M. De Bastiani, E. Aydin, T. Allen, D. Walter, A. Fell, J. Peng, N. Gasparini, J. Troughton, D. Baran, K. Weber, T. P. White, S. De Wolf, *Advanced Electronic Materials*, **2019**, 5, 1800500.

[96] Q. Chen, H. Zhou, T.-B. Song, S. Luo, Z. Hong, H.-S. Duan, L. Dou, Y. Liu, Y. Yang, *Nano Letters*, **2014**, 14, 4158.

[97] T. J. Jacobsson, J.-P. Correa-Baena, E. Halvani Anaraki, B. Philippe, S. D. Stranks, M. E. F. Bouduban, W. Tress, K. Schenk, J. Teuscher, J.-E. Moser, H. Rensmo, A. Hagfeldt, *Journal of the American Chemical Society*, **2016**, 138, 10331.

[98] C. Roldán-Carmona, P. Gratia, I. Zimmermann, G. Grancini, P. Gao, M. Graetzel, M. K. Nazeeruddin, *Energy & Environmental Science*, **2015**, 8, 3550.

[99] J. Holovský, S. De Wolf, J. Werner, Z. Remes, M. Müller, N. Neykova, M. Ledinsky, L. Černá, P. Hrzina, P. Löper, B. Niesen, C. Ballif, **2017**.

[100] D. Chen, X. Li, A. Su, H. Dong, S. Pang, W. Zhu, H. Xi, J. Zhang, C. Zhang, Y. Hao, *Dalton Transactions*, **2019**, 48, 5292.

[101] G. Han, T. M. Koh, S. S. Lim, T. W. Goh, X. Guo, S. W. Leow,

- R. Begum, T. C. Sum, N. Mathews, S. Mhaisalkar, *ACS Applied Materials & Interfaces*, **2017**, 9, 21292.
- [102] C. Xin, J. Zhang, X. Zhou, L. Ma, F. Hou, B. Shi, S. Pan, B. Chen, P. Wang, D. Zhang, X. Chen, Y. Zhao, A. A. Bakulin, Y. Li, X. Zhang, *ACS Applied Energy Materials*, **2020**, 3, 3318.
- [103] K. T. Cho, S. Paek, G. Grancini, C. Roldán-Carmona, P. Gao, Y. Lee, M. K. Nazeeruddin, *Energy & Environmental Science*, **2017**, 10, 621.
- [104] T. Niu, J. Lu, X. Jia, Z. Xu, M.-C. Tang, D. Barrit, N. Yuan, J. Ding, X. Zhang, Y. Fan, T. Luo, Y. Zhang, D.-M. Smilgies, Z. Liu, A. Amassian, S. Jin, K. Zhao, S. Liu, *Nano Letters*, **2019**, 19, 7181.
- [105] N. Hojnik, U. Cvelbar, G. Tavčar-Kalcher, J. Walsh, I. Križaj, *Toxins*, **2017**, 9, 151.
- [106] K. N. Kim, S. M. Lee, A. Mishra, G. Y. Yeom, *Thin Solid Films*, **2016**, 598, 315.
- [107] L. Phan, S. Yoon, M.-W. Moon, *Polymers*, **2017**, 9, 417.
- [108] Palumbo, P. Lo, Favia, *Coatings*, **2019**, 9, 640.
- [109] M. Iqbal, D. K. Dinh, Q. Abbas, M. Imran, H. Sattar, A. Ul Ahmad, *Surfaces*, **2019**, 2, 349.
- [110] K. He, X. Yang, H. Yan, Z. Wu, Z. Li, S. Zhong, Q. Ou, R. Liang, *Organic Electronics*, **2014**, 15, 1731.
- [111] C. Zhang, L. Qi, Q. Chen, L. Lv, Y. Ning, Y. Hu, Y. Hou, F. Teng, **2014**, 2, 8715.
- [112] Y. Jiao, Y. Zheng, K. Davey, S.-Z. Qiao, *Nature Energy*, **2016**, 1, 16130.
- [113] J. Duch, P. Kubisiak, K. H. Adolfsson, M. Hakkarainen, M. Golda-Cepa, A. Kotarba, *Applied Surface Science*, **2017**, 419, 439.
- [114] T. Lim, S. Ju, *Surface and Coatings Technology*, **2017**, 328, 89.
- [115] K. Akada, S. Obata, K. Saiki, *ACS Omega*, **2019**, 4, 16531.
- [116] A. Dey, P. Ghosh, J. Bowen, N. S. J. Braithwaite, S.

- Krishnamurthy, *Physical Chemistry Chemical Physics*, **2020**.
- [117] S. Kang, M. He, M. Chen, Z. Wang, Z. Sun, H. Dang, X. Chang, M. Dong, P. Liu, L. Cui, *Journal of Colloid and Interface Science*, **2019**, 556, 214.
- [118] D. I. Kim, J. W. Lee, R. H. Jeong, S.-H. Nam, K.-H. Hwang, J.-H. Boo, *Surface and Coatings Technology*, **2019**, 357, 189.
- [119] C. Tian, A. Mei, S. Zhang, H. Tian, S. Liu, F. Qin, Y. Xiong, Y. Rong, Y. Hu, Y. Zhou, S. Xie, H. Han, *Nano Energy*, **2018**, 53, 160.
- [120] N. J. Jeon, J. H. Noh, W. S. Yang, Y. C. Kim, S. Ryu, J. Seo, S. I. Seok, *Nature*, **2015**, 517, 476.
- [121] E. H. Anaraki, A. Kermanpur, L. Steier, K. Domanski, T. Matsui, W. Tress, M. Saliba, A. Abate, M. Grätzel, A. Hagfeldt, J.-P. Correa-Baena, *Energy & Environmental Science*, **2016**, 9, 3128.
- [122] J. H. Heo, H. J. Han, D. Kim, T. K. Ahn, S. H. Im, *Energy & Environmental Science*, **2015**, 8, 1602.
- [123] C. Lee, Y.-J. Han, Y. D. Seo, K. Nakabayashi, J. Miyawaki, R. Santamaría, R. Menéndez, S.-H. Yoon, J. Jang, *Carbon*, **2016**, 103, 28.
- [124] M. Saliba, T. Matsui, J.-Y. Seo, K. Domanski, J.-P. Correa-Baena, M. K. Nazeeruddin, S. M. Zakeeruddin, W. Tress, A. Abate, A. Hagfeldt, M. Grätzel, *Energy & Environmental Science*, **2016**, 9, 1989.
- [125] W. Rehman, D. P. McMeekin, J. B. Patel, R. L. Milot, M. B. Johnston, H. J. Snaith, L. M. Herz, *Energy & Environmental Science*, **2017**, 10, 361.
- [126] X. Liu, Z. Liu, B. Sun, X. Tan, H. Ye, Y. Tu, T. Shi, Z. Tang, G. Liao, *Nano Energy*, **2018**, 50, 201.
- [127] H.-H. Fang, J. Yang, S. Tao, S. Adjokatse, M. E. Kamminga, J. Ye, G. R. Blake, J. Even, M. A. Loi, *Advanced Functional Materials*, **2018**, 28, 1800305.
- [128] L. Zhu, H. Zhang, Q. Lu, Y. Wang, Z. Deng, Y. Hu, Z. Lou, Q. Cui, Y. Hou, F. Teng, *Journal of Materials Chemistry C*, **2018**, 6, 3945.

- [129] J. J. van Franeker, K. H. Hendriks, B. J. Bruijnaers, M. W. G. M. Verhoeven, M. M. Wienk, R. A. J. Janssen, *Advanced Energy Materials*, **2017**, 7, 1601822.
- [130] Y. Yuan, J. Huang, *Accounts of Chemical Research*, **2016**, 49, 286.
- [131] C. Li, S. Tscheuschner, F. Paulus, P. E. Hopkinson, J. Kießling, A. Köhler, Y. Vaynzof, S. Huettner, *Advanced Materials*, **2016**, 28, 2446.
- [132] C. Fei, B. Li, R. Zhang, H. Fu, J. Tian, G. Cao, *Advanced Energy Materials*, **2017**, 7, 1602017.
- [133] J. Peng, Y. Wu, W. Ye, D. A. Jacobs, H. Shen, X. Fu, Y. Wan, T. Duong, N. Wu, C. Barugkin, H. T. Nguyen, D. Zhong, J. Li, T. Lu, Y. Liu, M. N. Lockrey, K. J. Weber, K. R. Catchpole, T. P. White, *Energy & Environmental Science*, **2017**, 10, 1792.
- [134] S. Song, G. Kang, L. Pyeon, C. Lim, G.-Y. Lee, T. Park, J. Choi, *ACS Energy Letters*, **2017**, 2, 2667.
- [135] D. Yang, R. Yang, J. Zhang, Z. Yang, S. Liu, C. Li, *Energy & Environmental Science*, **2015**, 8, 3208.
- [136] Y. Cho, A. M. Soufiani, J. S. Yun, J. Kim, D. S. Lee, J. Seidel, X. Deng, M. A. Green, S. Huang, A. W. Y. Ho-Baillie, *Advanced Energy Materials*, **2018**, 8, 1703392.
- [137] S. Shao, M. Abdu-Aguye, L. Qiu, L.-H. Lai, J. Liu, S. Adjokatse, F. Jahani, M. E. Kamminga, G. H. ten Brink, T. T. M. Palstra, B. J. Kooi, J. C. Hummelen, M. Antonietta Loi, *Energy & Environmental Science*, **2016**, 9, 2444.
- [138] M. Jahandar, J. H. Heo, C. E. Song, K.-J. Kong, W. S. Shin, J.-C. Lee, S. H. Im, S.-J. Moon, *Nano Energy*, **2016**, 27, 330.
- [139] J. Yao, L. Yang, F. Cai, Y. Yan, R. S. Gurney, D. Liu, T. Wang, *Sustainable Energy & Fuels*, **2018**, 2, 436.
- [140] J. Yin, J. Cao, X. He, S. Yuan, S. Sun, J. Li, N. Zheng, L. Lin, *Journal of Materials Chemistry A*, **2015**, 3, 16860.

- [141] Z. Yu, B. Chen, P. Liu, C. Wang, C. Bu, N. Cheng, S. Bai, Y. Yan, X. Zhao, *Advanced Functional Materials*, **2016**, 26, 4866.
- [142] Y. Liu, Q. Chen, H.-S. Duan, H. Zhou, Y. Yang, H. Chen, S. Luo, T.-B. Song, L. Dou, Z. Hong, Y. Yang, *Journal of Materials Chemistry A*, **2015**, 3, 11940.
- [143] N. Arora, M. I. Dar, A. Hinderhofer, N. Pellet, F. Schreiber, S. M. Zakeeruddin, M. Grätzel, *Science*, **2017**, 358, 768.
- [144] A. Fakharuddin, L. Schmidt-Mende, G. Garcia-Belmonte, R. Jose, I. Mora-Sero, *Advanced Energy Materials*, **2017**, 7, 1700623.
- [145] S. Kim, S. Bae, S.-W. Lee, K. Cho, K. D. Lee, H. Kim, S. Park, G. Kwon, S.-W. Ahn, H.-M. Lee, Y. Kang, H.-S. Lee, D. Kim, *Scientific Reports*, **2017**, 7, 1200.
- [146] A. K. Jena, Y. Numata, M. Ikegami, T. Miyasaka, *Journal of Materials Chemistry A*, **2018**, 6, 2219.
- [147] W. Tan, A. R. Bowring, A. C. Meng, M. D. McGehee, P. C. McIntyre, *ACS Applied Materials & Interfaces*, **2018**, 10, 5485.
- [148] Q. Wang, B. Chen, Y. Liu, Y. Deng, Y. Bai, Q. Dong, J. Huang, *Energy & Environmental Science*, **2017**, 10, 516.
- [149] J. Stevenson, B. Sorenson, V. H. Subramaniam, J. Raiford, P. P. Khlyabich, Y.-L. Loo, P. Clancy, *Chemistry of Materials*, **2017**, 29, 2435.
- [150] K. L. Gardner, J. G. Tait, T. Merckx, W. Qiu, U. W. Paetzold, L. Kootstra, M. Jaysankar, R. Gehlhaar, D. Cheyns, P. Heremans, J. Poortmans, *Advanced Energy Materials*, **2016**, 6, 1600386.
- [151] J. C. Hamill, J. Schwartz, Y.-L. Loo, *ACS Energy Letters*, **2018**, 3, 92.
- [152] Z. Arain, C. Liu, Y. Yang, M. Mateen, Y. Ren, Y. Ding, X. Liu, Z. Ali, M. Kumar, S. Dai, *SCIENCE CHINA Materials*, **2019**, 62, 161.
- [153] P.-W. Liang, C.-Y. Liao, C.-C. Chueh, F. Zuo, S. T. Williams, X.-K. Xin, J. Lin, A. K. Y. Jen, *Advanced Materials*, **2014**, 26, 3748.
- [154] Y.-C. Wang, J. Chang, L. Zhu, X. Li, C. Song, J. Fang, *Advanced*

- Functional Materials*, **2018**, 28, 1706317.
- [155] S.-T. Ha, R. Su, J. Xing, Q. Zhang, Q. Xiong, *Chemical Science*, **2017**, 8, 2522.
- [156] Q. V. Le, K. Hong, H. W. Jang, S. Y. Kim, *Advanced Electronic Materials*, **2018**, 4, 1800335.
- [157] E. Klein, R. Lesyuk, C. Klinke, *Nanoscale*, **2018**, 10, 4442.
- [158] E. Klein, L. Heymann, A. B. Hungria, R. Lesyuk, C. Klinke, *Nanoscale*, **2018**, 10, 21197.
- [159] C. Ran, W. Gao, N. Li, Y. Xia, Q. Li, Z. Wu, H. Zhou, Y. Chen, M. Wang, W. Huang, *ACS Energy Letters*, **2019**, 4, 358.
- [160] A. Mishra, Z. Ahmad, F. Touati, R. A. Shakoor, M. K. Nazeeruddin, *RSC Advances*, **2019**, 9, 11589.
- [161] A. Kogo, T. Miyadera, M. Chikamatsu, *ACS Applied Materials & Interfaces*, **2019**, 11, 38683.
- [162] A. Ummadisingu, M. Grätzel, *Science Advances*, **2018**, 4, e1701402.
- [163] T. M. Brenner, Y. Rakita, Y. Orr, E. Klein, I. Feldman, M. Elbaum, D. Cahen, G. Hodes, *Chemistry of Materials*, **2016**, 28, 6501.
- [164] J. M. C. d. Silva Filho, V. A. Ermakov, F. C. Marques, *Scientific Reports*, **2018**, 8, 1563.
- [165] R. Szostak, J. C. Silva, S. H. Turren-Cruz, M. M. Soares, R. O. Freitas, A. Hagfeldt, H. C. N. Tolentino, A. F. Nogueira, *Science Advances*, **2019**, 5, eaaw6619.
- [166] S. M. Jain, B. Philippe, E. M. J. Johansson, B.-w. Park, H. Rensmo, T. Edvinsson, G. Boschloo, *Journal of Materials Chemistry A*, **2016**, 4, 2630.
- [167] S. Chen, Y. Hou, H. Chen, X. Tang, S. Langner, N. Li, T. Stubhan, I. Levchuk, E. Gu, A. Osvet, C. J. Brabec, *Advanced Energy Materials*, **2018**, 8, 1701543.
- [168] S. Ryu, J. H. Noh, N. J. Jeon, Y. Chan Kim, W. S. Yang, J. Seo,

- S. I. Seok, *Energy & Environmental Science*, **2014**, 7, 2614.
- [169] F. Tan, H. Tan, M. I. Saidaminov, M. Wei, M. Liu, A. Mei, P. Li, B. Zhang, C.-S. Tan, X. Gong, Y. Zhao, A. R. Kirmani, Z. Huang, J. Z. Fan, R. Quintero-Bermudez, J. Kim, Y. Zhao, O. Voznyy, Y. Gao, F. Zhang, L. J. Richter, Z.-H. Lu, W. Zhang, E. H. Sargent, *Advanced Materials*, **2019**, 31, 1807435.
- [170] W. Feng, C. Zhang, J.-X. Zhong, L. Ding, W.-Q. Wu, *Chemical Communications*, **2020**, 56, 5006.
- [171] F. Li, Y. Xie, Y. Hu, M. Long, Y. Zhang, J. Xu, M. Qin, X. Lu, M. Liu, *ACS Energy Letters*, **2020**, 5, 1422.
- [172] M.-C. Jung, S. R. Raga, L. K. Ono, Y. Qi, *Scientific Reports*, **2015**, 5, 9863.
- [173] C. Ding, Y. Zhang, F. Liu, Y. Kitabatake, S. Hayase, T. Toyoda, K. Yoshino, T. Minemoto, K. Katayama, Q. Shen, *Nano Energy*, **2018**, 53, 17.
- [174] J. Barbé, M. Newman, S. Lilliu, V. Kumar, H. K. H. Lee, C. Charbonneau, C. Rodenburg, D. Lidzey, W. C. Tsoi, *Journal of Materials Chemistry A*, **2018**, 6, 23010.
- [175] Z. Zhu, X. Zheng, Y. Bai, T. Zhang, Z. Wang, S. Xiao, S. Yang, *Physical Chemistry Chemical Physics*, **2015**, 17, 18265.
- [176] G. Kakavelakis, T. Maksudov, D. Konios, I. Paradisanos, G. Kioseoglou, E. Stratakis, E. Kymakis, *Advanced Energy Materials*, **2017**, 7, 1602120.
- [177] Y. Liu, B. He, J. Duan, Y. Zhao, Y. Ding, M. Tang, H. Chen, Q. Tang, *Journal of Materials Chemistry A*, **2019**, 7, 12635.
- [178] R. Singh, S. Sandhu, H. Yadav, J.-J. Lee, *ACS Applied Materials & Interfaces*, **2019**, 11, 29941.
- [179] J.-J. Li, J.-Y. Ma, Q.-Q. Ge, J.-S. Hu, D. Wang, L.-J. Wan, *ACS Applied Materials & Interfaces*, **2015**, 7, 28518.
- [180] F. Fu, S. Pisoni, Q. Jeangros, J. Sastre-Pellicer, M. Kawecki, A.

- Paracchino, T. Moser, J. Werner, C. Andres, L. Duchêne, P. Fiala, M. Rawlence, S. Nicolay, C. Ballif, A. N. Tiwari, S. Buecheler, *Energy & Environmental Science*, **2019**, 12, 3074.
- [181] H. Nagasaka, M. Yoshizawa-Fujita, Y. Takeoka, M. Rikukawa, *ACS Omega*, **2018**, 3, 18925.
- [182] J. Duan, Y. Wang, X. Yang, Q. Tang, *Angewandte Chemie International Edition*, **2020**, 59, 4391.
- [183] Y. Hou, Z. R. Zhou, T. Y. Wen, H. W. Qiao, Z. Q. Lin, B. Ge, H. G. Yang, *Nanoscale Horizons*, **2019**, 4, 208.
- [184] J.-a. Yang, T. Qin, L. Xie, K. Liao, T. Li, F. Hao, *Journal of Materials Chemistry C*, **2019**, 7, 10724.
- [185] S. Wang, K. Xuezhi, W. Zhang, W. Gong, P. Huai, W. Zhang, Z. Zhu, *Applied Surface Science*, **2014**, 292, 488.
- [186] A. C. Ferrari, *Solid State Communications*, **2007**, 143, 47.
- [187] S. N. Habisreutinger, T. Leijtens, G. E. Eperon, S. D. Stranks, R. J. Nicholas, H. J. Snaith, *The Journal of Physical Chemistry Letters*, **2014**, 5, 4207.
- [188] C.-T. Hsieh, J.-M. Chen, Y.-H. Huang, R.-R. Kuo, C.-T. Li, H.-C. Shih, T.-S. Lin, C.-F. Wu, *Journal of Vacuum Science & Technology B: Microelectronics and Nanometer Structures Processing, Measurement, and Phenomena*, **2006**, 24, 113.

국문초록

유기-무기 할라이드 페로브스카이트를 기반으로 한 페로브스카이트 태양전지는 뛰어난 광학적 및 물리적 특성에 기초하여 가장 강력한 차세대 광전지 중 하나로 급속히 발전해왔다. 현재까지 빠르게 개선된 페로브스카이트 태양전지의 광기전 성능은 상업용 실리콘 태양전지에 필적한다. 최근 연구 추세는 페로브스카이트 태양전지의 상용화를 위한 대규모 모듈화, 장기 안정성 및 독성 테스트와 같이 일상 생활에서 페로브스카이트 태양전지의 실제 사용과 관련된 실제 문제로 바뀌고 있다. 특히 안정성 측면에서 페로브스카이트의 수분, 대기 및 열에 의한 분해의 저하와 금속전극 및 전하이동층과의 계면 열화는 반드시 해결해야 할 문제이다. 더 나아가, 고가의 금속전극 및 전하이동층 도입의 공정 효율성이 떨어지는 부분도 개선해야 할 사항이다. 이러한 문제를 해결하기 위한 대안 중 하나는 저렴하고, 안정적인 카본 전극을 이용하여 정공 전도체 없이 페로브스카이트 태양전지를 제조하는 것이다.

카본 전극 기반 페로브스카이트 태양전지는 높은 수분 및 열 안정성을 가질 뿐만 아니라 다양한 전극 도입 방법을 통해 제조될 수 있으므로, 대량 생산 및 소자 대형화에 적합하다. 그러나, 이와 같은 공정 효율성 및 장치 안정성에도 불구하고, 카본 전극 기반 페로브스카이트 태양전지는 카본층과 페로브스카이트 광 흡수층 사이의 물리적 / 화학적 접촉이 불량하기하므로 종래의 금속 전극 기반 페로브스카이트 태양전지보다 효율이 떨어진다. 따라서 카본 전극 기반 페로브스카이트 태양전지의 실제적 상용화를 위해서는 계면 접촉성 향상을 통해 고성능, 고안정화된 카본 전극 기반 페로브스카이트를 제조할 수 있어야 한다.

본 논문에서는 다양한 공정 및 물질을 기반으로 한 계면 엔지니어링을 통해 카본 전극 기반 페로브스카이트 태양전지를 제조할 때 탄소 전극과 페로브스카이트의 계면 접촉을 개선하는 효과적인 전략을 제시하였다. 자세하게는, 용액 공정을 통해 유기 및 무기 물질을 도입하여 계면 층의 성장을 유도하거나 플라즈마 공정을 통해 탄소 전극의 계면 에너지 수준을 조정하였다. 첫 번째로, 부피가 큰 유기 리간드 (페닐에틸암모늄요오드) 용액을 이용하여 제조된 페인팅된 카본 전극 기반 페로브스카이트 태양전지 상 처리하여, 2 차원

페로브스카이트 계면층을 도입하였다. 도입된 2 차원 페로브스카이트 계면층은 정렬된 에너지 레벨 수준을 제공하며, 정공 추출 능력 향상과 계면 전하 재결합을 억제하였다. 이를 통해 카본 전극 기반 페로브스카이트 태양전지 성능을 향상시켰다. 또한, 2 차원 페로브스카이트는 수분 및 열 안정성이 높아 소자의 안정성을 더욱 높이는 것을 확인하였다. 두 번째로, 계면 접착성을 더욱 향상시킨 페로브스카이트 계면층을 형성하기 위해, 무극성 용매에 분산될 수 있는 유기산으로 둘러싸인 콜로이드 PbI_2 를 제조하였다. 제조된 콜로이드 PbI_2 는 제조된 카본 전극 기반 페로브스카이트 태양전지에 소자 손상 없이 계면에 도입되었으며, 추가적인 메틸암모늄 요오드 처리를 통해 $MAPbI_3$ 계면층의 이차성장을 유도하였다. $MAPbI_3$ 계면층의 이차성장은 유기 리간드 처리만으로 잔존하는 PbI_2 와 반응시키는 이전 연구들과 비교하였을 때, 카본 전극과 페로브스카이트 계면 접착성이 극대화되며 소자 성능이 크게 향상되었다. 또한, 계면층이 형성될 때 존재하는 소수성 유기산들에 의해 소자 안정성 향상에 기인하였다. 셋째로, 플라즈마 공정을 기반으로 불소가 농도 구배로 도입된 카본 전극을 제조하였다. 전자 끌개 특성이 큰 불소가 카본 전극에

도입되며 전극의 일 함수와 페로브스카이트의 호모 레벨의 에너지 레벨 수준 정렬에 따라 정공 수송 능력 향상되며 소자의 성능을 향상을 유도하였다. 더 나아가 소수성 불소 원자가 소수성 카본 전극에 도입되며 시너지 효과로 수분 안정성이 극대화된 카본 전극 기반 페로브스카이트 태양전지를 제조할 수 있었다. 따라서 본 논문은 다양한 공정/물질을 바탕으로 한 계면 엔지니어링을 통해 카본 전극 기반 페로브스카이트 태양전지의 성능 향상 방법을 제시할 뿐만 아니라 소자의 장기 안정성까지 더욱 향상시킬 수 있는 전략을 제시한다.

주요어: 페로브스카이트 태양전지, 카본 전극, 계면 엔지니어링, 2차원/3차원 혼성 페로브스카이트, 콜로이드 PbI_2 , 계층적 페로브스카이트, 불소 플라즈마 처리, 에너지 레벨 조절

학 번: 2017-32525

감사의 글

다사다난한 일들과 함께 긴 시간 동안, 다양한 곳에서 다양한 분야에 대한 연구를 해오며 5년이란 시간만에 연구자로서 큰 책임을 갖는 박사로서 관악산을 내려가게 되었습니다. 이 과정에서 많은 사람들과 많은 일들을 접하였고, 좋은 일들도 있었고 어려운 일들도 있었습니다. 그 과정에서 학문적으로도, 인생적으로도 많은 부분을 배울 수 있었으며 이를 통해 제한걸음 성장하여 이곳을 내려간다고 생각합니다. 이러한 성장에 있어 제 주변의 많은 분들의 관심과 도움, 헌신과 사랑, 그리고 독려와 응원이 아니었다면 어려웠다고 생각합니다. 이에 그동안 전하지 못한 감사의 인사를 드리며 본 학위 논문을 마무리하고자 합니다.

먼저 스승이자 교육자로서 저를 이끌어주신 장정식 교수님께 감사드립니다. 박사 학위 과정을 마무리함에 있어, 좌절하고 포기할 뻔한 순간들이 있었지만 항상 저의 손을 놓지 않고 교수님께서 저를 이끌어 주셨기에 인생에서의 중요한 챕터 중 하나를 잘 마무리할 수 있었다고 생각합니다. 교수님께서 연구적으로도 저를 성장시켜 주셨지만, 저는 교수님께서 한

명에 연구자로서, 박사로서 어떠한 자세와 책임을 가지고 살아가야하는지에 대한 원론적인 깊은 가르침을 주시며 저의 본질적인 가치를 높여 주셨다고 생각합니다. 아직도 성장해야 할 부분이 많지만, 고분자재료연구실의 문을 처음 두드린 저의 생각과 행동이 지금과는 많이 다르게 성장하였으며 이 기틀에는 교수님의 가르침이 있습니다. 앞으로 연구자로 나아감에 있어 교수님의 가르침들을 바탕으로 올바른 방향으로 성장해 나가겠습니다. 또한 교수님 옆에서 저를 위해 기도해주신 사모님께도 무궁한 감사드립니다. 교수님 가정에 항상 평안과 행복이 가득하기를 기원하겠습니다. 아울러 바쁘신 와중에도, 제가 박사 연구자로 거듭날 수 있게 저의 논문과 연구에 많은 조언해주시고 심사해주신 조재영 교수님, 이종찬 교수님, 오준학 교수님 그리고 임순호 박사님께도 깊이 감사드립니다. 뿐만 아니라 석사과정까지 지도해주시고 이후 연구자로서 길을 걷는데 물심양면으로 많은 도움을 주시고 신경써주신 함승욱 교수님께 감사드립니다. 가까이있음에도 자주 연락드리지 못하고 찾아뵙지 못했지만, 먼저 신경써주시고 생각해주셔서 항상 죄송스럽고 감사했습니다. 앞으로 연구자로서 더욱 성장하며 교수님께 먼저 인사드리고 감사의 마음 전달하겠습니다.

뒤늦게 고분자재료 연구실의 일원으로 들어와 성장함에 있

어 도움을 주신 고분자재료 연구실 사람들에게 감사드립니다.

먼저, 어려운 상황에서 고민할 때 손 내밀어주고 많은 도움을 준 페로브스카이트 태양전지팀에 감사드립니다. 방장으로 도 바쁘고 정신없지만 처음 접하는 연구인 페로브스카이트에 대한 전반에 대해 항상 친절하고 꼼꼼하게 알려주며 진심으로 저의 졸업과 연구에 대해 책임감가지고 신경 써준 기수, 10층의 마지막 문단음을 같이하며 마음을 털어놓을 수 있던 술 친구이자 연구적으로 방향을 잡지 못하는 생각들은 번뜩이는 아이디어들로 갈무리해준 해준이에게 감사드립니다. 이 둘이 있었기에 페로브스카이트 연구를 하며, 박사도 거듭날 수 있었음에 다시 한번 감사하다는 이야기 전합니다.

그리고 마지막까지 연구실을 지킨 사연러들, 성근이형과 윤기에게 감사함을 전합니다. 연구실을 정리하는 클로저로서, 졸업 동기로서 함께한 성근이형이 있었기에 서로 응원하고, 의지해오며 본 과정을 마무리할 수 있었다고 생각합니다. 유부선배로서, 기기 마스터로 많은 조언을 아끼지 않은 나윤이 아버지이자 박사 선배인 윤기에게 많은 배움을 얻었습니다.

또한 처음 고분자재료 연구실의 일원으로 적응하는데 많이 독려해주신 듬직한 방장 재문이형, 항상 연구실과 후배를 아끼고 신경써주신 함양의 아들 재훈이형, 시크하지만 따뜻한

매력을 지닌 주영이형, 분위기 메이커로 밝은 에너지 주는 정섭이, 연구 이야기를 주고받으며 다양한 아이디어를 준 정철이, 그리고 형으로서, 선배로서 흔들릴 때 많은 용기를 주고 도와준 창민이형, 연구실 전자기기를 책임져준 영덕이, 묵묵히 누나로서 연구실에서 자리를 지켜준 고은누나, 패션 이야기로도 연구이야기로도 많은 즐거움을 주고 받은 예비군 동기 정섭이, 나의 10층 옆자리 메이트로 많은 질문에 친절하게 알려준 경희, 부산에서 시작된 우리의 술자리가 아직도 진행형인 이수 친구 정균이, 독설가인 것 같지만 섬세한 촌테레 원주, 무뚝뚝한 상남자일 것 같지만 자기의 자리에서 책임감있게 남들을 잘 챙겨주는 우영이, 긍정적인 에너지로 웃음을 준 계절학기 메이트 예리까지 함께해온 모든 연구실 사람들에게 감사드립니다.

또한 처음 서울대에서 박사 학위를 시작하고 마침에 있어 많은 도움을 주었던 서울대 화학과 분자인식 초분자화학 연구실의 입학 동기 김경록, 고생 많이해준 장재규, 유기 조연자 오진록에게 감사의 인사를 전합니다.

학부 선후배, 동기로 만나 학위 과정을 마무리함까지 많은 도움을 준 생화학연구실의 나의 가장 가까운 형인 한국현, 매니저로 항상 고생한 민범홍, 항상 가까이에서 신경써준 동생

송승윤, 마음도 몸도 누구보다 큰 조흥기, 항상 진중한 안성우, 4차원 매력으로 즐거움을 준 김형연에게 감사드립니다.

고된 학위기간 동안 저에게 많은 에너지를 주고 어린 시절 부터 지금까지 김중원으로서 성장할 수 있게 도와준 친구 류광균, 윤선용, 이승재, 이지환, 정동석, 정인규, 차준희, 최용석, 최현준, 하재언, 황원석, 허성욱에게도 감사드립니다.

지금까지 저를 사랑과 헌신으로 돌봐주신 아버지 김규호님과 어머니 정선주님이 없었다면 여기까지 오지 못하였을 것입니다. 인생의 선배로서, 부모로서 제가 바르게 가지 못하는 부분에서는 가르침을 주시고 힘겨워할 때는 온 마음으로 독려해주신 부모님들이 있었기에 여기까지 성장할 수 있었습니다. 표현이 적은 아들이라 이야기는 못했지만 아버지, 어머니 진심으로 감사드리고 사랑합니다. 그리고 표현이 서툰 동생이라 내색하지 못했지만 항상 옆에서 지켜주고, 신경써주고, 배려해준 우리 형 김중엽에게 감사의 마음 전합니다.

또한 부족한 저를 사위로서 인정해주시고, 항상 격려와 조언을 아껴지 않으신 장인어른 윤영욱님과 여전히 소녀 같으시고, 내색하지 않으시지만 고생하시며 맛있는 요리들을 챙겨주시며 아껴주시는 마음 표현해주시는 장모님 선계숙님께도 진심으로 감사드립니다. 표현이 서툴지만 더욱 아들 같고 의지

되는 사위 김종원이 될 수 있도록 노력하겠습니다.

마지막으로 2011년 12월 28일부터 옆자리에서 부족한 나를 채워주고 지켜준 인생의 동반자인 사랑스러운 아내 은혜에게 감사합니다. 그녀가 있어 항상 행복하고, 즐거울 수 있음에 감사합니다. 앞으로 함께 지내온 세월보다 지낼 세월이 많은 그녀에게 항상 힘이되는 남편이자 친구로서 함께함을 약속할 것 입니다. 고된 상황에서도 묵묵히 저의 옆을 지켜와 준 은혜에게 다시 한번 감사의 마음 전합니다.

연구자로서, 박사로서 사회에 나가는 것은 비단 저의 노력보다 주변에 힘이 되어준 많은 좋은 사람들이 있었기에 가능한 일이라고 생각합니다. 치열한 경쟁사회에 들어가더라도 이 고마움을 잊지 않고 선한 영향력을 주는 사람으로, 깊이 연구하는 연구자로 거듭 반성하고 성장하며 살아갈 수 있도록 노력하겠습니다. 다시 한번 제가 성장할 수 있도록 도와주신 모든 분들께 감사드리며 항상 건강하기를 기원합니다.

2020년 7월 늦은 어느 날

관악산을 내려가며

김종원 드림